University of Alberta

Stray Loss Analysis of AC Machines Using Time-Stepped Finite Elements

by

Yang Zhan

A thesis submitted to the Faculty of Graduate Studies and Research
in partial fulfillment of the requirements for the degree of

Doctor of Philosophy
in
Power Engineering and Power Electronics

Department of Electrical and Computer Engineering

©Yang Zhan
Spring 2010
Edmonton, Alberta

Permission is hereby granted to the University of Alberta Libraries to reproduce single copies of this thesis and to lend or sell such copies for private, scholarly or scientific research purposes only. Where the thesis is converted to, or otherwise made available in digital form, the University of Alberta will advise potential users of the thesis of these terms.

The author reserves all other publication and other rights in association with the copyright in the thesis and, except as herein before provided, neither the thesis nor any substantial portion thereof may be printed or otherwise reproduced in any material form whatsoever without the author's prior written permission.

Examining Committee

Andrew M. Knight, Department of Electrical and Computer Engineering

John Salmon, Department of Electrical and Computer Engineering

Marek Reformat, Department of Electrical and Computer Engineering

Roger Toogood, Department of Mechanical Engineering

Narayan Kar, Department of Electrical and Computer Engineering, University of Windsor

Abstract

This thesis investigates stray losses in AC machines using the time-stepped finite element technique. Two aspects of this topic are involved in this thesis. The first aspect is to construct a finite element model for AC machine systems and develop an efficient numerical solution for the system equation; as the emphasis of this thesis, the second aspect is use the above model to analyze stray losses in AC machines under a variety of operation, design and manufacturing conditions.

The thesis modifies the traditional 2-D finite element technique to account for the variations in electromagnetic field along the machine's axis resulting from skewed structures, rotor interbar currents and ventilation ducts. Domain decomposition and parallel computation are incorporated to efficiently give a numerical solution to the system equation.

The factors affecting harmonic stray losses in AC machines including pulse width modulation (PWM) supply, interbar resistance and slot shape are investigated using the above efficient analysis tool. Simulations and tests under different load conditions are carried out for an induction motor to investigate the additional harmonic stray loss caused by the PWM supply. For a large synchronous generator, simulations and tests are performed to study the effect of different amortisseur interbar resistances on the slot harmonic contents and the resulting harmonic stray loss in the amorisseur cage. As a factor influential to magnet stray loss in permanent magnet synchronous machines, various slot shape designs are assessed by simulations. An optimization based on an evolutionary strategy is implemented to find the best slot shape design with minimum machine loss.

The conclusions in the thesis provide valued information to direct the future design and manufacture of efficient AC machines.

Acknowledgement

I would like to express my thanks to the following people and organizations:

- Dr. Andrew M. Knight for his excellent supervision, advice and support.
- Drs. Aldo Bolietti and Andrea Cavagnino from Politecnico di Torino, Turin, Italy, for their test results supporting part of this research.
- GE Canada for providing funding for this research, and in particular Dr. Nick Stranges for providing the machine data and test results to support part of this research.
- Dr. Svetlana Troitskaia and Mr. Ming Jiang for the instructive discussions on some of the research topics.

Table of Contents

List of Tables

List of Figures

List of Symbols

$\mathbf{A}$	magnetic vector potential
$\mathbf{A}_\mathrm{N}$	a vector of nodal magnetic potentials
A_st	slot area
B	magnetic flux density
$\hat{B}$	peak value of magnetic flux density
B_e	element flux density
$\mathbf{B}_\mathrm{r}$	residual flux density vector of permanent magnet
$B_{\mathrm{r}x}$	x-component of $\mathbf{B}_\mathrm{r}$
$B_{\mathrm{r}y}$	y-component of $\mathbf{B}_\mathrm{r}$
d	iron lamination thickness
E_p	phase electromotive force
f	fundamental frequency
g	minimum length of air gap
H	magnetic field intensity
H_c	coercive force of magnet
i_d	direct axis current
I_f	field current
i_q	quadrature axis current
$\mathbf{I}_\mathrm{r}$	a vector comprised of rotor loop currents
$\mathbf{I}_\mathrm{s}$	a vector comprised of stator phase currents
$\mathbf{J}$	current density
K_C	Carter’s coefficient
k_e	excess loss constant determined from experiments
k_h	a constant determined by fitting a P_h - $\hat{B}$ experimental curve
K_l	penalty factor for lower limit
K_s	skew factor
K_u	penalty factor for upper limit
L	overall core length

L'	effective core length
L_d	direct axis inductance
L_{er}	end-ring segment inductance
L_{ew}	end-winding inductance
L_{pm}	axial length of permanent magnet
L_q	quadrature axis inductance
L_{sl}	machine core length in each slice
m_{a}	amplitude modulation index
N_{b}	number of rotor bars
N_{c}	number of stator circuits in parallel
N_{cs}	number of coil sides per phase
N_{d}	number of ducts
N_{dv}	number of decision variables
N_{ele}	total number of unknown electric variables
N_{f}	number of turns of field winding
N_{p}	number of phases
n_{s}	synchronous speed
N_{sl}	number of slices
N_{st}	number of stator slots
N_{t}	number of turns per stator coil
p	number of pole pairs
P_{e}	eddy-current loss density in iron laminations
P_{ex}	excess loss density in iron laminations
P_{h}	hysteresis loss density in iron laminations
P_{pm}	eddy-current loss of permanent magnet
$\mathbf{R}^{-1}$	covariance matrix
R_{b}	rotor bar resistance
R_{bb}	bar-bar resistance
R_{c}	bar-iron contact resistance
R_{i}	iron resistance
R_{p2p}	pole-pole iron resistance

R_{s}	stator phase resistance
s	slip
T	period
T_{e}	electromagnetic torque
t	time
$\mathbf{V}_{\mathrm{b}}$	a vector comprised of voltages over rotor bar segments
v_d	direct axis voltage
V_{DC}	DC link voltage
v_q	quadrature axis voltage
$\mathbf{V}_{\mathrm{s}}$	a vector of polyphase supply voltages
w	slot opening
w_{d}	duct width
$\boldsymbol{x}$	a vector of decision variables
Z_{b}	impedance of rotor bar segment
Z_{end}	impedance of end-ring segment
Z_{p2p}	pole-pole end-ring impedance
α	a constant determined by fitting a P_h - $\hat{B}$ experimental curve
β	skew angle
Δ_{b}	cross section of rotor bar
Δ_{cs}	cross-sectional area of stator coil side
Δ_{e}	element area
Δ_{f}	coil side area of field winding
δ	skin depth
ε	slot pitch
ε_{d}	duct pitch
$\boldsymbol{\theta}$	a vector of rotation angles (for evolution strategy)
μ_{m}	iron lamination permeability
ν	reluctivity
ν_0	reluctivity of air, stator winding and rotor bar
ν_{e}	element reluctivity
ν_{m}	reluctivity of iron laminations

ν_{pm}	reluctivity of permanent magnet
ρ	mass density of iron laminations
$\boldsymbol{\sigma}$	a vector of step size values (for evolution strategy)
σ_{b}	rotor bar conductivity
σ_{m}	iron lamination conductivity
σ_{pm}	conductivity of permanent magnet
ϕ	magnetic flux
Ψ	magnetic flux linkage
Ψ_d	direct axis flux linkage
Ψ_{pm}	flux linkage of permanent magnet
Ψ_q	quadrature axis flux linkage
ω_{e}	electrical frequency of stator current

Subscripts

b	rotor bar
f	field winding
m	iron lamination
pm	permanent magnet
s	stator
sl	slice
st	slot

Superscripts

t	at the time t
$t + \Delta t$	at the time ($t + \Delta t$)

List of Abbreviations

C-N	Crank-Nicholson
DD	domain decomposition
EMF	electromotive force
ES	evolution strategy
FEA	finite element analysis
FEM	finite element method
FFT	fast Fourier Transform
IPM	interior-mounted permanent magnet
KVL	Kirchhoff’s voltage law
MMF	magnetomotive force
MPI	Message Passing Interface
N-R, NR	Newton-Raphson
PMSM	permanent magnet synchronous machine
PWM	pulse width modulation
SPM	surface-mounted permanent magnet
SPWM	sinusoidal pulse width modulation
TLM	transmission line modeling

Chapter 1 Introduction

Electric machines are widely used as electro-mechanical energy converters in home appliances and industrial production. Electric motors which convert electric energy to mechanical energy consume a large percentage of the electric energy produced, typically about 60% in industrialized countries [1]. Electric generators which convert mechanical energy to electric energy produce almost all the global electricity consumed. The energy loss associated with the process of electro-mechanical energy conversion has always been a concern of electric machine manufacturers and users. In modern society, economic growth is increasingly dependent on the consumption of fossil fuels. An opinion generally accepted is that the fossil energy resources will be eventually depleted due to the increasing consumption of fossil fuels, and on the other hand this results in the excessive emission of greenhouse and toxic gases. These resource and environment issues evoke a close attention to the energy losses inside electric machines. As a large portion of fossil energy is converted to other energy forms or eventually consumed by electric machines, the reduction of electric machine losses may help relieve the pressure on natural resources and environment. A full investigation of the loss mechanism is a prerequisite for the design of energy-efficient electric machines. This thesis focuses on the loss mechanism analysis for AC electric machines including induction machines, synchronous machines and permanent magnet synchronous machines.

1.1 Components of AC machine losses

The losses that occur in AC machines can be divided into four basic categories:

1. Joule loss (I^2R losses)
2. Iron loss
3. Mechanical loss
4. Stray loss

Joule loss is the ohmic heating loss that occurs in stator windings, field windings (in synchronous machines) and rotor windings or squirrel cage (in induction machines). Since the conductor resistances are temperature dependent, the Joule losses are dependent on the expected operation temperature.

The core of an electric machine is usually made of laminated ferromagnetic material, which is exposed to time and space varying magnetic fluxes. These fluxes produce hysteresis loss, eddy-current loss and excess loss. These three categories of magnetic losses occurring in the laminated core are lumped together to form the iron loss.

Mechanical loss is associated with two mechanical effects in an AC machine: friction and windage. Friction loss is caused by the friction of bearings, while windage loss is caused by the air resistance that acts on the moving parts inside the machine. In some cases a fan is designed in to the end of the machine's rotor in order to provide the air flow cooling the machine. The built-in cooling fan consumes the input energy to the machine without developing output. This portion of energy loss is also included in the windage loss.

Stray loss is the portion of total loss that is difficult to model and quantify. This portion of loss is not strictly independent of other loss categories in this thesis. In the initial stage of design, most electric machine manufacturers give raw design of basic structures using their in-house software based on analytical and empirical equations. Regarding the loss calculations these programs assume that losses only occur because of the fundamental frequency of field. Due to this design routine, "Joule loss" and "iron loss" terms in common usage only refer to those losses at fundamental frequency. However, in additional to the fundamental losses, harmonic currents and harmonic fields do cause another portion of Joule loss and iron loss. As these additional losses are unable to be precisely calculated by the in-house programs, they are treated as stray losses in most of the previous work on machine losses. In this thesis, the terms of "Joule loss" and "iron loss" refer to the sum of loss components at all frequencies. The harmonic components of those losses that are treated as stray losses are termed as "harmonic Joule loss" and "harmonic iron loss".

The ratio of each above loss components to a total machine loss is a function of machine size and load condition. Generally speaking, with the increased load the proportion of iron loss and the proportion of mechanical loss become less significant relative to the proportion of Joule loss.

1.2 Origins of stray losses in AC machines

Stray losses may bring extra temperature rise and machine performance degradation, therefore it is essential to understand the phenomena causing these losses and evaluate them for design of higher efficiency electric machines. Although stray losses in AC machines have been defined from the different aspects of the subject, there is general agreement that the following constitute the physical origins of stray losses [2], [3]:

1. Saturation of magnetic material
2. The space harmonics of magnetic field caused by the geometrical structures around the active region of the machine such as slots, windings and air-gap
3. The nonsinusoidal input supply to a machine
4. The leakage flux in the frame, end-region and other metallic parts
5. The fringing flux caused by slots and ventilation ducts, if present
6. Industrial imperfection – the most prominent of which is interbar currents due to imperfect insulation of the squirrel cage bars or the amortisseur bars

1.3 Loss analysis by finite element method

Manufacturers rely on experimental and simulation approaches to quantify the losses in electric machines. For induction machines and synchronous machines, IEEE or IEC standards [4] - [6] define some segregated losses that are similar to the loss components mentioned in Section 1.1. These standards also give recommendations on the test procedures for determination of those losses. The simulation approach for machine loss analysis is the subject of this thesis. Electromagnetic simulations have been carried out in the process of design to predict the various performances of electric machines. Generally the electromagnetic field in an electric machine is modeled by the Maxwell's equations and the machine performances associated with the field are simulated by solving these equations. As friction and windage are purely mechanical performances which usually need tests to be determined, they are not in the scope of electromagnetic simulations involved with this thesis.

1.3.1 The application of time-stepped finite element method

A full knowledge of the electromagnetic field distribution is required for electric machine loss analysis. In an electric machine, the field varies with time and space and may be saturated at certain regions of the iron core. Time-stepped finite element analysis (FEA) is a simulation technique that can calculate the field distribution in time domain, therefore it is a suitable technique for modeling of the time and space varying nonlinear field in electric machines. This feature is essential particularly to the accurate prediction of stray losses as time-stepped FEA is capable of predicting the harmonics which constitute a large proportion of stray losses.

This thesis studies two aspects regarding the application of time-stepped finite elements in AC machine analysis. One aspect is the finite element modeling of AC machines. In this thesis some modifications are made to the conventional 2-D finite element method (FEM) by incorporating multislice technique, Carter’s coefficient and interbar circuit model in order to adapt it to certain special structures such as skewed bars (or slots) and ventilation ducts as well as manufacturing variations such as imperfect interbar insulation. The modified 2-D time-stepped finite element models are developed for induction machines, synchronous machines and permanent magnet synchronous machines, respectively. Most of the origins of stray losses mentioned in Section 1.2 can be taken into account using the 2-D model without incurring the impractical complexity and computation overhead of a fully time-stepped 3-D model. However the 2-D technique is still relatively expensive in comparison to the traditional analytical method as the former solves a large number of coupled equations at each time step for circuit variables and nodal magnetic potentials, though the number of these equations is much less than that with the 3-D technique. Thus the other aspect of the research on time-stepped FEA of AC machines is the investigation of the approaches to reduce the computation time required to solve the finite element equations. This thesis proposes an efficient parallelized algorithm based on domain decomposition to the time-stepped finite element model for AC machines.

1.3.2 Loss analysis for AC machines

This thesis aims to analyze AC machine losses using the modified efficient 2-D time-stepped finite element model. Emphasis is placed on the investigation of some factors affecting stray losses in induction machines, synchronous machines and permanent magnet synchronous machines. These factors include supply harmonics, rotor interbar resistances and shape of certain structure.

A. Interbar resistance

The induced interbar leakage currents between rotor bars are conventionally neglected in the AC machine design routines. A reason for this is the difficulty in modeling the bar-bar insulation by the traditional design routines based on analytical and empirical calculations. However the interbar currents are considered a vital internal factor underlying harmonic field in AC machines as well as a considerable source of harmonic stray losses. The bar-bar insulation represented by interbar resistances varies significantly with individual machines due to manufacturing variations. In this thesis the interbar circuit originating from the modeling of noninsulated cage bars in induction machines is generalized for the modeling of noninsulated amortisseur bars in synchronous machines, and the effects of interbar resistance variation on the various field harmonics and the relevant stray losses are investigated.

B. Supply harmonics

Pulse width modulation (PWM) schemes are commonly used in variable speed drives. As an external source of harmonics to AC machines a PWM supply causes additional stray losses at the PWM frequency. Simulations are carried out in this thesis for induction machines under a range of load conditions in order to investigate the additional stray losses caused by a PWM supply and their relation to the load variations. It is expected that these simulation results provide a better understanding of stray losses caused by PWM frequency and consequently better inform future design of induction machines with nonsinusoidal supply.

C. Slot shape

The field distribution in an electric machine is a function of the dimension and shape of parts and structures. The adjustment of dimension and shape design may change the field distribution as well as the total loss. It is particularly of interest to the manufacturers of high-efficiency machines to seek the optimal design with the lowest losses using appropriate optimization algorithms. Of the various structures in an electric machine, the adjustment of slot shape is an economical approach to contribute towards loss reduction after an initial design using low-loss materials has been carried out. In this thesis a permanent magnet synchronous machine (PMSM) is selected as the prototype for slot shape optimization in order to minimize the total loss. An optimization based on evolution strategy is implemented and the 2-D time-stepped FEA is used to evaluate the loss components of the PMSM including the stray loss in the permanent magnets. The thesis highlights the advantage of the proposed optimal slot shape design in reducing the magnet stray loss.

1.4 Contributions

This thesis develops a universal time-stepped 2-D finite element model for AC machines. Some improvement techniques are incorporated with this model to make it compatible with the axial field variation caused by skewed bars (or slots), ventilation ducts and interbar currents. An efficient algorithm based on domain decomposition and parallel computation is proposed for solving the equations derived from that model.

The thesis demonstrates that the combination of the proposed model and the efficient parallel algorithm is an efficient tool for the evaluation of AC machine performances. The time-stepped FEA is carried out to evaluate the stray losses in three basic types of AC machine: induction machine, synchronous machine and PMSM. Three factors affecting stray losses in AC machines are emphasized in this thesis: imperfect bar-bar insulation, PWM supply and shapes and dimensions of certain parts such as stator slots. Using time domain simulations, the thesis makes a comprehensive analysis of the relation between these three factors and stray losses. A portrait of AC machine stray losses is obtained, and this information may guide electric machine manufacturers to develop new design for energy-efficient machines, which would be considered an asset in the current situation of energy scarcity. In pursuit of this goal, this thesis makes a valuable attempt at the design optimization based on evolution strategy and time-stepped FEM.

This thesis presents a number of measurement results, and simulation results are obtained under the same supply and speed conditions. The machine performances under a number of variable factors (i.e. rotor temperatures and interbar resistances) are simulated in order to explain the experimental observation related to stray losses.

Chapter 2 Background Theory and Literature Review

Three types of AC machines are studied in this thesis: induction machines, synchronous machines and PMSMs. Section 1.2 clarifies the general origins of stray losses in AC machines. Of those origins field harmonics may cause stray losses in a variety of parts exposed to those field harmonics, depending on the construction of different types of AC machines. The following sections give the qualitative explanations on the cause of field harmonics and harmonic stray losses. Most manufacturers of electric machines employ experiments to quantify these losses. Some of these stray loss test procedures are reviewed in this section.

2.1 Induction machines

By their rotor construction induction machines are classified into squirrel cage machines and wound rotor machines. In this thesis the induction machines involved in the loss study are squirrel cage machines. Squirrel cage induction machines have rugged construction without brushes. This characteristic increases their reliability and reduces maintenance costs. Induction machines are the preferred choice for industrial motors as the speed control of induction machines is now feasible thanks to modern power electronics.

2.1.1 Harmonics and stray losses in induction machines

In order to locate the parts where the harmonic stray losses occur, it is necessary to briefly introduce how the stator and rotor fields form in an induction machine. The stator current produces the rotating fundamental field at supply frequency. The rotor fundamental field and the induced fundamental current in squirrel cage vary at slip frequency due to the rotor’s motion at slip speed relative to the rotating fundamental field.

Figure 2-1 summarizes the cause of harmonic stray losses in an induction machine. As an important source of harmonics in induction machines, a nonsinusoidal supply introduces current time harmonics that produce harmonic

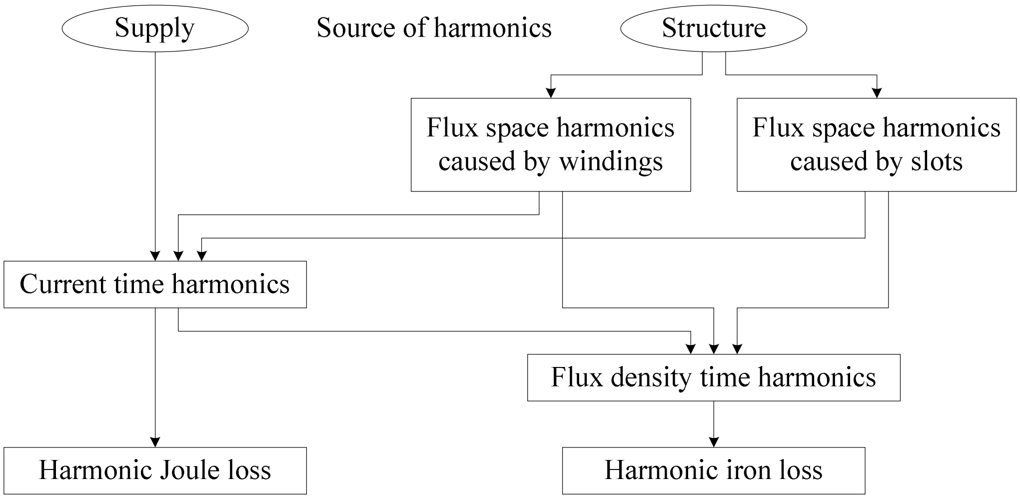

Figure 2-1 Harmonic stray losses in an induction machine

Joule losses and cause harmonic iron losses through the induced harmonic fields. A typical example of the nonsinusoidal supply is an inverter that may produce current harmonics at the PWM switching frequency. The structures such as windings and slots form the other source of harmonics (i.e. space harmonics) in an induction machine. Space harmonics in air-gap flux density are partly due to the nonsinusoidal spatial distribution of the stator windings, and the other portion of space harmonics, referred as slot harmonic, is produced by the reluctance fluctuation due to the slot-tooth modulation. The flux density space harmonics produce a stationary wave interacting with the rotating fundamental field to give the rotating harmonic fields. The flux densities corresponding to these field time harmonics produce additional harmonic iron losses and induce additional harmonic currents that cause extra harmonic Joule losses in windings and bars. In summary, the harmonics caused by supply and machine structure are both reflected in the stator current, the induced current in rotor cage and the iron laminations. The resulting harmonic Joule loss and harmonic iron loss constitute the harmonic stray losses in an induction machine.

2.1.2 Interbar currents in induction machines

Due to their simplicity and effectiveness cast rotor cages are widely used in induction machines, particularly in small ratings. A disadvantage of cast cage is the imperfect insulation between the rotor bars and the rotor core. This manufacturing process leads to current flowing circumferentially between successive rotor bars through the lamination iron. This current is commonly referred to as “interbar current”. Large induction machines adopt the more traditional fabricated cage where the copper bars are inserted into the rotor slots. Generally a fabricated cage has less regular bar-iron contact surface and as a result a better interbar insulation than an equivalent cast rotor [7].

In an induction machine the interbar current is a common phenomenon that requires a special attention when modeling the machine as it contributes to the axial variations in both flux density and bar current density. The presence of interbar current changes particularly the harmonic electromagnetic field distribution in the rotor, and therefore the interbar current is considered an important factor underlying the rotor stray losses. An experimental study undertaken by the Toshiba Corporation claimed that the losses in a cast cage machine due to interbar currents constitute approximately 30% of the typical stray-load losses [7].

2.1.3 Determination of stray loss by experiment

As experimental methods for determination of stray losses are not the main concern of this thesis, this section gives the brief comments only on the stray loss measurement procedure introduced in IEEE Standard 112, a representative of the prevalent international standards for induction machine testing.

IEEE Standard 112 defines some segregated losses in an induction machine and describes the tests and calculations to be used to determine these losses [4]. The segregated losses include stator I^2R loss, rotor I^2R loss, friction and windage loss, core loss, and stray-load loss. Stray-load loss is defined as that portion of the total loss in a machine not accounted for by the sum of the other loss components. Generally, stray-load loss is actually the stray loss when load is applied, so it is dependent on motor loading. The standard defines the no load test and some other procedures to isolate stator I^2R loss, core loss, friction and windage loss from the total no-load losses, however the harmonic Joule loss in squirrel cage, which is supposed to be a stray loss, is treated as a part of the core loss in this standard. Although the IEEE Standard 112 provides a reverse-rotation test as the direct measurement method of stray loss, criticisms have been reported that the principle and presumption of this method are indeed problematic [8] and the measurement results are subject to a high degree of uncertainty [9] - [12]. According to empirical estimations the stray-load loss in an induction machine amounts to 1% - 2% of the output, but values as low as 0.5% and as high as 4% are not uncommon [13].

2.2 Synchronous machines

Almost all electrical power plants use synchronous machines to generate electricity. In some cases synchronous machines are used not to provide any real power to a power system, and instead they generate or absorb reactive power as compensators to improve the power factor on the local grid they are connected to.

2.2.1 Rotor construction of synchronous machines

The stator structure in a synchronous machine is similar to that in an induction machine. A synchronous machine differs from an induction machine only in the rotor geometry and structures. The rotor of a synchronous machine is excited by the field winding, which is nonexistent in an induction machine.

Synchronous machines are classified into salient-pole machines and cylindrical-rotor machines depending on their rotor configuration. The construction of a salient-pole synchronous machine is shown schematically in Figure 2-2 (a). The rotors of this kind of machines have obviously salient poles with concentrated field winding surrounding the pole bodies. By properly shaping the pole face, a nonuniform air gap is usually obtained to make the radial air-gap flux density to approximate a sinusoidal distribution. A cylindrical-rotor synchronous machine has a round rotor with distributed field winding and uniform air gap as shown in Figure 2-2 (b). The coil sides are distributed in multiple slots around the rotor periphery and arranged to produce an approximately sinusoidal distribution of radial air-gap flux density.

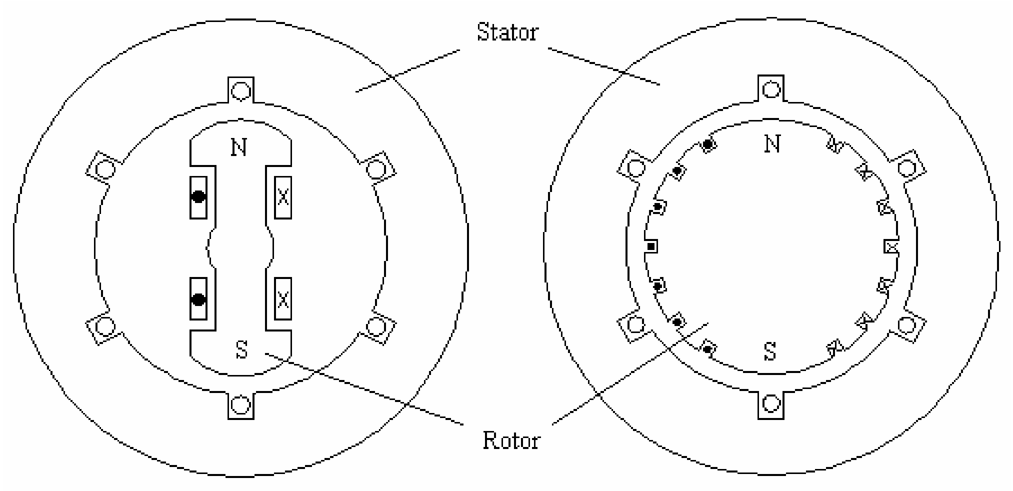

(a) Salient-pole machine (b) Cylindrical-rotor machine

Figure 2-2 Construction of synchronous machines

Some synchronous machines may have an amortisseur winding on the rotor. Salient-pole machines normally have amortisseur winding in the form of conductive bars spaced across each pole face. The ends of the bars are brazed to a pair of conductors to form a low-resistance path. This configuration of amortisseur winding is similar to the squirrel cage in an induction machine. There are two basic types of amortisseurs. Nonconnected amortisseur windings are isolated on each pole face. Connected amortisseurs have conducting bridges that interconnect all the amortisseur groups at individual poles. The main purpose of amortisseur is to dampen oscillations about synchronous speed that result from electrical or mechanical perturbations. It is also used to accelerate the machine during starting. As the rotating field moves past the winding during oscillations or starting it induces currents in the amortisseur winding which produce torque and accelerate or decelerate the machine. In this process the amortisseur winding works exactly the same way as the squirrel cage in an induction machine.

2.2.2 Harmonics and stray losses in synchronous machines

Some harmonics in a synchronous machine are produced in a way similar to the harmonics occurring in an induction machine. For instance, all the slots around the periphery of iron cores and the nonsinusoidal spatial distribution of stator windings produce space harmonics modulating the machine fundamental field. In addition, a power grid may input time harmonics into the synchronous machines connected to it.

The field winding of a synchronous machine is excited with DC current, which produces fundamentally a DC rotor field. Thanks to the shape of pole face (in salient-pole machine) or the configuration of field winding (in cylindrical-rotor machine), the spatial distribution of air-gap flux density is approximately sinusoidal. As the air-gap flux rotates with the rotor, a sinusoidal field presents on the stator at the fundamental frequency corresponding to the synchronous speed. However the DC excitation in synchronous machines still produces rotor magnetomotive force (MMF) harmonics though the rotor construction has been specially arranged to mitigate the impact of these harmonics on air-gap flux density. Thus the nonsinusoidal air-gap flux due to the DC excitation creates an additional harmonic source in a synchronous machine.

Unlike the circumstances in an induction machine, the rotor of a synchronous machine in steady state does not carry any field or induced current at slip frequency, because the rotor motion is in synchronism with the stator fundamental rotating field. Thus DC rotor field fundamentally produces no loss in the rotor core and the amortisseur winding. However, as the effect of harmonics introduced by internal structures and external supply, the AC components of the rotor field and the induced current in amortisseur winding produce a considerable amount of rotor loss. The rotor loss and the stator harmonic loss constitute the harmonic stray losses in synchronous machines. It is postulated that interbar currents also occur in the rotor of a synchronous machine and cause an additional stray loss, for construction and manufacturing process of amortissuer are similar to those of the squirrel cage in an induction machine. However, to the author’s knowledge, no previous work on interbar currents in synchronous machines has been published prior to the work carried out for this thesis.

2.2.3 Determination of stray loss by experiment

Similar to IEEE Standard 112, some segregated losses are defined in IEEE Standard 115 for synchronous machines. These losses include friction and windage loss, core loss (on an open circuit), stray-load loss (on a short circuit), armature I^2R loss and field I^2R loss. The standard provides an experiment guide to determine the efficiency by measuring those segregated losses [5]. The loss components of core loss and stray-load loss due to harmonic, leakage and fringing flux constitute the stray losses at open and short circuit respectively. This experiment guide is based on a false assumption that the superposition of the core loss at an open circuit and the stray-load loss at a short circuit can simulate precisely the actual load loss in a synchronous machine. Ideally, the direct measurement of stray losses under the actual load condition is required for determination of efficiency. In [3] a measurement of stray losses throughout the entire geometry of a synchronous machine is carried out by using miniature thermistors and thin film area sensors.

2.3 Permanent magnet synchronous machines

A PMSM is similar to a synchronous machine with the exception that the field winding is replaced by permanent magnet. In comparison to conventional synchronous machines, the excitation by permanent magnet does not need the parts such as external DC supply, slip rings, brushes, and hence requires no maintenance cost for those parts. PMSMs are typically operated from variable-frequency drives and behave similarly to conventional synchronous machines. PMSMs have high power density, high efficiency and are relatively simple to control. These advantages make PMSMs an attractive candidate for industrial drive, servo drive, electric vehicle traction drive and motion parts in home appliances such as washing machine, refrigerator and air conditioning.

2.3.1 Rotor construction of permanent magnet synchronous machines

PMSMs are classified as surface-mounted permanent magnet (SPM) and interior-mounted permanent magnet (IPM) types. The SPM machine has its magnets projected from the surface of the rotor, while the IPM machine has its magnets buried inside the rotor. The cross sections of the two types of machine are schematically shown in Figure 2-3. In practice, the geometry of the permanent magnets and the rotor core may vary depending on individual applications in order to obtain sinusoidal spatial distribution of air-gap flux density, and desired direct and quadrature axis inductance (L_d and L_q). In a SPM machine, epoxy glue, special tape or retaining sleeve is used to fix the magnets to the rotor surface. This design makes SPM machines easy to build and less expensive, but less robust compared to IPM type, especially in high-speed applications. The rotor of an IPM machine possesses salient magnetic structure that favours development of a reluctance torque component and helps increase flux density. This extra torque component can be harnessed to increase output with a more sophisticated control algorithm. The main disadvantage of IPM machines is the large cogging torque that may cause noise and vibration.

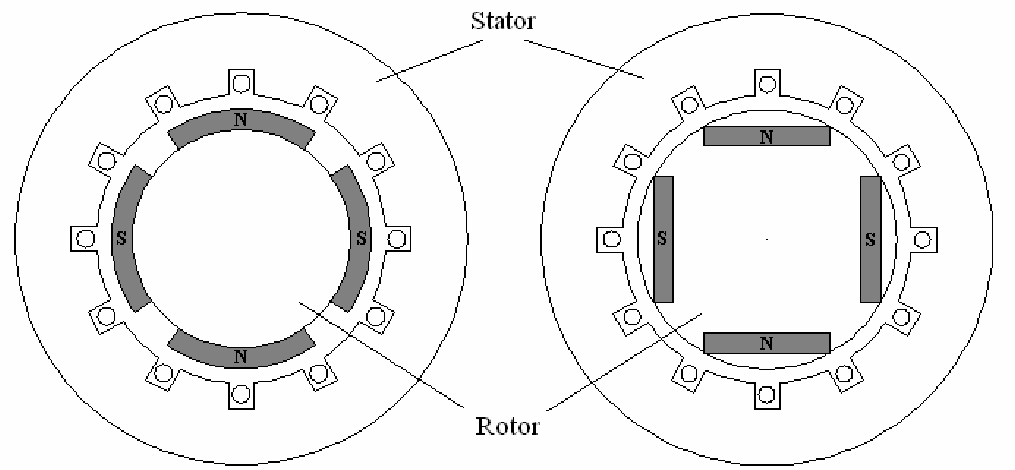

(a) Surface-mounted permanent magnet (b) Interior-mounted permanent magnet

Figure 2-3 Construction of permanent magnet synchronous machines

2.3.2 Harmonics and stray losses in permanent magnet synchronous machines

Slots in the core periphery, nonsinusoidal spatial distribution of stator windings and nonsinusoidal supply (if presents) are all common sources of harmonics in conventional synchronous machines and PMSMs. Analogous to DC field winding in conventional synchronous machines, MMF of permanent magnets in PMSMs contains harmonics and results in air-gap flux density which is not perfectly sinusoidal, though efforts have been made to reduce effect of these harmonics by shaping magnets and rotor core. Thus the nonsinusoidal MMF of permanent magnets produces an additional portion of stray loss in a PMSM.

Supply and slot harmonics induce eddy currents in permanent magnet, rotor iron core and conductive retaining sleeve, if present. These eddy currents may produce significant stray losses at high speeds by heating the rotor. The rotor temperature rise caused by these stray losses is a special concern in design of PMSMs. The property of permanent magnet is sensitive to temperature. Residual flux density (B_r) and coercive force (H_c) decrease as magnet temperature increases. This characteristic is unfavourable for the permanent magnet performance, particularly the demagnetization withstand, whose degradation increases the risk of demagnetization in the case of transients or field-weakening control. In addition, if the magnet is unfortunately heated to over its Curie temperature, irreversible demagnetization will occur to the magnet and lead to a permanent damage to the machine. It is technically difficult to construct a cooling system for the moving part inside an electric machine, thus a design with low rotor stray losses is expected to keep the rotor temperature in a safe range. A conventional approach to reduce the magnet loss is to divide the solid magnets into a number of insulated segments.

2.4 Time-stepped finite element model

2.4.1 Finite element methods for AC machine analysis

For simulation of electric machine performances, two major finite element models have been established: time-harmonic FEA and time-stepped FEA. Time-harmonic FEA relies on “one snapshot” rotor position in calculating the phasor-based performance characteristics in frequency domain by treating the supply as a current phasor. This method can model only the effects of time harmonics as the result of nonsinusoidal supply. The effects of saturation and space harmonics caused by rotor motion cannot be investigated using such a linear field modeling method in frequency domain. As the induced currents in core laminations, squirrel cage (or amortisseur windings) and permanent magnets are an outcome of the interacting supply and space harmonics, a more accurate model is required when evaluating the full effect of harmonics. Time-stepped FEA calculates machine electrical and magnetic performances at samples of rotor position. With the dynamic creation of finite element mesh (for a machine's air gap only, in practice) this method inherently reflects the full effect of harmonics and saturation. This method has been employed in the simulations of nonsinusoidal field in induction machines since 1980's [14] - [17], and it was extended in 1990's to simulate the performances of conventional synchronous machines and PMSMs [18] - [21]. The authors of [14] - [19] simulate the steady-state electromagnetic performances of AC machines by solving the coupled electric circuit equations and finite-element field equations. To implement a comprehensive simulation of electromechnical performances such as the transients during starting and supply or load perturbation, this method has been improved by coupling an additional mechanical equation with the electromagnetic system equations. In [20] and [21] the starting transient of line-start PMSM is simulated by solving simultaneously those mechanical and electromagnetic equations.

There are two approaches to implement time-stepped FEA on the electromagnetic system of AC machine: coupled circuit approach [22] and eddy-current approach [23]. The coupled circuit approach is based on a circuit model comprised of time varying circuit equations coupled to a magnetostatic finite element model. The finite element model is used to update the self and mutual inductances of the circuit as the orientation of the rotor and the magnetic saturation vary. The eddy-current approach calculates the unknown circuit variables with the present change rate of magnetic potential, in other words, the field and circuit equations are solved simultaneously at each time step. This approach has the advantage that the full effect of instantaneous induced currents and electromotive forces (EMF) is directly included in the simulation results. The investigation of the two approaches show that the simulation based on the eddy-current model is significantly faster than that based on the coupled circuit model [24], [25].

2.4.2 Multislice technique

Skewed slots are extensively adopted in AC machines as a design routine in order to reduce harmonics, noise and vibration. The center line of a skewed slot is not a straight line parallel to the axis of the machine, but is a spiral line along the cylinder (for instance, the surface of the rotor). In small or medium size induction machines, slot skewing is usually done on rotors. Slot skewing in synchronous machines and PMSMs, if presents, is usually done on stators. Conventionally, the slot pitch or the angle a skewed slot crosses on the surface of rotor or stator cylinder is used as the measure of skew. One slot pitch is an arc covering one slot and one tooth of the stator.

Skewed slots result in axial variation of flux density that needs 3-D modeling technique. The 3-D finite element model requires extremely expensive overhead in computation, which makes it impractical to simulate AC machines by time-stepped 3-D technique. To simplify the modeling of induction machines with skewed rotor slots and reduce the computation time, the multislice technique has been exploited that models the skew by a set of slices cut from the machine using planes perpendicular to the machine's axis [26], [27]. The multislice model of a skewed slot is shown in Figure 2-4. The bar lying in a skewed slot is represented by the axial bar segments which are discretized by the slices and shifted parallel to one another on the surface of rotor cylinder, but electrically connected in series. The angle across the adjacent bar segments is dependent on the value of skew

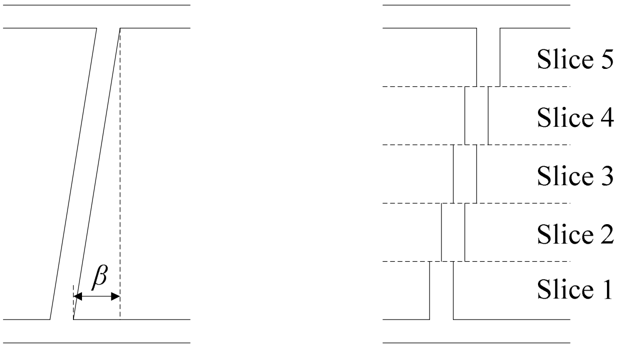

(a) Skewed slot (b) Discrete approximation

Figure 2-4 Multislice model (5-slice example) angle and the number of slices. As the bar segments within slices are assumed parallel to the machine’s axis, the magnetic field on each slice can be modeled using 2-D finite elements. The currents flowing in bars and windings are continuous across the discrete slices, and the magnetic fields on these slices are coupled together through the electric circuit equations with those continuous currents.

2.4.3 Interbar circuit model

As mentioned in Section 2.1.2 rotor interbar currents contribute to the axial variation in bar currents as well as machine field. A number of previous authors attempted to model these transverse currents using 3-D technique. In [28] and [29] two similar algorithms based on the coupled 2-D and 3-D models are adopted to compute the rotor stray losses caused by interbar currents in induction machines. Both algorithms employ a 2-D multislice time-stepped finite element model as the first step to compute the stator current, rotor current and the 2-D field distributions at each time step. The presence of interbar currents is neglected in the 2-D analysis. In the following step the harmonics in the 2-D solution are identified and then 3-D FEA in frequency domain is carried out at each remarkable harmonic in order to obtain the detailed information on rotor field and interbar currents. The introduction of 3-D models leads to a large amount of computational effort in solving interbar current problems. The computation required in the pre- and post-processing of 3-D FEA data is also complex [30]. On the other hand, these coupled 2-D and 3-D models are not a complete time-stepped solution because the effect of interbar currents is not directly included in the initial 2-D time-stepped models; in addition, the 3-D analysis in frequency domain cannot be used to predict the transient nonlinear variation of the field.

An alternative to the coupled 2-D and 3-D models is the 2-D multislice interbar circuit model. In [30] and [31], the interbar insulation is modeled using the lumped transverse resistances in a multislice rotor circuit, rather than the 3-D finite elements as in [28] and [29]. In this rotor circuit, the bar impedances are included as a part of the 2-D time-stepped finite element model; the end-ring impedances and the interbar resistances constitute a circuit external to the finite element model. Thus the finite-element equation of rotor field and the interbar circuit equation are coupled together to form a full time-stepped 2-D finite element solution. Figure 2-5 shows two commonly used multislice interbar circuit models (3-slice examples). The bar-bar model in Figure 2-5 (a) is based on the usually accepted assumption that interbar currents flow directly between adjacent bars. However the iron resistance is usually much smaller than the bar-iron contact resistance; more logically, the interbar currents will enter the iron through the bar-iron contact resistances and then circulate in the iron core, rather than flow to the adjacent bars through the high resistance bar-iron path. This pattern of interbar currents is embodied in the bar-iron model, which is a cubic network shown in Figure 2-5 (b) [32], [33]. In [30] and [31] the bar-bar model is integrated with the 2-D time-stepped multislice FEM. In a recent publication, [34], the bar-iron model is applied with the multislice model created by 2-D finite element commercial software.

The interbar resistances (R_{bb} or R_c in Figure 2-5) are inconstant parameters in an induction machine. They may vary significantly with the individual machines, or even with the different bars in a single machine, depending on manufacturing

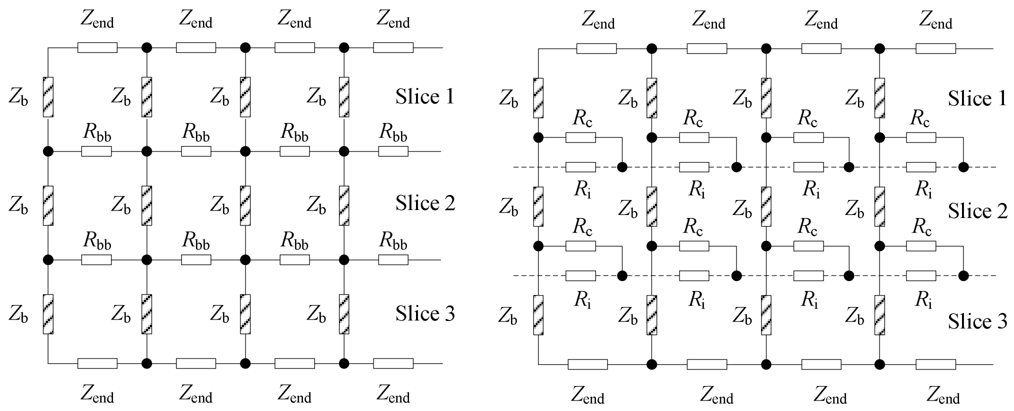

(a) Bar-bar model (b) Bar-iron model

Z_b – Impedance of bar segment Z_{end} – Impedance of end-ring segment

R_{bb} – Bar-bar resistance R_c – Bar-iron contact resistance R_i – Iron resistance

——— Cage circuit or bar-iron circuit ▨ Part of finite element model

------- Iron circuit ▭ External to finite element model

Figure 2-5 Interbar circuit model (3-slice examples) process and ageing [32], [35]. As examples, bar and slot diameter manufacturing tolerances, thermal expansion coefficients and oxide formation on surfaces may all affect the surface contact resistance between the bar and the iron core. For this reason, the estimation of interbar resistances is subject to a large amount of experimental effort [35], [36]. Depending on the values of interbar resistances, noticeable variations of machine performances may occur, e.g., starting torque [7], [37], torque-speed characteristic [38], harmonic related performances such as rotor harmonic Joule loss [38], torque and stator current ripples [31].

2.4.4 Computational efficiency of multislice time-stepped finite element method

The multislice modeling technique for skewed induction machines has been summarized in Section 2.4.2. This section reviews the numerical technique developed recently to solve the nonlinear equation based on the multislice model. Generally, FEA of saturated field needs Newton-Raphson (N-R) numerical iterative technique to solve nonlinear equations. Multislice time-stepped FEM iterates at each time step the process of solving the circuit equation and the field equations on multiple slices. Although the multislice time-stepped technique has avoided the infeasibility of fully time-stepped 3-D modeling, the computational overhead is still a significant drawback which limits its application in day-to-day analysis and design of electric machines. It is essential to improve the computational efficiency in order to broaden the application of multislice time-stepped FEM.

A. Transmission line modeling method

Transmission line modeling (TLM) method is a technique that is used for nonlinear electric circuit analysis. Previous authors borrowed TLM as a replacement numerical technique for N-R method to save the computation time in solving 2-D nonlinear magnetostatic and magnetodynamic problems [39], [40]. The N-R iterative solution to a nonlinear finite-element field equation has the following form:

$$\mathbf{S}_k \Delta \mathbf{A}_{k+1} = \mathbf{F}_k \tag{2-1}$$

where $\mathbf{S}_k$ is Jacobian matrix, $\mathbf{F}_k$ is forcing term and $\Delta\mathbf{A}_{k+1} = \mathbf{A}_{k+1} - \mathbf{A}_k$ are nodal magnetic potentials. At each N-R iteration both $\mathbf{S}_k$ and $\mathbf{F}_k$ need to update, however this costs intensive computational effort as the N-R solution to a multislice finite element model produces a large-scale Jacobian matrix. The TLM iterative solution to a nonlinear field finite-element equation has the following form:

$$\mathbf{S}_0\mathbf{A}_k = \mathbf{F}_{\mathrm{TLM}\,k} \tag{2-2}$$

where $\mathbf{S}_0$ is reconstructed only prior to the first TLM iteration within each time step, and then maintained constant until the next time step; the right-hand side term, $\mathbf{F}_{\mathrm{TLM}\,k}$, embodies the nonlinearity of this equation, and is updated at each TLM iteration. Thus, within each time step the TLM method needs to update only $\mathbf{F}_{\mathrm{TLM}\,k}$ which takes significantly less time than updating both $\mathbf{S}_k$ and $\mathbf{F}_k$ by N-R method. However the TLM method has a linear rate of convergence [39], which leads to more iterations to obtain convergence than the quadratically convergent N-R method. As this feature negates the advantage of TLM method in saving the computation time for reconstruction of large-scale matrix, this method alone may not be significantly faster than the N-R method for electric machine analysis.

B. Domain decomposition

Domain decomposition (DD) is also a mathematical method that is introduced to increase the computational efficiency in solving boundary value problems. DD splits a boundary value problem into smaller boundary value problems on subdomains. With the aid of this method the matrix equation constructed for a boundary value problem can be subdivided into a set of equations with reduced number of unknown variables and coefficient matrices of smaller size. Solving that set of equations is more efficient computationally than solving the original one because the computation overhead for solving a matrix equation decreases very fast with the reduced size of the matrix.

For the analysis of a skewed induction machine, a previous author utilizes two levels of DD to solve the multislice numerical equation constructed by TLM method (TLM-DD method) [41]. The first level of DD creates the subdomains by exploiting the rotational symmetry of the finite-element mesh within each slice while the second level of DD subdivides the multislice equation into blocks related to the slices. Thanks to the TLM method the representation of field nonlinearity is moved from the Jacobian matrix on the left-hand side of the numerical equation to the forcing term on the right-hand side. Thus the left-hand side coefficient matrix becomes dependent on the mesh geometry only, irrespective of the field nonlinearity. This feature lends the TLM equation to the first level of DD that utilizes the geometric periodicity of a machine's cross section to define the subdomains for the physical regions covering each stator slot, each rotor slot, plus a single domain for the whole air gap. With the aid of this level of DD, the field equation of the whole domain on each slice is converted to a set of subdomain equations with respect to stator slot, rotor slot and air gap. In these subdomain equations all the stator slot subdomains and all the rotor slot subdomains share the same coefficient matrix respectively, within each time step.

C. Parallel TLM-DD method

As mentioned in Section 2.4.2, in the multislice model of induction machines, the magnetic fields on the slices interact on one another through the electric circuit of stator and rotor. By utilizing the absence of direct magnetic coupling between the slices, the second level of DD splits coefficient matrix and vector of unknown variables into blocks related to magnetic potentials on individual slices and circuit variables, respectively. With this level of DD, the calculations of nodal magnetic potentials on an individual slice are independent of other slices once the values of circuit variables are obtained. These calculations take a large amount of simulation time, but fortunately they can be carried out in parallel since the calculation related one slice requires no result from the calculation related to any other slice. The TLM-DD method brings a significant improvement of computational efficiency to the multislice model of skewed induction machines, especially when the calculations based on the multislice-level DD are implemented in parallel [41].

2.5 Loss evaluation based on 2-D time-stepped finite element analysis

Previous sections have clarified that AC machine losses may occur in windings, squirrel cage or amortisseur, interbar regions, permanent magnets and core laminations. These losses can be evaluated using the data of current and magnetic flux density obtained from multislice time-stepped FEA.

2.5.1 Losses in windings and interbar regions

The evaluation of losses in windings and interbar regions is straightforward. The windings and interbar regions are treated as lumped resistances, and the currents flowing in these resistances are predicted by the finite element simulation. The Joule losses in the windings and interbar regions are computed using the lumped resistances multiplied by the square of the currents.

2.5.2 Losses in solid conductors

Due to the skin effect the density of induced currents is not uniformly distributed in the cross sections of solid conductors such as squirrel cage or amortisseur bars and permanent magnet. For this reason these conductors cannot be treated as lumped resistance when predicting the Joule losses caused by the induced currents. It is necessary to first compute the Joule loss of each element from the local current density predicted by FEM and then add these element losses together. As a 2-D model does not mesh the end-ring regions of a squirrel cage or amortisseur, the effect of the electromagnetic field in these regions is reckoned in using the lumped resistances and inductances across the ends of adjacent bars (Z_{end} in Figure 2-5). The Joule losses in end rings are obtained from the lumped end-ring resistances multiplied by the square of the end-ring currents.

2.5.3 Iron loss

The evaluation of the loss in core laminations (iron loss) is less straightforward in comparison to the losses mentioned above. Iron loss is actually the sum of three components: eddy-current loss, hysteresis loss and excess loss due to domain wall effects. Modeling and calculation of these iron loss components have been investigated in a lot of literature. Modeling the eddy-current loss explicitly usually requires the computationally expensive 3-D FEA [42], since the eddy currents flowing along the laminations are not compatible with the 2-D analysis of the field in a machine's cross section. Hysteresis losses and excess losses in laminations can be directly accounted for by incorporating the Preisach hysteresis model with a time-stepped 2-D scheme [43], [44]. Although a lot of different Preisach models have been proposed over the years for evaluation of electric machine iron losses [45] - [49], it requires a very complicated algorithm to directly incorporate a Preisach model with the time-stepped 2-D finite element model of an electric machine, and this algorithm is very expensive computationally [50]. On the other hand, electric machine manufacturers usually do not have the data necessary to establish a Preisach model for the ferromagnetic laminations. Due to the above difficulty in direct inclusion of the iron losses into a time-stepped finite element solution, a more common practice is to disregard the iron losses and replace the Preisach model with a single-valued B-H curve for the laminations during the time-stepped 2-D finite element solution. The iron loss components can be evaluated a posteriori as a part of the post-processing, from the instantaneous flux densities obtained by the 2-D FEA. The three basic equations used to calculate the iron loss components are shown in [51] and cited below.

A. Eddy-current loss

The eddy-current loss density (in W/m^3) in laminations, P_e, is given by the following classical equation:

$$P_\mathrm{e} = \frac{\sigma_\mathrm{m} d^2}{12T} \int_T \left(\frac{\mathrm{d}B}{\mathrm{d}t} \right)^2 \mathrm{d}t \qquad (2\text{-}3)$$

where σ_m is lamination conductivity, d is lamination thickness, B is flux density, and T is period of fundamental flux density. This equation is based on the assumption that the flux densities in laminations do not vary in the normal direction, thus it is valid for thin laminations only where the skin depth of flux density is greater than the lamination thickness.

B. Hysteresis loss

The hysteresis loss density (in W/m^3) in laminations, P_h, can be calculated using an empirical formula

$$P_\mathrm{h} = k_\mathrm{h} \rho f \hat{B}^{\alpha} K(\hat{B}) \tag{2-4}$$

where f is fundamental frequency of flux density, ρ is lamination mass density, $\hat{B}$ is peak value of flux density, k_h and α are constants determined by fitting a P_h - $\hat{B}$ experimental curve. $K(\hat{B})$ is an empirical correction factor proposed in [52] in order to take into account the losses caused by minor hysteresis loops.

$$K(\hat{B}) = 1 + \frac{k}{\hat{B}} \sum_i \Delta B_i \tag{2-5}$$

ΔB_i is the change in flux density during the excursion at a minor loop, as shown in Figure 2-6. k is a constant between 0.6 and 0.7, depending on the material being considered. The value of 0.65 is used for k in [51].

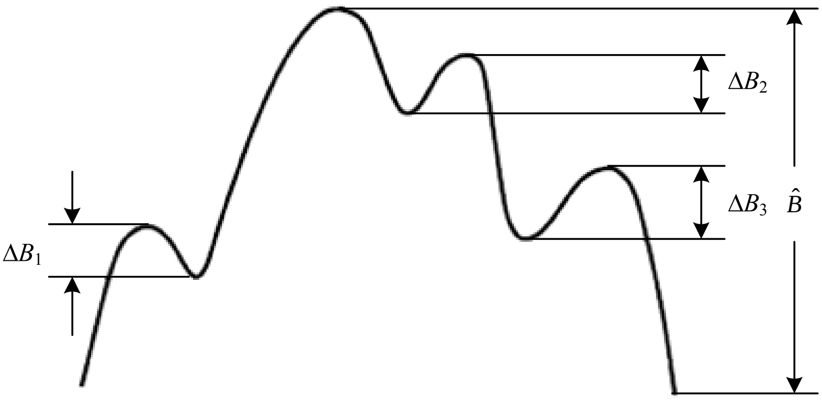

Figure 2-6 Flux density waveform with reversals

C. Excess loss

The following empirical formula can be used to calculate density of excess loss (in W/m^3)

$$P_\mathrm{ex} = \frac{k_\mathrm{e} \rho}{T} \int_T \left| \frac{\mathrm{d}B}{\mathrm{d}t} \right|^{1.5} \mathrm{d}t \tag{2-6}$$

k_e is excess loss constant determined from experiments.

For an AC machine modeled by multislice FEM, one needs to carry out the calculations shown in (2-3) to (2-6) in each lamination element on each slice to work out the total iron loss.

2.6 Design optimization of AC machines for minimum loss

An important aspect of research on AC machine losses is to investigate the influence of different configurations of machine structures and parts on the variations of machine losses including the local losses in specific parts and the total losses in a whole machine. The goal of design optimization in this thesis is to locate the optimal configuration with the minimum loss from a variety of choices. There are a number of target structures selected for loss minimization or efficiency maximization in previous contributions. Some authors attempts to improve machine design by changing some fundamental variables that are used to sketch out the geometry and dimensions of the main parts [53] - [59]. Examples for these parameters include

1. Stator bore diameter
2. Length of laminated iron core stack
3. Height of stator yoke
4. Mean width of stator slot
5. Width of stator slot opening
6. Rotor shaft diameter, etc

and the following if an induction machine,

7. Height of rotor slot
8. Mean width of rotor slot
9. Width of rotor slot opening, etc

or the following if a PMSM,

10. Magnet thickness
11. Magnet pole angle, etc

Other authors focus on the design improvement of a specific type of structure, e.g., the stator slot [60] or the rotor slot [61]. A range of key points on a slot’s outline are defined to describe the detailed geometry of the slot, and the various designs of geometry are implemented by changing the relative locations of these points.

2.6.1 Loss evaluation

In the process of seeking the optimal design with the minimum loss, one needs to evaluate the machine losses of various candidate designs, and the accuracy of these evaluation results is an important factor affecting the reliability of the final optimal result. In the publications mentioned in the previous section, the various design optimization methods for PMSM rely on analytical models to evaluate machine losses [55] - [59]. With these analytical models for loss evaluation, the stray losses such as the harmonic losses in iron laminations and permanent magnets are actually neglected [55], [56], [58], [59], or in a better case, assumed as a constant percentage of the output power [57]. In [54], [60] and [61], the design optimization of induction machines employs FEM to relatively accurately predict the flux density distribution, however these methods involve the use of either equivalent circuit of induction machine or time-harmonic FEM, whichever is still lack of accuracy in harmonic loss calculation. To the author’s knowledge, the time-stepped eddy-current FEA is unfortunately unpopular in machine optimization due to the excessive time penalty being incurred. Due to the absence of precise prediction of machine field and current density distribution, the harmonic stray losses are simply neglected or estimated inaccurately at the stage of loss evaluation in most of the previous work on design optimization of AC machines.

2.6.2 Optimization algorithms review

Solving an optimization problem is an iterative process of evaluating the performance of the current candidate, rearranging the objective variable value(s) of the current candidate, and selecting the next candidate until this process converges to the solution with the optimal performance. An optimization algorithm is a numerical method that mathematically defines this process. Deterministic method and stochastic method are two families of algorithms applied to engineering optimization problems.

A deterministic optimization method always converges to the same optimal value via the same route, if it repeatedly starts the seeking procedures from the same initial candidate. This optimization family includes a wide variety of commonly used techniques such as interval cutting methods, Newton's method, steepest descent method, conjugate gradient method, etc [62]. At each iteration in these optimization processes the new candidate must be compared to the previous candidate to determine the better one.

Stochastic optimization methods refer to a family of methods that introduce randomness into the search process as a means of speeding convergence and weakening the algorithm's sensitivity to modeling errors. There are a large number of members in this family, such as direct random search methods [63], simulated annealing [64], evolutionary algorithms [65], [66], etc. The probability introduced into these algorithms may provide the necessary impetus to escape from a local solution by allowing some candidates inferior to the previous ones to be accepted in the optimization process.

Evolutionary algorithms denote a category of stochastic optimization methods that use mechanisms inspired by natural selection and survival of the fittest in the biological world. This family of optimization methods includes three similar techniques: genetic algorithm (GA), evolution strategy (ES) and evolutionary programming (EP), which have been developed independently since the late 1950's. One of the main advantages of evolutionary algorithms is that they are not selective to the mathematical form of the optimization problem. All they need about the object to be optimized is an evaluation of objective function, thus they can handle a wide variety of linear or nonlinear problems defined on continuous, discrete or mixed search spaces, and even the problems that cannot be explicitly defined by analytical objective functions [67]. Another advantage of evolutionary algorithms is the capability for self-optimization. The performances of some optimization techniques are dependent on the settings of exogenous variables that are used to control the optimization algorithms themselves. Evolutionary algorithms (e.g., ES, self-adaptive GA and self-adaptive EP) may optimize these parameters as part of the optimum seeking process itself to adapt the algorithms to specific optimization problems [67]. Thanks to their broad applicability, evolutionary algorithms (e.g., GA) have been commonly used in design optimization of AC machines for minimum loss or maximum efficiency [54] - [59].

2.6.3 Constrained optimization problem

The optimal design of an electric machine must satisfy a number of technical requirements according to the relevant standards and the specific applications. For example, the requirements placed on induction machine design may include efficiency and power factor at rated load, locked-rotor torque, pullout torque, locked-rotor current, manufacturing cost, etc. On the other hand, in the process of optimization, the variation of each design variable must be confined into a feasible range that is determined by the physical dimension limits of the machine structures. Consequently, machine design optimization is mathematically a constrained optimization problem.

A straightforward approach to handle these constraints is expressing them using a range of inequalities in terms of those technical variables and design variables, and the optimization algorithm discards the infeasible candidate solutions that violate any of those inequalities. An alternative approach is incorporating penalty functions with an objective function. Penalty functions use the amount of constraint violation to “punish” an infeasible candidate solution so that feasible solutions are favored by the search process. The penalty function approach is commonly used to handle those constraints determined by the technical requirements [54], [56], [61].

Chapter 3 Numerical Models

The modeling of some common structures in AC machines is similar, irrespective of the type of machine. The time-stepped multislice eddy-current finite element model of skewed induction machines is presented in this chapter as a representative. The modeling of the structures particular to synchronous machines and PMSMs is presented in Chapter 5 and Chapter 6, respectively. In this thesis the finite element models of AC machines are developed based on the following assumptions:

1. Within each slice of a multislice model the flux densities have no axial variations and can be modeled using 2-D finite elements;
2. As mentioned in Section 2.5.3, the magnetization property of lamination material can be characterized by a monotonic *B*-*H* curve, hysteresis losses are modeled and evaluated using (2-4) outside the finite element model;
3. The eddy currents in laminations are sufficiently small and therefore can be excluded from the finite element model, eddy-current losses and excess losses are evaluated using (2-3) and (2-6) outside the finite element model, as mentioned in Section 2.5.3;
4. There is no skin effect in the stranded conductors (i.e. the windings), the winding currents are uniformly distributed in the cross section of each coil side.

3.1 Field equations

Considering that the electromagnetic field in an electric machine is quasi-static, the general form of electric machine field equation can be derived from Maxwell's equations:

$$\nabla \times (v \nabla \times \mathbf{A}) = \mathbf{J} \tag{3-1}$$

A is magnetic vector potential, **J** is current density, and v is reluctivity. In the 2-D multislice model of a skewed induction machine, (3-1) can be rewritten as follows for the different regions in the *i*th slice:

For the regions of laminations,

$$\frac{\partial}{\partial x}\left(\nu_{\mathrm{m}}\frac{\partial \mathbf{A}_{\mathrm{sl}i}}{\partial x}\right)+\frac{\partial}{\partial y}\left(\nu_{\mathrm{m}}\frac{\partial \mathbf{A}_{\mathrm{sl}i}}{\partial y}\right)=0 \tag{3-2}$$

For the air regions,

$$\nu_0\frac{\partial^2 \mathbf{A}_{\mathrm{sl}i}}{\partial x^2}+\nu_0\frac{\partial^2 \mathbf{A}_{\mathrm{sl}i}}{\partial y^2}=0 \tag{3-3}$$

For the regions of stator coil sides,

$$\nu_0\frac{\partial^2 \mathbf{A}_{\mathrm{sl}i}}{\partial x^2}+\nu_0\frac{\partial^2 \mathbf{A}_{\mathrm{sl}i}}{\partial y^2}=-\frac{\gamma N_{\mathrm{t}} I_{\mathrm{s}}}{N_{\mathrm{c}}\Delta_{\mathrm{cs}}} \tag{3-4}$$

For the region of *j*th rotor bar,

$$\nu_0\frac{\partial^2 \mathbf{A}_{\mathrm{sl}i}}{\partial x^2}+\nu_0\frac{\partial^2 \mathbf{A}_{\mathrm{sl}i}}{\partial y^2}=-\sigma_{\mathrm{b}}\left(\frac{V_{\mathrm{b}ij}}{L_{\mathrm{sl}}}-\frac{\partial \mathbf{A}_{\mathrm{sl}i}}{\partial t}\right) \tag{3-5}$$

$\mathbf{A}_{\mathrm{sl}i}$ is the *z*-component of magnetic vector potential on the *i*th slice (*z*-component is parallel to machine axis), I_{s} is the stator phase current, and $V_{\mathrm{b}ij}$ is the voltage over the segment of *j*th rotor bar within the *i*th slice, i.e. Z_{b} in Figure 2-5. N_{t} is number of turns per stator coil, N_{c} is number of stator circuits in parallel, Δ_{cs} is cross-sectional area of stator coil side, γ is ±1 depending on direction of coil side, σ_{b} is rotor bar conductivity, L_{sl} is axial length of machine core in each slice, and ν_0 is reluctivity of air, stator windings and rotor bars. ν_{m} is reluctivity of laminations, and it is a function of the lamination field.

3.2 Electric circuit equations

Applying Kirchhoff's voltage law (KVL) to the stator circuit gives the following equation,

$$\mathbf{V}_{\mathrm{s}}=\frac{N_{\mathrm{t}}L_{\mathrm{sl}}}{N_{\mathrm{c}}}\sum_{j=1}^{N_{\mathrm{cs}}}\left[\frac{\gamma_j}{\Delta_{\mathrm{cs}j}}\sum_{i=1}^{N_{\mathrm{sl}}}\iint_{\Delta_{\mathrm{cs}j}}\frac{\partial \mathbf{A}_{\mathrm{sl}i}}{\partial t}\mathrm{d}S\right]+R_{\mathrm{s}}\mathbf{I}_{\mathrm{s}}+L_{\mathrm{ew}}\frac{\mathrm{d}\mathbf{I}_{\mathrm{s}}}{\mathrm{d}t} \tag{3-6}$$

where $\mathbf{V}_{\mathrm{s}}$ is a vector of polyphase supply voltages, $\mathbf{I}_{\mathrm{s}}$ is a vector comprised of the individual phase currents of stator (i.e. I_{s}), N_{cs} is number of coil sides per phase, N_{sl} is number of slices, R_{s} is stator phase resistance, and L_{ew} is end-winding inductance. The first term on the right-hand side of (3-6) is the induced EMF due to the magnetic flux through the stator coils.

The bar-iron type of interbar circuit model as shown in Figure 2-5 (b) is used for the proposed induction machine simulations. Some loop currents are defined in this model to develop the rotor circuit equations. Figure 3-1 shows two options for the definition of loop currents in that circuit model (only three representative loop currents are shown). The conventional definition of loop currents is shown in Figure 3-1 (a), where all the loop currents are linked with the interbar resistances. In case of insulated bars the large interbar resistances limit all the loop currents in the conventional definition to very small values that may lead to numerical instability. In this thesis an alternative definition of loop currents is proposed as shown in Figure 3-1 (b). With this definition the loop currents defined as i_{l3} link bar and end-ring impedances only, thus they bypass the potential high-impedance branches. This feature of the improved definition may enhance the numerical stability for the special case of insulated bars, and make feasible the simulations for a wide range of interbar resistances.

With this improved definition of loop currents the voltages over rotor bar segments (Z_b) within the slices are given by the following equation:

$$\mathbf{V}_\mathrm{b} = -\frac{R_\mathrm{b}}{N_\mathrm{sl}}\mathbf{M}\mathbf{I}_\mathrm{r} + \frac{L_\mathrm{sl}}{\Delta_\mathrm{b}}\begin{bmatrix} \iint\limits_{\Delta_{\mathrm{b}1}} \frac{\partial \mathbf{A}_{\mathrm{sl}1}}{\partial t}\mathrm{d}S \\ \vdots \\ \iint\limits_{\Delta_{\mathrm{b}N_\mathrm{b}}} \frac{\partial \mathbf{A}_{\mathrm{sl}1}}{\partial t}\mathrm{d}S \\ \iint\limits_{\Delta_{\mathrm{b}1}} \frac{\partial \mathbf{A}_{\mathrm{sl}2}}{\partial t}\mathrm{d}S \\ \vdots \\ \iint\limits_{\Delta_{\mathrm{b}N_\mathrm{b}}} \frac{\partial \mathbf{A}_{\mathrm{sl}2}}{\partial t}\mathrm{d}S \\ \vdots \\ \iint\limits_{\Delta_{\mathrm{b}1}} \frac{\partial \mathbf{A}_{\mathrm{sl}N_\mathrm{sl}}}{\partial t}\mathrm{d}S \\ \vdots \\ \iint\limits_{\Delta_{\mathrm{b}N_\mathrm{b}}} \frac{\partial \mathbf{A}_{\mathrm{sl}N_\mathrm{sl}}}{\partial t}\mathrm{d}S \end{bmatrix} \tag{3-7}$$

where $\mathbf{V}_\mathrm{b}$ is defined as a vector comprised of voltages over rotor bar segments, i.e.,

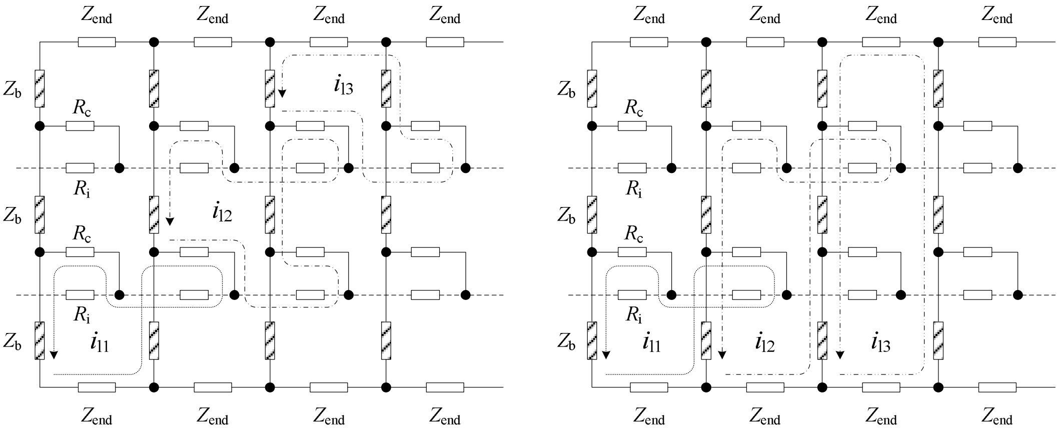

(a) Conventional definition (b) Improved definition

Figure 3-1 Rotor loop currents for induction machines

$$\mathbf{V}_{\mathrm{b}} = \left[V_{\mathrm{b11}}, \cdots, V_{\mathrm{b1}N_{\mathrm{b}}},\ V_{\mathrm{b21}}, \cdots, V_{\mathrm{b2}N_{\mathrm{b}}}, \cdots, V_{\mathrm{b}N_{\mathrm{sl}}1}, \cdots, V_{\mathrm{b}N_{\mathrm{sl}}N_{\mathrm{b}}}\right]^{\mathrm{T}}$$

N_{b} is number of rotor bars, R_{b} is bar resistance, $\mathbf{I}_{\mathrm{r}}$ is a vector comprised of the loop currents, Δ_{b1} to $\Delta_{\mathrm{b}N_{\mathrm{b}}}$ are the cross sections of the 1st to N_{b}th bars, and $\mathbf{M}$ is an $N_{\mathrm{b}}N_{\mathrm{sl}}$-by-$N_{\mathrm{b}}N_{\mathrm{sl}}$ matrix which relates the loop currents to the currents through Z_{b}. The second term on the right-hand side of (3-7) is a vector of induced EMF across bar segments. Applying KVL to the loops in Figure 3-1 (b) one may obtain an additional equation for rotor circuit:

$$\mathbf{M}^{\mathrm{T}}\mathbf{V}_{\mathrm{b}} = \mathbf{R}_{\mathrm{r}}\mathbf{I}_{\mathrm{r}} + \mathbf{L}_{\mathrm{r}}\frac{\mathrm{d}\mathbf{I}_{\mathrm{r}}}{\mathrm{d}t} \tag{3-8}$$

$\mathbf{R}_{\mathrm{r}}$ is a matrix in terms of R_{c}, R_{i} and R_{er} (end-ring segment resistance, the resistive part of Z_{end}). $\mathbf{L}_{\mathrm{r}}$ is a matrix in terms of L_{er} (end-ring segment inductance, the inductive part of Z_{end}). The value of R_{i} is usually negligible in comparison to R_{c} [33], however it is still included in (3-8) for the completeness of interbar circuit model.

This thesis implements time-stepped FEA based on the eddy current approach to investigate steady-state losses of electric machines. This needs the simultaneous solution for a global equation comprised of (3-2) to (3-8) at constant rotor speed. In the global equation $\mathbf{A}_{\mathrm{sl}}$, $\mathbf{I}_{\mathrm{s}}$, $\mathbf{V}_{\mathrm{b}}$ and $\mathbf{I}_{\mathrm{r}}$ are time-varying unknown variables; $\mathbf{V}_{\mathrm{s}}$ is a known time-dependent variable; v_{m} is a variable whose value is determined by experimental samples and spline interpolation for the *B-H* curves of laminations; other parameters are all constant.

3.3 Discretization of system equations

The space- and time-discretized form of (3-2) to (3-8) is developed in this section in order to find the numerical solution of the system equation.

3.3.1 Space discretization

The space discretization is implemented on the machine field domain by the Galerkin FEM [68]. The summation of the finite-element expressions of the terms on both sides of (3-2) to (3-5) forms the general Galerkin formulation of the global multislice field equations:

$$\nu_{\mathrm{e}}\mathbf{S}\mathbf{A}_{\mathrm{N}} = \frac{\gamma N_{\mathrm{t}}}{N_{\mathrm{c}}\Delta_{\mathrm{cs}}}\mathbf{Q}_{\mathrm{s}}\mathbf{I}_{\mathrm{s}} + \sigma_{\mathrm{b}}\left(\frac{1}{L_{\mathrm{sl}}}\mathbf{Q}_{\mathrm{b}}\mathbf{V}_{\mathrm{b}} - \mathbf{T}_{\mathrm{b}}\frac{\mathrm{d}\mathbf{A}_{\mathrm{N}}}{\mathrm{d}t}\right) \tag{3-9}$$

$\mathbf{A}_{\mathrm{N}}$ is a vector of nodal magnetic potentials on all slices, $\mathbf{S}$, $\mathbf{Q}_{\mathrm{s}}$, $\mathbf{Q}_{\mathrm{b}}$ and $\mathbf{T}_{\mathrm{b}}$ are matrices derived by the Galerkin FEM, and ν_{e} are element reluctivities that are multiplied by the corresponding nodal entries of the matrix $\mathbf{S}$ to form the coefficient of $\mathbf{A}_{\mathrm{N}}$. $\mathbf{S}$ is a stiffness matrix dependent on the shapes of all finite elements on all slices. The first term on the right-hand side of (3-9) is nonzero for only the nodes related to stator winding elements, and it contains a matrix, $\mathbf{Q}_{\mathrm{s}}$, which is dependent on the areas of stator winding elements. The term in the brackets is nonzero for only the nodes related to rotor bar elements, and it contains the $\mathbf{Q}_{\mathrm{b}}$ and $\mathbf{T}_{\mathrm{b}}$ matrices which are dependent on the areas of rotor bar elements. In accordance with (3-2) and (3-3) the right-hand side of (3-9) equals zero for the nodes related to air-gap elements and lamination elements. It should be noted that the finite element mesh of rotor is in motion while the time-stepped simulation is running. However, the motion of rotor leads to the deformation of air-gap elements only. As the $\mathbf{Q}_{\mathrm{s}}$, $\mathbf{Q}_{\mathrm{b}}$ and $\mathbf{T}_{\mathrm{b}}$ matrices are determined by stator winding or rotor bar elements, they are constant throughout the time-stepped simulation. $\mathbf{S}$ is related to all finite elements including the deformed air-gap elements, thus the time-dependence of the $\mathbf{S}$ matrix requires consideration.

With the Galerkin FEM all the EMF terms in (3-6) and (3-7) are also converted into expressions in terms of the nodal magnetic potentials. The Galerkin formulations of (3-6) and (3-7) form the following equations:

$$\mathbf{V}_{\mathrm{s}} = \frac{\gamma N_{\mathrm{t}} L_{\mathrm{sl}}}{N_{\mathrm{c}} \Delta_{\mathrm{cs}}} \mathbf{Q}_{\mathrm{s}}^{\mathrm{T}} \frac{\mathrm{d}\mathbf{A}_{\mathrm{N}}}{\mathrm{d}t} + R_{\mathrm{s}} \mathbf{I}_{\mathrm{s}} + L_{\mathrm{ew}} \frac{\mathrm{d}\mathbf{I}_{\mathrm{s}}}{\mathrm{d}t} \tag{3-10}$$

$$\mathbf{V}_{\mathrm{b}} = -\frac{R_{\mathrm{b}}}{N_{\mathrm{sl}}} \mathbf{M}\mathbf{I}_{\mathrm{r}} + \frac{L_{\mathrm{sl}}}{\Delta_{\mathrm{b}}} \mathbf{Q}_{\mathrm{b}}^{\mathrm{T}} \frac{\mathrm{d}\mathbf{A}_{\mathrm{N}}}{\mathrm{d}t} \tag{3-11}$$

With the space discretization by Galerkin method the electromagnetic system of an induction machine is described using the finite-element equations, (3-9) to (3-11), plus the pure circuit equation, (3-8).

3.3.2 Time discretization

To find the numerical solutions for the time-dependent variables, $\mathbf{A}_{\mathrm{N}}$, $\mathbf{I}_{\mathrm{s}}$, $\mathbf{V}_{\mathrm{b}}$ and $\mathbf{I}_{\mathrm{r}}$, (3-8) to (3-11) are required to be discretized in time domain. The time derivative terms in (3-8) to (3-11) can be discretized by Crank-Nicholson (C-N) method [68]. For example, the C-N representation of $\frac{\mathrm{d}\mathbf{A}_{\mathrm{N}}}{\mathrm{d}t}$ is

$$\frac{\mathbf{A}_{\mathrm{N}}^{t+\Delta t} - \mathbf{A}_{\mathrm{N}}^{t}}{\Delta t} = \frac{1}{2}\left(\frac{\mathrm{d}\mathbf{A}_{\mathrm{N}}^{t+\Delta t}}{\mathrm{d}t} + \frac{\mathrm{d}\mathbf{A}_{\mathrm{N}}^{t}}{\mathrm{d}t} \right) \tag{3-12}$$

(3-9) can be rewritten as follows for the moments of t and $t + \Delta t$:

$$\sigma_{\mathrm{b}} \mathbf{T}_{\mathrm{b}} \frac{\mathrm{d}\mathbf{A}_{\mathbf{N}}^{t+\Delta t}}{\mathrm{d}t} = -\nu_{\mathrm{e}}^{t+\Delta t} \mathbf{S}^{t+\Delta t} \mathbf{A}_{\mathbf{N}}^{t+\Delta t} + \frac{\gamma N_{\mathrm{t}}}{N_{\mathrm{c}} \Delta_{\mathrm{cs}}} \mathbf{Q}_{\mathrm{s}} \mathbf{I}_{\mathrm{s}}^{t+\Delta t} + \frac{\sigma_{\mathrm{b}}}{L_{\mathrm{sl}}} \mathbf{Q}_{\mathrm{b}} \mathbf{V}_{\mathrm{b}}^{t+\Delta t} \tag{3-13}$$

$$\sigma_{\mathrm{b}} \mathbf{T}_{\mathrm{b}} \frac{\mathrm{d}\mathbf{A}_{\mathbf{N}}^{t}}{\mathrm{d}t} = -\nu_{\mathrm{e}}^{t} \mathbf{S}^{t} \mathbf{A}_{\mathbf{N}}^{t} + \frac{\gamma N_{\mathrm{t}}}{N_{\mathrm{c}} \Delta_{\mathrm{cs}}} \mathbf{Q}_{\mathrm{s}} \mathbf{I}_{\mathrm{s}}^{t} + \frac{\sigma_{\mathrm{b}}}{L_{\mathrm{sl}}} \mathbf{Q}_{\mathrm{b}} \mathbf{V}_{\mathrm{b}}^{t} \tag{3-14}$$

Substituting (3-13) and (3-14) into (3-12) and rearranging the terms to isolate the unknown $t + \Delta t$ variables, one may obtain

$$\begin{aligned} &\left(\nu_{\mathrm{e}}^{t+\Delta t} \mathbf{S}^{t+\Delta t} + \frac{2\sigma_{\mathrm{b}} \mathbf{T}_{\mathrm{b}}}{\Delta t} \right) \mathbf{A}_{\mathbf{N}}^{t+\Delta t} - \frac{\gamma N_{\mathrm{t}}}{N_{\mathrm{c}} \Delta_{\mathrm{cs}}} \mathbf{Q}_{\mathrm{s}} \mathbf{I}_{\mathrm{s}}^{t+\Delta t} - \frac{\sigma_{\mathrm{b}}}{L_{\mathrm{sl}}} \mathbf{Q}_{\mathrm{b}} \mathbf{V}_{\mathrm{b}}^{t+\Delta t} = \\ &\qquad \left(-\nu_{\mathrm{e}}^{t} \mathbf{S}^{t} + \frac{2\sigma_{\mathrm{b}} \mathbf{T}_{\mathrm{b}}}{\Delta t} \right) \mathbf{A}_{\mathbf{N}}^{t} + \frac{\gamma N_{\mathrm{t}}}{N_{\mathrm{c}} \Delta_{\mathrm{cs}}} \mathbf{Q}_{\mathrm{s}} \mathbf{I}_{\mathrm{s}}^{t} + \frac{\sigma_{\mathrm{b}}}{L_{\mathrm{sl}}} \mathbf{Q}_{\mathrm{b}} \mathbf{V}_{\mathrm{b}}^{t} \end{aligned} \tag{3-15}$$

Applying the similar derivations to (3-10), (3-11) and (3-8) one may obtain the time-discretized form of those equations:

$$-\frac{2\gamma N_{\mathrm{s}} L_{\mathrm{sl}}}{N_{\mathrm{c}}\Delta_{\mathrm{cs}}}\mathbf{Q}_{\mathrm{s}}^{\mathrm{T}}\mathbf{A}_{\mathbf{N}}^{t+\Delta t}-\left(R_{\mathrm{s}}\Delta t+2L_{\mathrm{ew}}\right)\mathbf{I}_{\mathrm{s}}^{t+\Delta t}= \\ -\frac{2\gamma N_{\mathrm{s}} L_{\mathrm{sl}}}{N_{\mathrm{c}}\Delta_{\mathrm{cs}}}\mathbf{Q}_{\mathrm{s}}^{\mathrm{T}}\mathbf{A}_{\mathbf{N}}^{t}+\left(R_{\mathrm{s}}\Delta t-2L_{\mathrm{ew}}\right)\mathbf{I}_{\mathrm{s}}^{t}-\Delta t\left(\mathbf{V}_{\mathrm{s}}^{t+\Delta t}+\mathbf{V}_{\mathrm{s}}^{t}\right) \qquad (3\text{-}16)$$

$$-\frac{2L_{\mathrm{sl}}}{\Delta_{\mathrm{b}}}\mathbf{Q}_{\mathrm{b}}^{\mathrm{T}}\mathbf{A}_{\mathrm{N}}^{t+\Delta t}+\Delta t\mathbf{V}_{\mathrm{b}}^{t+\Delta t}+\frac{R_{\mathrm{b}}\Delta t}{N_{\mathrm{sl}}}\mathbf{M}\mathbf{I}_{\mathrm{r}}^{t+\Delta t}=-\frac{2L_{\mathrm{sl}}}{\Delta_{\mathrm{b}}}\mathbf{Q}_{\mathrm{b}}^{\mathrm{T}}\mathbf{A}_{\mathrm{N}}^{t}-\Delta t\mathbf{V}_{\mathrm{b}}^{t}-\frac{R_{\mathrm{b}}\Delta t}{N_{\mathrm{sl}}}\mathbf{M}\mathbf{I}_{\mathrm{r}}^{t} \qquad (3\text{-}17)$$

$$\Delta t\mathbf{M}^{\mathrm{T}}\mathbf{V}_{\mathrm{b}}^{t+\Delta t}-\left(\mathbf{R}_{\mathrm{r}}\Delta t+2\mathbf{L}_{\mathrm{r}}\right)\mathbf{I}_{\mathrm{r}}^{t+\Delta t}=-\Delta t\mathbf{M}^{\mathrm{T}}\mathbf{V}_{\mathrm{b}}^{t}+\left(\mathbf{R}_{\mathrm{r}}\Delta t-2\mathbf{L}_{\mathrm{r}}\right)\mathbf{I}_{\mathrm{r}}^{t} \qquad (3\text{-}18)$$

In the time-discretized system equations, (3-15) to (3-18), the values of *t*-variables are known from the solution to those equations at the last time step. To find the time-stepped solution one needs to iteratively substitute the present values of time-dependent variables for the corresponding *t* variables in the system equations and solve those equations with respect to the *t* + Δ*t* variables.

3.4 An efficient solution based on Newton-Raphson technique and domain decomposition

3.4.1 Newtion-Raphson system equation

As known from Section 2.4.4, the implementation of DD significantly improves the computation efficiency in solving the TLM-linearized system equations. This suggests that it is potentially more efficient to utilize DD to solve the system equations linearized by N-R method as it is quadratically convergent. The N-R iterative form of (3-15) to (3-18) is written as

$$\left(\mathbf{G}_{k}+\frac{2\sigma_{\mathrm{b}}\mathbf{T}_{\mathrm{b}}}{\Delta t}\right)\Delta\mathbf{A}_{\mathbf{N}\,k+1}^{t+\Delta t}-\frac{\gamma N_{\mathrm{t}}}{N_{\mathrm{c}}\Delta_{\mathrm{cs}}}\mathbf{Q}_{\mathrm{s}}\Delta\mathbf{I}_{\mathrm{s}\,k+1}^{t+\Delta t}-\frac{\sigma_{\mathrm{b}}}{L_{\mathrm{sl}}}\mathbf{Q}_{\mathrm{b}}\Delta\mathbf{V}_{\mathrm{b}\,k+1}^{t+\Delta t}= \\ -\left(\nu_{\mathrm{e}\,k}^{t+\Delta t}\mathbf{S}^{t+\Delta t}+\frac{2\sigma_{\mathrm{b}}\mathbf{T}_{\mathrm{b}}}{\Delta t}\right)\mathbf{A}_{\mathbf{N}\,k}^{t+\Delta t}+\left(-\nu_{\mathrm{e}}^{t}\mathbf{S}^{t}+\frac{2\sigma_{\mathrm{b}}\mathbf{T}_{\mathrm{b}}}{\Delta t}\right)\mathbf{A}_{\mathbf{N}}^{t} \\ +\frac{\gamma N_{\mathrm{t}}}{N_{\mathrm{c}}\Delta_{\mathrm{cs}}}\mathbf{Q}_{\mathrm{s}}\left(\mathbf{I}_{\mathrm{s}\,k}^{t+\Delta t}+\mathbf{I}_{\mathrm{s}}^{t}\right)+\frac{\sigma_{\mathrm{b}}}{L_{\mathrm{sl}}}\mathbf{Q}_{\mathrm{b}}\left(\mathbf{V}_{\mathrm{b}\,k}^{t+\Delta t}+\mathbf{V}_{\mathrm{b}}^{t}\right) \qquad (3\text{-}19)$$

$$-\frac{2\gamma N_{\mathrm{s}} L_{\mathrm{sl}}}{N_{\mathrm{c}}\Delta_{\mathrm{cs}}}\mathbf{Q}_{\mathrm{s}}^{\mathrm{T}}\Delta\mathbf{A}_{\mathbf{N}\,k+1}^{t+\Delta t}-\left(R_{\mathrm{s}}\Delta t+2L_{\mathrm{ew}}\right)\Delta\mathbf{I}_{\mathrm{s}\,k+1}^{t+\Delta t}=\frac{2\gamma N_{\mathrm{s}} L_{\mathrm{sl}}}{N_{\mathrm{c}}\Delta_{\mathrm{cs}}}\mathbf{Q}_{\mathrm{s}}^{\mathrm{T}}\left(\mathbf{A}_{\mathbf{N}\,k}^{t+\Delta t}-\mathbf{A}_{\mathbf{N}}^{t}\right)$$

$$+\left(R_{\mathrm{s}}\Delta t+2L_{\mathrm{ew}}\right)\mathbf{I}_{\mathrm{s}\,k}^{t+\Delta t}+\left(R_{\mathrm{s}}\Delta t-2L_{\mathrm{ew}}\right)\mathbf{I}_{\mathrm{s}}^{t}-\Delta t\left(\mathbf{V}_{\mathrm{s}}^{t+\Delta t}+\mathbf{V}_{\mathrm{s}}^{t}\right) \tag{3-20}$$

$$\begin{aligned}-\frac{2L_{\mathrm{sl}}}{\Delta_{\mathrm{b}}}\mathbf{Q}_{\mathrm{b}}^{\mathrm{T}}\Delta\mathbf{A}_{\mathrm{N}\,k+1}^{t+\Delta t}+\Delta t\Delta\mathbf{V}_{\mathrm{b}\,k+1}^{t+\Delta t}+\frac{R_{\mathrm{b}}\Delta t}{N_{\mathrm{sl}}}\mathbf{M}\Delta\mathbf{I}_{\mathrm{r}\,k+1}^{t+\Delta t}&=\\ \frac{2L_{\mathrm{sl}}}{\Delta_{\mathrm{b}}}\mathbf{Q}_{\mathrm{b}}^{\mathrm{T}}\left(\mathbf{A}_{\mathrm{N}\,k}^{t+\Delta t}-\mathbf{A}_{\mathrm{N}}^{t}\right)-\Delta t\left(\mathbf{V}_{\mathrm{b}\,k}^{t+\Delta t}+\mathbf{V}_{\mathrm{b}}^{t}\right)-\frac{R_{\mathrm{b}}\Delta t}{N_{\mathrm{sl}}}\mathbf{M}\left(\mathbf{I}_{\mathrm{r}\,k}^{t+\Delta t}+\mathbf{I}_{\mathrm{r}}^{t}\right)&\end{aligned} \tag{3-21}$$

$$\begin{aligned}\Delta t\mathbf{M}^{\mathrm{T}}\Delta\mathbf{V}_{\mathrm{b}\,k+1}^{t+\Delta t}-\left(\mathbf{R}_{\mathrm{r}}\Delta t+2\mathbf{L}_{\mathrm{r}}\right)\Delta\mathbf{I}_{\mathrm{r}\,k+1}^{t+\Delta t}&=-\Delta t\mathbf{M}^{\mathrm{T}}\left(\mathbf{V}_{\mathrm{b}\,k}^{t+\Delta t}+\mathbf{V}_{\mathrm{b}}^{t}\right)\\ &+\left(\mathbf{R}_{\mathrm{r}}\Delta t+2\mathbf{L}_{\mathrm{r}}\right)\mathbf{I}_{\mathrm{r}\,k}^{t+\Delta t}+\left(\mathbf{R}_{\mathrm{r}}\Delta t-2\mathbf{L}_{\mathrm{r}}\right)\mathbf{I}_{\mathrm{r}}^{t}\end{aligned} \tag{3-22}$$

where

$$\Delta\mathbf{A}_{\mathbf{N}\,k+1}^{t+\Delta t}=\mathbf{A}_{\mathbf{N}\,k+1}^{t+\Delta t}-\mathbf{A}_{\mathbf{N}\,k}^{t+\Delta t}$$

$$\Delta\mathbf{I}_{\mathrm{s}\,k+1}^{t+\Delta t}=\mathbf{I}_{\mathrm{s}\,k+1}^{t+\Delta t}-\mathbf{I}_{\mathrm{s}\,k}^{t+\Delta t}$$

$$\Delta\mathbf{V}_{\mathrm{b}\,k+1}^{t+\Delta t}=\mathbf{V}_{\mathrm{b}\,k+1}^{t+\Delta t}-\mathbf{V}_{\mathrm{b}\,k}^{t+\Delta t}$$

$$\Delta\mathbf{I}_{\mathrm{r}\,k+1}^{t+\Delta t}=\mathbf{I}_{\mathrm{r}\,k+1}^{t+\Delta t}-\mathbf{I}_{\mathrm{r}\,k}^{t+\Delta t}$$

$$\mathbf{G}_k=\nu_{\mathrm{e}\,k}^{t+\Delta t}\mathbf{S}^{t+\Delta t}+\frac{2}{\Delta_{\mathrm{e}}}\frac{\partial\nu_{\mathrm{e}\,k}^{t+\Delta t}}{\partial B_{\mathrm{e}}^{2}}\left(\mathbf{S}^{t+\Delta t}\mathbf{A}_{\mathrm{N}\,k}^{t+\Delta t}\right)\left(\mathbf{S}^{t+\Delta t}\mathbf{A}_{\mathrm{N}\,k}^{t+\Delta t}\right)^{\mathrm{T}} \tag{3-23}$$

In (3-23) Δ_{e} and B_{e} are the area and the flux density of corresponding element, respectively. In the process of solving (3-19) to (3-22), the values of $\nu_{\mathrm{e}\,k}^{t+\Delta t}$ and $\dfrac{\partial\nu_{\mathrm{e}\,k}^{t+\Delta t}}{\partial B_{\mathrm{e}}^{2}}$ are obtained by spline interpolation.

Unlike the constant coefficient matrix in TLM system equation, the coefficient matrix in the N-R system equation contains an iterative term, $\mathbf{G}_k$, which embodies the field nonlinearity in an electric machine. As the electromagnetic field in an electric machine may display a circumferential periodicity, it is not necessary for this case to mesh the whole machine's cross section when constructing the N-R system equation. The finite element mesh and the N-R system equation may be required for only a sector of one pole or one pole pair according to the field periodicity that depends on the number of slots and the number of poles in the machine. In the case that the field periodicity does not exist, it is required to construct the finite element mesh and the N-R system equation for the whole cross section.

For the purpose of calculation convenience the system equations (3-19) to (3-22) are usually transformed to obtain a symmetric coefficient matrix with positive diagonal entries. It is well known that an equation with such a coefficient matrix can be solved by Cholesky decomposition that reduces the computation overhead for Gaussian elimination. The symmetry of such a matrix can be obtained by applying three multipliers to both sides of (3-20) to (3-22), respectively. The negative coefficients of $\Delta\mathbf{I}_{\mathrm{s}\,k+1}^{t+\Delta t}$ and $\Delta\mathbf{I}_{\mathrm{r}\,k+1}^{t+\Delta t}$ in (3-20) and (3-22), i.e. – $(R_{\mathrm{s}}\Delta t + 2L_{\mathrm{ew}})$ and – $(R_{\mathrm{r}}\Delta t + 2L_{\mathrm{r}})$ that correspond to the negative diagonal entries in the coefficient matrix, are modified to be positive. Meanwhile dummy unknown variables corresponding to $\Delta\mathbf{I}_{\mathrm{s}\,k+1}^{t+\Delta t}$ and $\Delta\mathbf{I}_{\mathrm{r}\,k+1}^{t+\Delta t}$ are introduced into (3-20) and (3-22), respectively; and redundant equations with respect to these original and dummy variables are constructed in order to equate the total number of equations with the total number of unknown variables and negate the sign change of $\Delta\mathbf{I}_{\mathrm{s}\,k+1}^{t+\Delta t}$ and $\Delta\mathbf{I}_{\mathrm{r}\,k+1}^{t+\Delta t}$ terms on the left-hand side of the relevant subequations. With these transformations the N-R system equation can be rewritten into a submatrix form. A 3-slice example of this submatrix equation is shown as follows:

$$\begin{bmatrix} \mathbf{S}_{\mathrm{s1}k} & 0 & 0 & \mathbf{S}_{\mathrm{s1c}} \\ 0 & \mathbf{S}_{\mathrm{s2}k} & 0 & \mathbf{S}_{\mathrm{s2c}} \\ 0 & 0 & \mathbf{S}_{\mathrm{s3}k} & \mathbf{S}_{\mathrm{s3c}} \\ \mathbf{S}_{\mathrm{s1c}}^{\mathrm{T}} & \mathbf{S}_{\mathrm{s2c}}^{\mathrm{T}} & \mathbf{S}_{\mathrm{s3c}}^{\mathrm{T}} & \mathbf{S}_{\mathrm{c}} \end{bmatrix} \begin{bmatrix} \Delta\mathbf{A}_{\mathrm{s1},k+1} \\ \Delta\mathbf{A}_{\mathrm{s2},k+1} \\ \Delta\mathbf{A}_{\mathrm{s3},k+1} \\ \Delta\mathbf{C}_{k+1} \end{bmatrix} = \begin{bmatrix} \mathbf{F}_{\mathrm{s1}k} \\ \mathbf{F}_{\mathrm{s2}k} \\ \mathbf{F}_{\mathrm{s3}k} \\ \mathbf{F}_{\mathrm{c}k} \end{bmatrix} \tag{3-24}$$

In (3-24) $\mathbf{A}_{\mathrm{s1}}$, $\mathbf{A}_{\mathrm{s2}}$ and $\mathbf{A}_{\mathrm{s3}}$ are vectors of the $t + \Delta t$ nodal magnetic potentials of Slice 1, Slice 2 and Slice 3, respectively; $\mathbf{C}$ is a vector comprised of all the $t + \Delta t$ circuit variables including N_{p} stator phase currents, N_{p} dummy stator phase currents, $N_{\mathrm{b}}N_{\mathrm{sl}}$ bar segment voltages, $N_{\mathrm{b}}N_{\mathrm{sl}}$ rotor loop currents and $N_{\mathrm{b}}N_{\mathrm{sl}}$ dummy rotor loop currents; the Jacobian matrix (i.e. the coefficient matrix on the left-hand side) and the forcing terms on the right-hand side are written in terms of submatrices. The subscripts s1, s2 and s3 denote the coefficients of magnetic potential variables or the terms in the field equation of Slice 1, Slice 2 and Slice 3, respectively. The subscript c denotes the coefficients of circuit variables or the terms in the circuit equation. The subscript k denotes the matrices or the vectors that are updated with the N-R iterations while those without the subscript k are independent of the nonlinear iterations and need to be recalculated only at the beginning of each time step.

3.4.2 Domain decomposition of Newton-Raphson system equation

As mentioned in Section 2.4.4 B, two levels of DD have been exploited with TLM method. Of those two levels of DD, the one based on the rotationally symmetric subdomains is not applicable to the system equation linearized by N-R technique as the field nonlinearity in those subdomains produces variable coefficient matrices on the left-hand side of the field equation. On the other hand, the second level of DD that is based on the multislice-related subdomains is applicable to a system equation linearized by either TLM technique or N-R technique. The idea of the multislice-level DD has been stated in Section 2.4.4 B. This section formulates the combination method of N-R iteration and multislice-level DD (NR-DD method).

The NR-DD method converts the direct solution of (3-24) into a process of solving a circuit equation and multislice field equations separately. The first step of NR-DD method is to construct and solve the following circuit equation:

$$\mathbf{S}_{\mathrm{dd}k}\Delta\mathbf{C}_{k+1}=\mathbf{F}_{\mathrm{dd}k} \tag{3-25}$$

(3-25) is isolated from (3-24) by eliminating the magnetic potential variables.

$$\mathbf{S}_{\mathrm{dd}k}=\mathbf{S}_{\mathrm{c}}-\mathbf{S}_{\mathrm{s1c}}^{\mathrm{T}}\mathbf{S}_{\mathrm{s1}k}^{-1}\mathbf{S}_{\mathrm{s1c}}-\mathbf{S}_{\mathrm{s2c}}^{\mathrm{T}}\mathbf{S}_{\mathrm{s2}k}^{-1}\mathbf{S}_{\mathrm{s2c}}-\mathbf{S}_{\mathrm{s3c}}^{\mathrm{T}}\mathbf{S}_{\mathrm{s3}k}^{-1}\mathbf{S}_{\mathrm{s3c}} \tag{3-26}$$

$$\mathbf{F}_{\mathrm{dd}k}=\mathbf{F}_{\mathrm{c}k}-\mathbf{S}_{\mathrm{s1c}}^{\mathrm{T}}\mathbf{S}_{\mathrm{s1}k}^{-1}\mathbf{F}_{\mathrm{s1}k}-\mathbf{S}_{\mathrm{s2c}}^{\mathrm{T}}\mathbf{S}_{\mathrm{s2}k}^{-1}\mathbf{F}_{\mathrm{s2}k}-\mathbf{S}_{\mathrm{s3c}}^{\mathrm{T}}\mathbf{S}_{\mathrm{s3}k}^{-1}\mathbf{F}_{\mathrm{s3}k} \tag{3-27}$$

For the calculations of $\mathbf{S}_{\mathrm{dd}k}$ and $\mathbf{F}_{\mathrm{dd}k}$ it is unwise to design an algorithm to calculate the inverse of $\mathbf{S}_{\mathrm{s1}k}$, $\mathbf{S}_{\mathrm{s2}k}$ and $\mathbf{S}_{\mathrm{s3}k}$ in (3-26) and (3-27) due to the complication of matrix inverse calculation. Noting that the three submatrices $\mathbf{S}_{\mathrm{s1}k}$, $\mathbf{S}_{\mathrm{s2}k}$ and $\mathbf{S}_{\mathrm{s3}k}$ are also symmetric with positive diagonal entries like the global coefficient matrix, one may treat the matrix multiplications, $\mathbf{S}_{\mathrm{s1}k}^{-1}\mathbf{S}_{\mathrm{s1c}}$, $\mathbf{S}_{\mathrm{s2}k}^{-1}\mathbf{S}_{\mathrm{s2c}}$, $\mathbf{S}_{\mathrm{s2}k}^{-1}\mathbf{S}_{\mathrm{s2c}}$ and $\mathbf{S}_{\mathrm{s1}k}^{-1}\mathbf{F}_{\mathrm{s1}k}$, $\mathbf{S}_{\mathrm{s2}k}^{-1}\mathbf{F}_{\mathrm{s2}k}$, $\mathbf{S}_{\mathrm{s3}k}^{-1}\mathbf{F}_{\mathrm{s3}k}$, as solving a series of linear equations, which possess the symmetric coefficient matrices with positive diagonal entries and thus can be solved by Cholesky decomposition. For example, $\mathbf{S}_{\mathrm{s1}k}^{-1}\mathbf{F}_{\mathrm{s1}k}$ can be found by solving the following equation with Cholesky decomposition

$$\mathbf{S}_{\mathrm{s1}k}\mathbf{X} = \mathbf{F}_{\mathrm{s1}k} \tag{3-28}$$

Similarly, $\mathbf{S}_{\mathrm{s1}k}^{-1}\mathbf{S}_{\mathrm{s1c}}$ can be calculated by solving the following equations with Cholesky decomposition:

$$\mathbf{S}_{\mathrm{s1}k}\mathbf{Y}_i = \mathbf{S}_{\mathrm{s1c}\,i} \quad (i = 1, 2, \ldots, N_{\mathrm{ele}}) \tag{3-29}$$

where $N_{\mathrm{ele}} = 2N_{\mathrm{p}}+3N_{\mathrm{b}}N_{\mathrm{sl}}$, is the total number of unknown electric variables, and the vectors $\mathbf{S}_{\mathrm{s1c}\,i}$ are the column vectors assembling $\mathbf{S}_{\mathrm{s1c}}$, i.e.,

$$\mathbf{S}_{\mathrm{s1c}} = [\mathbf{S}_{\mathrm{s1c}\,1}, \mathbf{S}_{\mathrm{s1c}\,2}, \cdots, \mathbf{S}_{\mathrm{s1c}\,N_{\mathrm{ele}}}] \tag{3-30}$$

The matrix $\mathbf{S}_{\mathrm{s1}k}^{-1}\mathbf{S}_{\mathrm{s1c}}$ can be obtained by assembling the column vectors $\mathbf{Y}_i$, i.e.,

$$\mathbf{S}_{\mathrm{s1}k}^{-1}\mathbf{S}_{\mathrm{s1c}} = [\mathbf{Y}_1, \mathbf{Y}_2, \cdots, \mathbf{Y}_{N_{\mathrm{ele}}}] \tag{3-31}$$

Thus $\mathbf{S}_{\mathrm{dd}k}$ and $\mathbf{F}_{\mathrm{dd}k}$ are eventually found through a range of matrix operations shown in (3-26) to (3-31), and the terms in (3-26) guarantee that $\mathbf{S}_{\mathrm{dd}k}$ is symmetric. However, if one needs to solve (3-25) by Choleksy decomposition, positive diagonal entries of $\mathbf{S}_{\mathrm{dd}k}$ are required but actually not guaranteed because $\mathbf{S}_{\mathrm{dd}k}$ is obtained by the subtraction operations from a matrix with positive diagonal entries, i.e. $\mathbf{S}_{\mathrm{c}}$. Trial simulations indicate that the negative diagonal entries of $\mathbf{S}_{\mathrm{dd}k}$, if present, are always the diagonal coefficients for $\Delta\mathbf{I}_{\mathrm{s}\,k+1}^{t+\Delta t}$. One can change the sign of the negative diagonal coefficients to positive, and in the meanwhile adjust the coefficients of the dummy variables for $\Delta\mathbf{I}_{\mathrm{s}\,k+1}^{t+\Delta t}$ in the relevant subequations to negate the change of sign on the left-hand side of those subequations.

The second step of NR-DD method is to substitute the solution of (3-25) into the first three subequations in (3-24), i.e. (3-32) to (3-34), to find the magnetic potentials.

$$\mathbf{S}_{\mathrm{s1}k}\Delta\mathbf{A}_{\mathrm{s1},k+1} = \mathbf{F}_{\mathrm{s1}k} - \mathbf{S}_{\mathrm{s1c}}\Delta\mathbf{C}_{k+1} \tag{3-32}$$

$$\mathbf{S}_{\mathrm{s2}k}\Delta\mathbf{A}_{\mathrm{s2},k+1} = \mathbf{F}_{\mathrm{s2}k} - \mathbf{S}_{\mathrm{s2c}}\Delta\mathbf{C}_{k+1} \tag{3-33}$$

$$\mathbf{S}_{\mathrm{s3}k}\Delta\mathbf{A}_{\mathrm{s3},k+1} = \mathbf{F}_{\mathrm{s3}k} - \mathbf{S}_{\mathrm{s3c}}\Delta\mathbf{C}_{k+1} \tag{3-34}$$

It is evident that (3-32) to (3-34) can also be solved by Cholesky decomposition for the magnetic potentials.

In summary, the multislice-level DD decouples the global equation (3-24) to isolate the circuit equation (3-25) and the field equation of each slice, (3-32) to (3-34). Each of these isolated equations has significantly less unknown variables than the global equation. It is demonstrated that solving these isolated equations saves significant computation overhead in comparison to directly solving the global equation, where all the unknown variables are coupled. The proposed solution shown in (3-25) to (3-34) takes full advantage of those symmetric and positive diagonal matrices that enable the extensive application of Cholesky decomposition in equation solving and matrix multiplication. The generalized application of Cholesky decomposition simplifies the algorithm and further increases its execution efficiency.

3.4.3 Parallel NR-DD method

Constructing and solving the equations (3-25) and (3-32) to (3-34) can be executed in series on a single processor or in parallel on multiple processors. The parallel NR-DD method is expected to bring a significant promotion of computational efficiency for multislice time-stepped electric machine analysis. Similar to the parallel TLM-DD method summarized in Section 2.4.4 C, the basic idea of parallel NR-DD method is also to deal with the independent multislice field equations and the field terms in the circuit equation in parallel with multiple processors. The two methods differ only in the numerical techniques they use to linearize the nonlinear system equations. In this section the progress of parallel NR-DD method is illustrated with a 3-slice example.

In the NR-DD equations, (3-25) to (3-27) and (3-32) to (3-34), the calculations with respect to the matrices and the vectors with the subscripts s1, s2 and s3 are independent of one another. This feature suggests that one can assign the calculation related to each slice to one processor in a multiprocessor system that implements these calculations simultaneously. For example, this parallelized NR-DD algorithm may independently carry out:

1. Construction and updating of the matrices and vectors related to each slice, i.e. $\mathbf{S}_{\mathrm{s}ik}$, $\mathbf{S}_{\mathrm{s}i\mathrm{c}}$ and $\mathbf{F}_{\mathrm{s}ik}$ (i = 1, 2, 3);
2. Calculation of each slice's contribution to both sides of (3-25), i.e. $\mathbf{S}_{sic}^{\mathrm{T}}\mathbf{S}_{sik}^{-1}\mathbf{S}_{sic}$ and $\mathbf{S}_{sic}^{\mathrm{T}}\mathbf{S}_{sik}^{-1}\mathbf{F}_{sik}$ (i = 1, 2, 3);
3. Calculation of the vectors on the right-hand side of (3-32) to (3-34), i.e. $\mathbf{F}_{sik} - \mathbf{S}_{sic}\Delta\mathbf{C}_{k+1}$ (i = 1, 2, 3);
4. Solving the field equation of each slice, (3-32) to (3-34).

Under the above rules of calculation the number of processors needed for the parallel processing equals the number of slices. Two other tasks are assigned to the master processor which undertakes the calculations related Slice 1. The first is to construct $\mathbf{S}_{\mathrm{c}}$ and $\mathbf{F}_{\mathrm{c}k}$, and calculate $\mathbf{S}_{\mathrm{dd}k}$ and $\mathbf{F}_{\mathrm{dd}k}$ in accordance with (3-26) and (3-27) after the calculation of slice-contributed terms in those two equations is completed on the corresponding processors; the second is to solve the circuit equation (3-25). Figure 3-2 shows the steps of parallel NR-DD algorithm.

The inter-processor communication overhead is a common concern for parallel processing techniques. Intensive exchange of information between processors may retard execution of simulation programs, especially in the case that the processors have no shared memory and rely on communication network for data exchange. For the proposed parallel NR-DD algorithm it should be emphasized that the data that the multiple processors need to exchange are only the circuit variables $\Delta\mathbf{C}_{k+1}$ and the slice-contributed matrices in (3-26) and (3-27). The slave processors are required to send their calculated results of $\mathbf{S}_{\mathrm{s}i\mathrm{c}}^{\mathrm{T}}\mathbf{S}_{sik}^{-1}\mathbf{S}_{\mathrm{s}i\mathrm{c}}$ and $\mathbf{S}_{\mathrm{s}i\mathrm{c}}^{\mathrm{T}}\mathbf{S}_{sik}^{-1}\mathbf{F}_{sik}$ (i = 2, 3) to the master processor, where those results are needed for the calculations of $\mathbf{S}_{\mathrm{dd}k}$ and $\mathbf{F}_{\mathrm{dd}k}$. Once the master processor finishes solving the circuit equation (3-25), the value of $\Delta\mathbf{C}_{k+1}$ is substituted into (3-32) to find $\Delta\mathbf{A}_{\mathrm{s}1,k+1}$; on the other hand, the master processor sends the results of $\Delta\mathbf{C}_{k+1}$ to the slave processors, where the value of $\Delta\mathbf{C}_{k+1}$ is substituted into (3-33) and (3-34) in order to find $\Delta\mathbf{A}_{\mathrm{s}2,k+1}$ and $\Delta\mathbf{A}_{\mathrm{s}3,k+1}$, respectively. It is noted that the data exchanged between the processors are only some N_{ele}-dimensional matrices and vectors rather than the large nodes-related matrices. As the matrix operations take a large

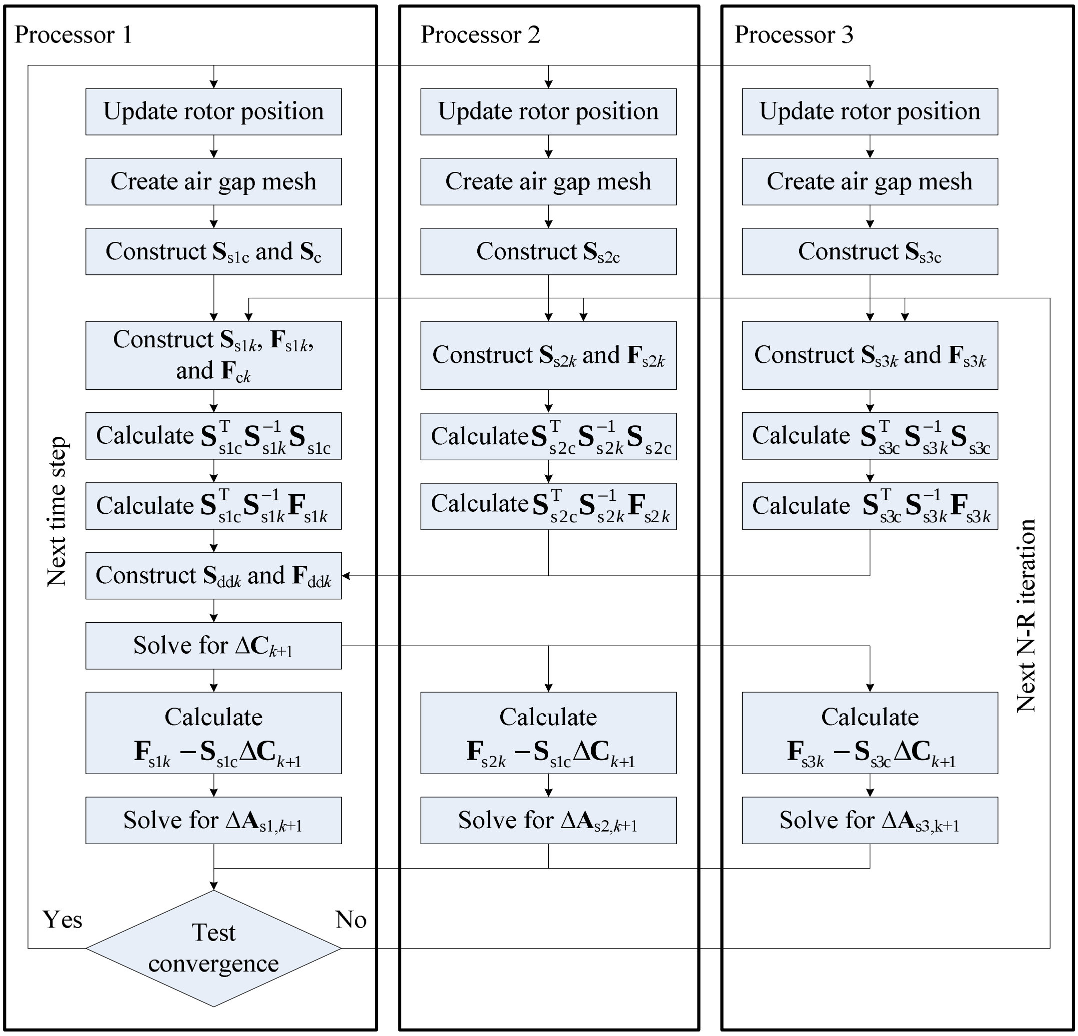

Figure 3-2 Flow chart of parallel NR-DD method (3-slice example)

proportion of the simulation time, the small amount of data exchange does not significantly slow down the simulations.

3.5 Simulation examples

3.5.1 Computational efficiency of NR-DD method

In order to test the efficiency of the numerical techniques developed in the previous sections, simulations are carried out for a 208V, 60Hz, 3-phase, Y-connected, 4-pole, 2hp skewed induction motor with a time-stepped multislice finite element model. The motor has 36 stator slots and 32 rotor slots with the rotor skew of one slot pitch, and the skew is modeled with 5 slices. The system equations are constructed and solved by traditional NR method, serial TLM-DD method, parallel TLM-DD method, serial NR-DD method and parallel NR-DD method, respectively, in order to compare their computational efficiencies. All these simulations are carried out at the rated voltage and speed for 10 supply cycles at 60Hz, with 100 time steps per cycle, i.e. 1000 steps of 166.7μs each.

As the number of stator slots per pole and the number of rotor bars per pole are both integrals (9 and 8, respectively), the electromagnetic field of this motor displays a circumferential periodicity of one pole pitch. A finite-element mesh of one pole pitch is thereby created for a set of simulations based on the traditional N-R, serial NR-DD and parallel NR-DD numerical techniques. This mesh, as shown in Figure 3-3, consists of 1941 nodes and 3534 first-order triangular elements for each slice (the number of dynamic air-gap elements is not included). Regarding the various simulations in this section it should be emphasized that the

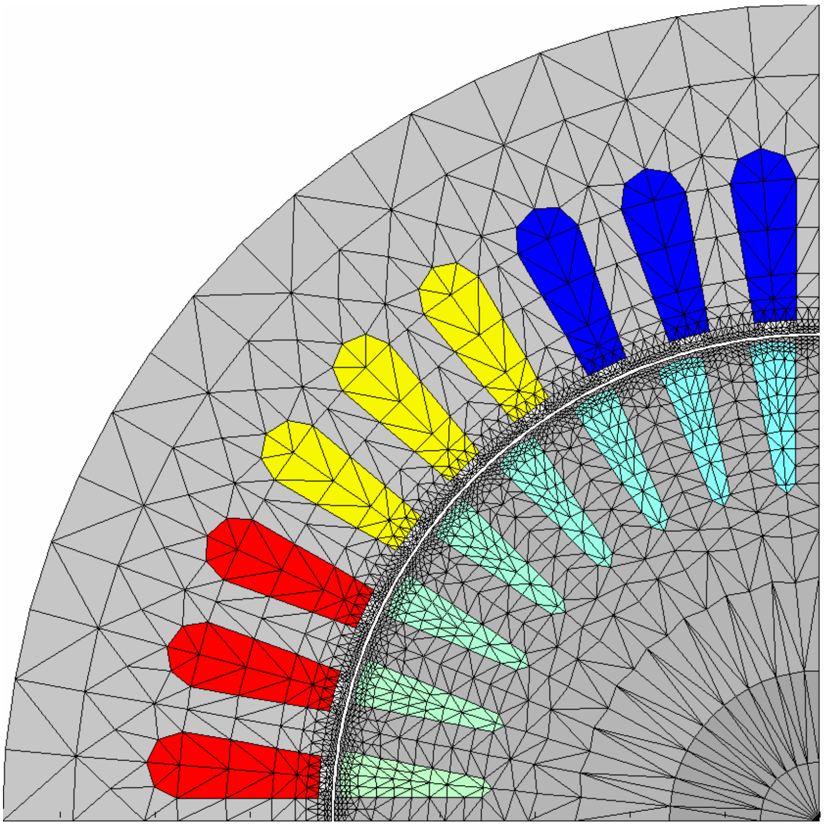

Figure 3-3 Finite element mesh of an induction motor

interbar circuit model is applied in the serial and parallel NR-DD simulations but not in the traditional N-R simulation, in other words, the interbar leakage currents are neglected in the traditional N-R simulation. For the case when interbar currents are neglected, the rotor circuit is modeled with the conventional approach that defines one loop current circulating in the path of every two adjacent bars and the end-ring segments across the bars, producing in total N_b variables of rotor loop current and N_b dummy variables of rotor loop current in the rotor circuit equation. Thus, in this section the system equation created by the traditional N-R technique contains $2N_b(N_{sl}-1)$ less circuit variables than the ones created by the serial and parallel NR-DD techniques.

The traditional NR and serial NR-DD simulations are executed respectively on a personal computer with a 3.2GHz dual-core PENTIUM D processor, while the parallel NR-DD simulation is executed on three of such computers connected by a local 1GB network. MPICH2, a high-performance and widely portable implementation of the Message Passing Interface (MPI) standard, is installed on those computers in order to develop and run the parallel simulation programs. Table 3-1 summarizes the elapsed time for the three simulations of the 10 supply cycles. Even though the NR-DD system equation has more unknown variables, the NR-DD methods are still obviously faster than the traditional N-R method. And particularly, the parallel NR-DD method is highly efficient, its simulation time is less than 1/5 of the time of traditional N-R simulation for a 5-slice model.

A previous author has carried out another set of simulations including the serial TLM-DD, the parallel TLM-DD, as well as the traditional NR simulation in order to investigate the computational efficiency of TLM-DD technique [41]. That set of simulations was implemented in the same manner as the last set of

Table 3-1
5-slice simulation times, 3.2 GHz PENTIUM D

	Traditional N-R method	Serial NR-DD method	Parallel NR-DD method
Interbar circuit model	Not included	Included	Included
Elapsed time	2270s	1581s	395s

simulations (the same motor under the same operating condition, the same MPI software and the same local network for communication) except that a cluster of relatively slow workstations with two 1GHz PENTIUM III processors each was used for that set of simulations. The interbar circuit model was not included in any of those simulations. As explained in Section 2.4.4 B, the regions of one stator slot, one rotor slot and the air gap from Figure 3-3 were chosen as the finite element mesh for the TLM-DD simulations. The simulations in [41] came with the elapsed time shown in Table 3-2.

Table 3-2
5-slice simulation times, 1GHz PENTIUM III

	Traditional N-R method	Serial TLM-DD method	Parallel TLM-DD method
Interbar circuit model	Not included	Not included	Not included
Elapsed time	9281s	7911s	2158s

Since the traditional NR simulation was made in both sets of tasks, the elapsed time of this simulation can be used as a benchmark to calculate the relative simulation times of other numerical methods for comparison of their computational efficiencies. The relative simulation times are shown in Table 3-3. The results indicate that serial and parallel NR-DD techniques are faster than serial and parallel TLM-DD techniques, respectively. And this improvement comes again even though the NR-DD techniques in this thesis include an interbar circuit model that produces more equations to solve than the TLM-DD techniques.

Table 3-3
Relative simulation times

Traditional N-R method	100.0%
Serial TLM-DD method	85.2%
Serial NR-DD method	69.6%
Parallel TLM-DD method	23.3%
Parallel NR-DD method	17.4%

3.5.2 Performance prediction

The simulations in this section aim to ensure the validity of the combination of multislice time-stepped FEM, interbar circuit model and parallel NR-DD technique in evaluating the general performances of an induction motor including current, input power, losses, output power, output torque, etc. To predict the above performances, a general evaluation of the four aspects of losses is required including stator Joule loss, rotor Joule loss (or cage loss), iron loss and friction and windage loss. Stray losses account for parts of those loss components, but are not investigated in this section as a specific target component. Figure 3-4 depicts the relation between those loss components and the finite element solution. In accordance with the second and third assumptions presented at the beginning of this chapter, in this finite element model there is not an equation that deals with eddy currents and hysteresis inside laminations and is solved simultaneously with the system equations (3-19) to (3-22). For this reason, the power flow in the finite element model includes only the components of stator Joule loss, rotor Joule loss, friction and windage loss, and output power, rather than iron loss. To evaluate the general performances of an induction motor, one needs to do the following steps:

1. Solve the system equation (3-19) to (3-22);
2. Calculate the input power to the finite element model using the supply voltage and the currents obtained from the last step, calculate the stator and rotor Joule losses as stated in Section 2.5.1 and Section 2.5.2, and then subtract the Joule losses and the friction and windage loss (obtained from

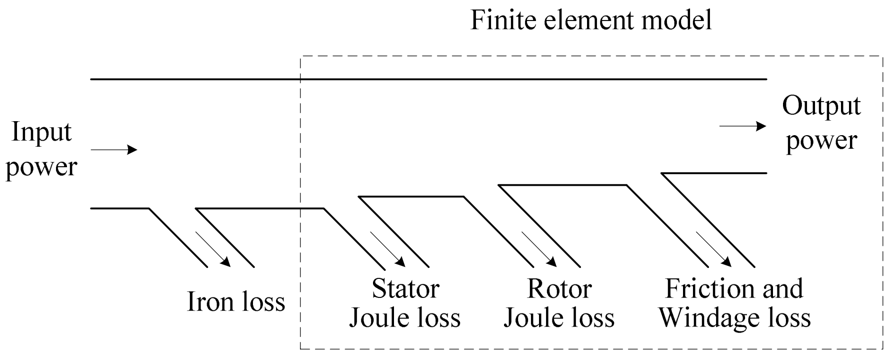

Figure 3-4 Power flow in an induction motor

experiment) from the input power to the finite element model to obtain the output power of the motor;

3. Evaluate the iron loss in compliance with the equations (2-3) to (2-6) outside the finite element model;
4. Add the iron loss into the input power to the finite element model to obtain the total input power to the motor, and correct the motor's current and power factor obtained from the first step in notice of the errors caused by the neglect of iron loss occurring in the finite element model.

The parallel NR-DD technique with an interbar circuit model is applied to this task. As the bar-iron contact resistance R_c (in Figure 2-5 (b)) is an influential factor to induction motor performances, it is important to estimate the value of R_c prior to a simulation. In [35] the authors propose an extensive experimental program in which the mean interbar resistance is determined for a large sample of cage rotors, and investigate the possible use of algorithms that may be used to estimate the interbar resistance of rotors having slots of a particular shape. The manufacturer of the induction motors investigated in [35] fabricated the same type of induction motor simulated in this section. As the value of R_c is a function of manufacturing procedures, the measurement results given by [35] are also considered valid for the motor simulated in this section. With the rotor circuit modeled as Figure 2-5 (b), the typical resistivity of R_c for this motor may range from 2.5×10^{-6} Ωm to 25×10^{-6} Ωm according to the estimation in [35], and the value of R_i is neglected. It should be noted that it is commonplace to describe interbar resistance in units of resistivity, a practice which may be somewhat confusing to those who are not familiar with the field. It is commonly known that the bar-iron resistance is physically a surface contact resistance, and as such may be thought of in terms of conductance per unit surface area. Since profile of the bar is uniform over the length of the machine, this in turn may be written as a conductance per unit length. As such the "interbar resistance" commonly referred to in papers is actually the interbar resistance between bars of unit length, and the units of resistivity are indicative of conductance per meter.

Rotor temperature is another sensitive factor to induction machine performances. In [69] the test measurement for this motor shows the stator temperature of 70˚C at rated operation. Rotor temperature is unknown and assumed approximately 15˚C - 35˚C higher than the stator temperature.

The simulation conditions of 10 supply cycles with 100 time steps per cycle in the last section are not suitable for an accurate prediction of the induction machine performance. A simulation of more supply cycles is required because the prediction of rotor losses needs the rotor currents and flux densities over a full slip cycle. Meanwhile a smaller time step is preferred in the attempt to reflect the effect of slot harmonics on rotor losses, i.e. the rotor harmonic stray losses. For these purposes, a period of 34 supply cycles with 400 time steps per cycle is simulated for this induction motor. As the initial electromagnetic state of the motor at the rated speed is unknown, transients will occur in the simulation and last for several cycles. Of the 34 simulated supply cycles, the first 9 cycles are reserved for the transients to settle down, and the last 25 cycles (the 4th to 34th) which cover approximately a full slip cycle at the rotor speed of 1726.5 rpm and the synchronous speed of 1800 rpm are used to evaluate the rotor losses. Simulations are made with the rotor temperature assumptions of 86˚C, 95˚C and 104˚C, and 10 different interbar resistances between 2.5×10^{-6} Ωm and 25×10^{-6} Ωm for each temperature. The calculated output power and cage losses are shown in Figure 3-5 and Figure 3-6 respectively, under these different conditions of rotor

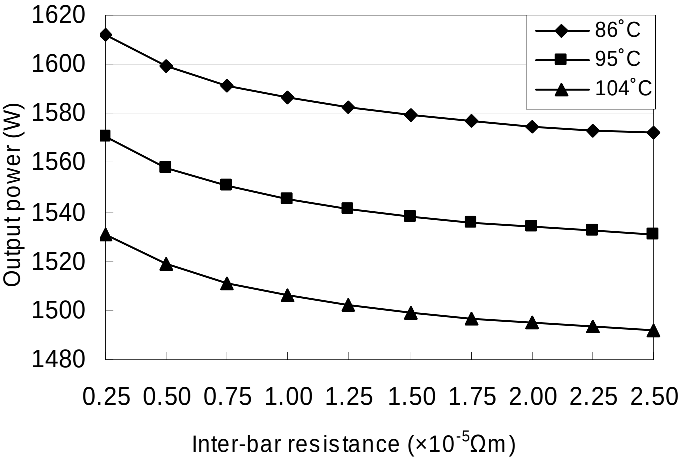

Figure 3-5 Evaluation of induction motor output power

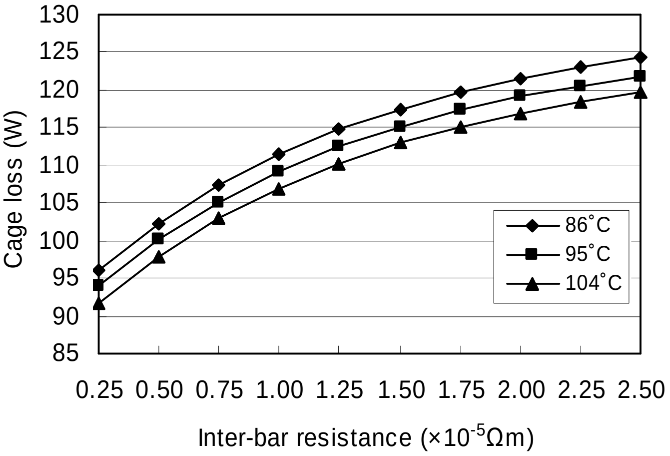

Figure 3-6 Evaluation of induction motor cage loss

temperatures and interbar resistances. Figure 3-5 shows that a ±9˚C variation of rotor temperature may result in a change of output power by ± 2% - 3%. By comparing the simulation results to the test results given by [69], the rotor temperature may be estimated to be in the range of 90˚C - 95˚C. This agrees with the expected range of rotor temperature, approximately 20˚C to 30˚C above the stator temperature. Figure 3-6 shows that the increasing interbar resistance in the simulated range leads to more cage loss. The simulated performances at the rotor temperature of 95˚C and the interbar resistance of 5.0×10^{-6} Ωm match the test results fundamentally, and they are tabulated in Table 3-4. Figure 3-7 shows the fluxes in the first and the fifth slice of the multislice model at the last time step of the simulation. Table 3-4 shows that there is a 40W difference between the input powers given by simulation and test, and simulated line current is somewhat smaller than the measured. A reason for these differences is that the finite element model does not explicitly include the iron loss. The posteriori evaluation of iron loss external to the finite element solution is not in complete accordance with the iron loss mechanism in reality. Relatively large discrepancies may be found between the simulated and measured power and current in the case of a larger ratio of iron loss to total loss.˚

3.6 Summary

This chapter validates a time-stepped finite element model for skewed induction machines that is based on multislice technique and interbar circuit

Table 3-4
Induction motor simulation and test results

	Simulation	Test [69]
Supply voltage (V)	208.45	208.45
Line current (A)	6.44	6.51
Input power (W)	1871.5	1831.5
Torque (Nm)	8.62	8.67
Speed (rpm)	1726.5	1726.5
Output power (W)	1558.0	1567.5
Efficiency (%)	83.2	85.6
Stator temperature (˚C)	70	70
Rotor temperature (˚C)	95	NA
Interbar resistance (Ωm)	5.0×10^{-6}	NA

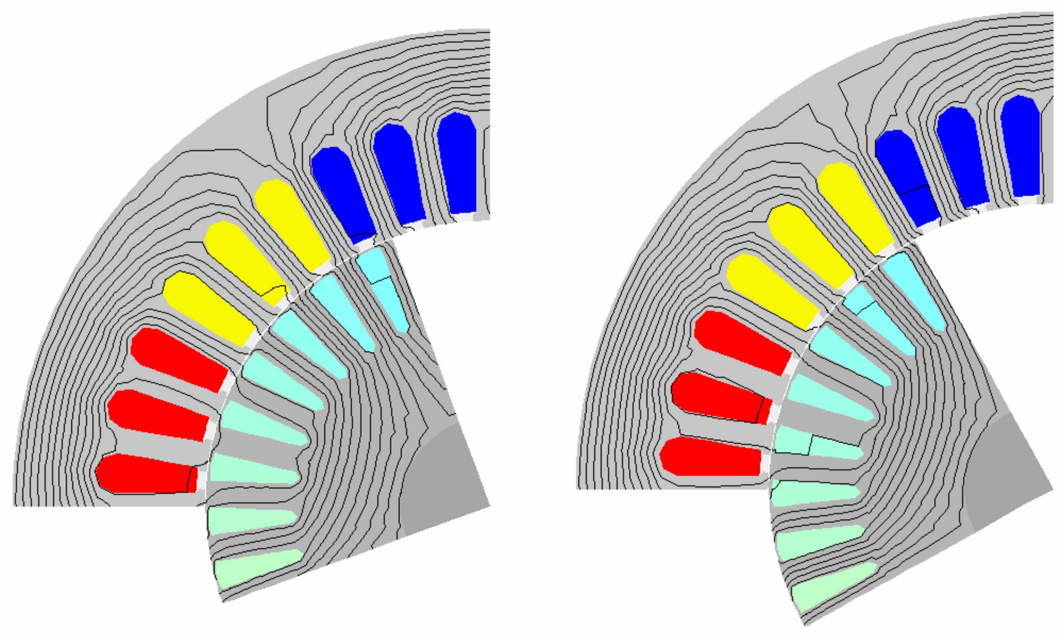
(a) Slice 1

(b) Slice 5

Figure 3-7 Fluxes in an induction motor

model. N-R method and DD are combined as a new technique to solve the system equation numerically. Incorporated with a more complicated rotor interbar circuit model, the new technique still brings a considerable promotion of computational efficiency in comparison to the several previously developed techniques, which are incorporated with the relatively simple and traditional rotor circuit model. The execution of NR-DD algorithm on a single processor reduces the simulation time by 30% in comparison to the standard solution based on traditional N-R algorithm. The parallel execution of a 5-slice NR-DD algorithm is shown to require less than 1/5 of the simulation time for the standard solution. The NR-DD algorithm is also shown to offer advantages of computational efficiency over the TLM-DD numerical technique in both serial and parallel executions.

The proposed method has been used to rapidly analyze a range of possible operating conditions. These results may be used by a manufacturer to provide a range of expected performance based on a stochastic analysis of “as made” characteristics.

Chapter 4 Induction Machine Analysis

4.1 Introduction

The simulation technique developed in Chapter 3 provides an accurate analysis tool for induction machines under a variety of operating conditions. Nowadays the use of induction machines with nonsinusoidal supplies is becoming increasingly common. Many of these machines are purpose-built inverter duty motors, yet the requirements for the design of an optimally efficient inverter duty motor are not fully understood. A significant amount of research has been done on the losses and properties of electrical steel sheets under nonsinusoidal supply conditions, e.g. [70] - [72]. Similarly, investigations into the losses in specific machines under nonsinusoidal supply have been carried out [73] - [77]. However, in the case of an inverter-fed machine, the impact of design choices on stray loss in the core, either what is traditionally defined as “iron loss” or through interbar currents, has not been fully described in the literature. Recent research has indicated that: the additional loss due to PWM frequency harmonics in standard steel samples is a function of the fundamental waveform shape [78]; additional stray loss density (compared to sinusoidal excitation) in transformer cores under PWM supply conditions is a function of the location within the lamination [71]. At higher flux densities, saturation effects may reduce the change in flux density caused by a high frequency current harmonic. Hence, it may be postulated that in a more saturated machine (with associated higher fundamental losses), the additional stray losses due to PWM switching may be less significant than in the case of a machine with a lower overall saturation level. Recent papers have also investigated the impact of interbar currents on slip frequency losses in skewed machines [7], [32], [34]. At these low frequencies, there is a complex relationship between interbar resistance and interbar loss as the current flow at low frequency is limited by both the resistance and reactances in the rotor circuit. However, at PWM frequencies, one may postulate that current harmonics will be limited by the reactance of the circuit, giving additional stray losses that are proportional to resistance.

Applying experimental investigations and FEA simulations based on the technique developed in Chapter 3, this thesis attempts to provide a better understanding of factors affecting stray loss and efficiency of induction machines excited with PWM supply. These factors include fundamental voltage waveform, load condition and PWM switching condition. The measurement and simulation results in this chapter may better inform future design of inverter-fed machines.

4.2 Experimental investigation

The experimental results in this chapter are provided by the collaborators at Politecnico di Torino, Turin, Italy. These collaborators possess a long-term experience of induction motor test and analysis. The test rig and the motor drive that are necessary for the experiments shown in chapter are accessible in their laboratory. This chapter attempts to use the simulation results shown in Section 4.3 to explain the observation obtained from the following experiments.

4.2.1 Experimental facility

The induction motor for the loss investigation in this chapter is the same as the one simulated for general performance prediction in Chapter 3. Motor nameplate data together with parameters derived from locked-rotor and no-load tests according to IEEE Stand 112 are presented in Table 4-1. Resistance and reactance values are the values corresponding to a stator temperature of 75˚C. The experimental facility is shown in Figure 4-1. With the power supply in the facility an excellent symmetric three-phase voltage without reverse components is available. The supply uses a 40kVA static sinusoidal supply with harmonic distortion of 0.1%. For nonsinusoidal conditions, the PWM inverter allows completely independent regulation of the modulation index and DC link voltage. The switching frequency can be selected in the range of 1kHz - 15kHz. In addition, the modulation waveform can be selected among sinusoidal, sinusoidal plus third harmonic and space vector. The electrical instrumentation used is based

Table 4-1
Induction motor parameters, referred to stator temperature of 75˚C

Rated voltage	208V
Rated output power	2.0HP (1492W)
Rated frequency	60Hz
Stator resistance	0.980Ω
Rotor resistance	1.033Ω
Stator leakage reactance	0.916Ω
Rotor leakage reactance	1.896Ω
Magnetizing reactance	31.933Ω
Equivalent core loss resistance	561.75Ω
Fiction and windage loss	30.1W

Figure 4-1 Induction motor test facility

on a digital power meter with a bandwidth of 800 kHz. In the load test, a torque transducer is connected between the motor under test and the load to measure both speed and torque.

4.2.2 Measured results

With the experimental facility shown in Figure 4-1 measurements are taken under no-load and load conditions for both sinusoidal and PWM supplies. The PWM supply used for these measurements is sinusoidal PWM (SPWM) with the PWM frequency of 5kHz. In order to closely match the simulations to the test conditions, tests are carried out first and simulations carried out with parameters as close as possible to actual test data.

A. No-load tests

No-load tests are carried out under the stator temperature of approximately 25˚C - 30˚C and a range of supply fundamental voltages with constant frequency, as IEEE Standard 112. The tests with PWM supplies are repeated under two different conditions:

1. Constant DC link voltage (V_{DC} = 354.03V), variable modulation index, m_a;
2. Constant modulation index ($m_a = 1$), variable DC link voltage.

Measured currents and loss components under the sinusoidal and PWM supply conditions are shown in Table 4-2. Of those loss components, the rotational losses (the sum of iron loss, stray loss due to harmonics in the squirrel cage and friction and windage loss) are presented in Figure 4-2 as a function of supply line-line voltage. Using the data from Table 4-2, it is possible to extrapolate by curve fitting to find the friction and windage loss. Using the data from the sinusoidal supply condition, a friction and windage loss value of 30.1W is found. Using a 5th order polynomial the rotational losses under sinusoidal excitation may be predicted for all magnitudes of supply voltage in the range of interest. Subtracting these predictions from the corresponding measured losses under PWM excitation, the additional rotational losses (relative to the sinusoidal case) can be found. These additional rotational losses are plotted in Figure 4-3. It can be seen that in the case of fixed modulation index and variable DC link voltage, the additional losses are approximately proportional to fundamental line-line voltage. In the case where the DC link voltage is constant, the additional losses follow a curve that is somewhat similar to the shape of a *B*-*H* curve in a saturating material.

B. Load tests

The motor is also tested under a range of load conditions up to 166% rated power, again with sinusoidal and SPWM supplies. The PWM supply tests are carried out with constant modulation index (m_a = 1.0) and constant DC link voltage.

Table 4-2
Measured results of an induction motor at no-load

Sinusoidal supply

Line-line voltage (V)	Line current (A)	Stator Joule loss (W)	Rotational loss (W)	Friction and windage loss (W)	Iron loss + Cage loss (W)
52.29	1.00	2.48	34.36	30.10	4.26
69.52	1.20	3.56	38.50	30.10	8.40
86.82	1.44	5.11	43.48	30.10	13.38
104.22	1.70	7.11	48.77	30.10	18.67
121.40	1.99	9.70	54.67	30.10	24.57
138.80	2.28	12.74	62.06	30.10	31.96
156.06	2.59	16.53	70.43	30.10	40.33
173.45	2.94	21.19	80.40	30.10	50.30
199.34	3.54	30.65	99.38	30.10	69.28
208.13	3.76	34.65	107.10	30.10	77.00
216.78	4.02	39.49	115.56	30.10	85.46
225.43	4.31	45.39	124.43	30.10	94.33

PWM supply, constant V_{dc} and variable m_a

Fundamental line-line voltage (V)	Line RMS current (A)	Stator Joule loss (W)	Rotational loss (W)	Friction and windage loss (W)	Iron loss + Cage loss (W)
39.95	0.92	2.11	35.63	33.33	2.30
49.55	0.99	2.43	38.49	33.33	5.16
59.64	1.09	2.99	41.77	33.33	8.44
79.76	1.36	4.65	50.18	33.33	16.85
99.97	1.66	6.88	59.61	33.33	26.28
120.30	1.99	9.91	69.18	33.33	35.85
140.72	2.36	13.92	79.12	33.33	45.79
159.21	2.69	18.06	88.15	33.33	54.82
179.11	3.06	23.34	98.92	33.33	65.59
189.53	3.39	28.58	107.54	33.33	74.21
201.34	3.66	33.41	116.87	33.33	83.54
210.47	3.89	37.69	125.17	33.33	91.84

Table 4-2 (continued)

PWM supply, variable V_{dc} and constant m_a

Fundamental Line-line voltage (V)	Line RMS current (A)	Stator Joule loss (W)	Rotational loss (W)	Friction and windage loss (W)	Iron loss + Cage loss (W)
40.57	0.93	2.16	32.32	29.07	3.25
49.89	1.00	2.49	34.35	29.07	5.28
60.37	1.13	3.16	37.69	29.07	8.62
70.51	1.26	3.95	41.41	29.07	12.34
90.01	1.55	5.95	48.54	29.07	19.47
110.04	1.85	8.45	56.55	29.07	27.48
131.24	2.24	12.39	67.88	29.07	38.81
161.53	2.86	20.05	88.17	29.07	59.10
181.04	3.27	26.18	103.88	29.07	74.81
199.93	3.63	32.24	117.19	29.07	88.12
209.90	3.90	37.16	126.91	29.07	97.84

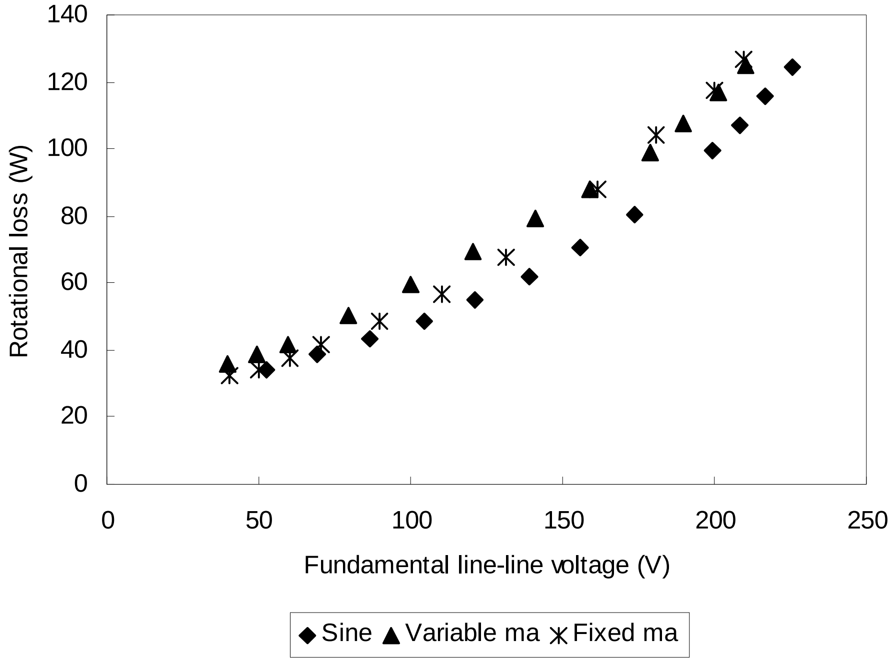

Figure 4-2 Measured rotational loss of an induction motor at no load

The data from these tests are tabulated in Table 4-3. In the sinusoidal supply case, the tabulated variables of voltage, current and power are RMS values, and the efficiency is given both in terms of direct input-output calculation and IEEE

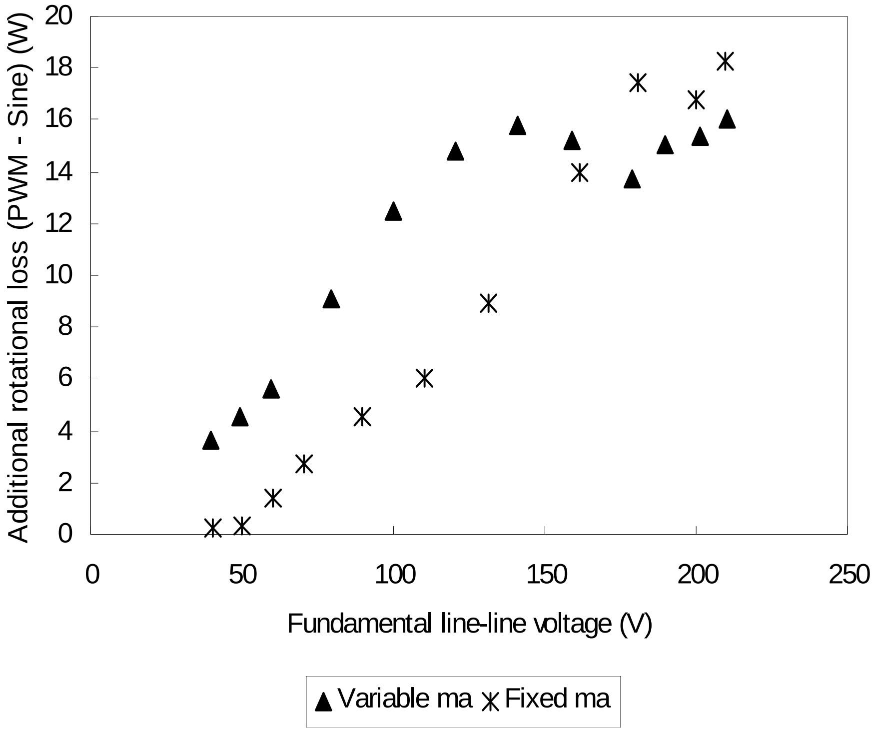

Figure 4-3 Measured additional rotational loss of an induction motor at no load

Standard 112. In the PWM case, both RMS and fundamental measurements are tabulated. Figure 4-4 plots the measured efficiency under both sinusoidal and PWM supply conditions. As may be expected, the sinusoidal efficiency is higher than the PWM case, with direct efficiency measurement higher than the value calculated according to the standard. Of particular interest in these results is the impact of PWM supply on available output torque and fundamental input power. Plotting the torque-speed curves in Figure 4-5, it can be seen that the gradient of the torque speed curve is less steep when PWM supply is used. The difference between the torques under PWM and sinusoidal supply conditions becomes more apparent as the load increases. Figure 4-6 plots the input power to the motor as a function of load; the input power under sinusoidal supply conditions is compared with fundamental and total input power under PWM conditions. The power curve under sinusoidal supply is found less steep than the total power curve and the fundamental power curve under PWM supply. The difference between sinusoidal supply power and PWM total power becomes pronounced as the load increases,

Table 4-3
Load test results of an induction motor

Sinusoidal supply

Load percentage (%)	5.6	26.4	46.9	77.7	103.5	127.6	138.3
Line-line voltage (V)	209.0	208.9	208.9	208.7	208.6	208.5	208.5
Line current (A)	3.67	3.92	4.40	5.44	6.52	7.59	8.16
Input power (W)	218.5	543.2	878.3	1392.3	1837.7	2262.5	2457.6
Output torque (Nm)	0.47	2.20	3.91	6.47	8.62	10.63	11.52
Speed (rpm)	1795.5	1783	1768	1746	1726	1705	1697
Efficiency (direct, %)	40.0	75.6	82.4	85.0	84.8	83.9	83.3
Efficiency (IEEE 112, %)	NA	71.3	79.8	83.3	83.5	82.8	82.3

PWM supply

Load percentage (%)	4.6	24.7	45.0	65.2	100.2	122.1	166.6
Line-line voltage (fundamental, V)	213.5	211.5	210.0	208.8	207.7	207.1	206.5
Line current (RMS, A)	3.892	4.058	4.476	5.094	6.543	7.636	10.028
Line current (fundamental, A)	3.853	4.019	4.435	5.058	6.481	7.555	9.918
Input power (total, W)	240.9	564.6	897.6	1238.9	1854.4	2258.3	3123.0
Input power (fundamental, W)	220.7	542.7	873.4	1214.5	1827.9	2234.5	3072.7
Output torque (Nm)	0.39	2.06	3.75	5.43	8.35	10.17	13.88
Speed (rpm)	1799	1785	1772	1756	1727	1706	1663
Efficiency (direct, %)	30.1	68.2	77.5	80.6	81.4	80.5	77.4

however the difference between PWM fundamental and total power that represents the input harmonic power, appears relatively less noticeable. Regarding the load tests it is important to underline that the torque measurement under PWM condition is not easy, especially at low load where the ripple may be so considerable relative to the low output torque that it may interfere with the torque meter reading. In addition the rotor temperature is not the same during the two load tests.

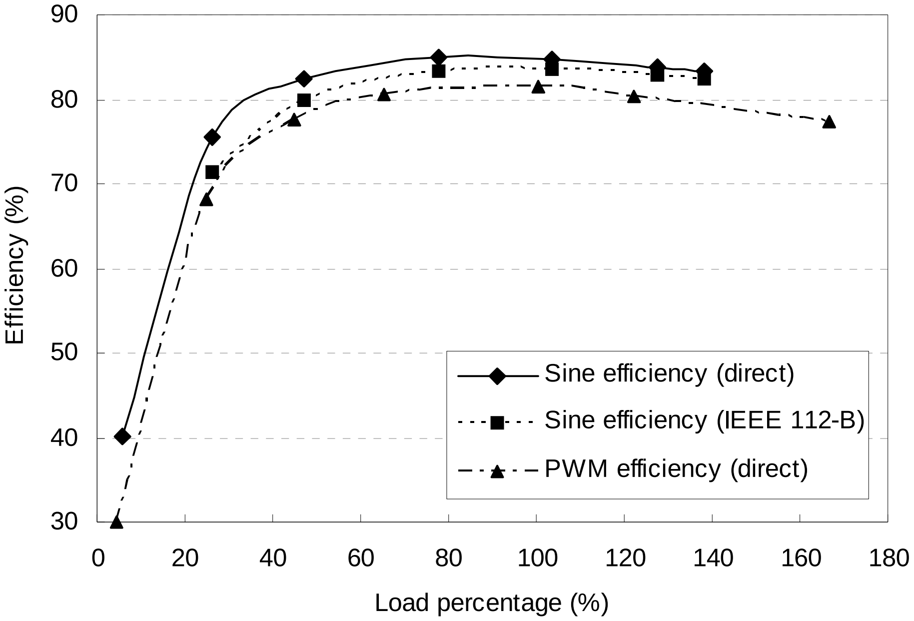

Figure 4-4 Measured efficiency of an induction motor

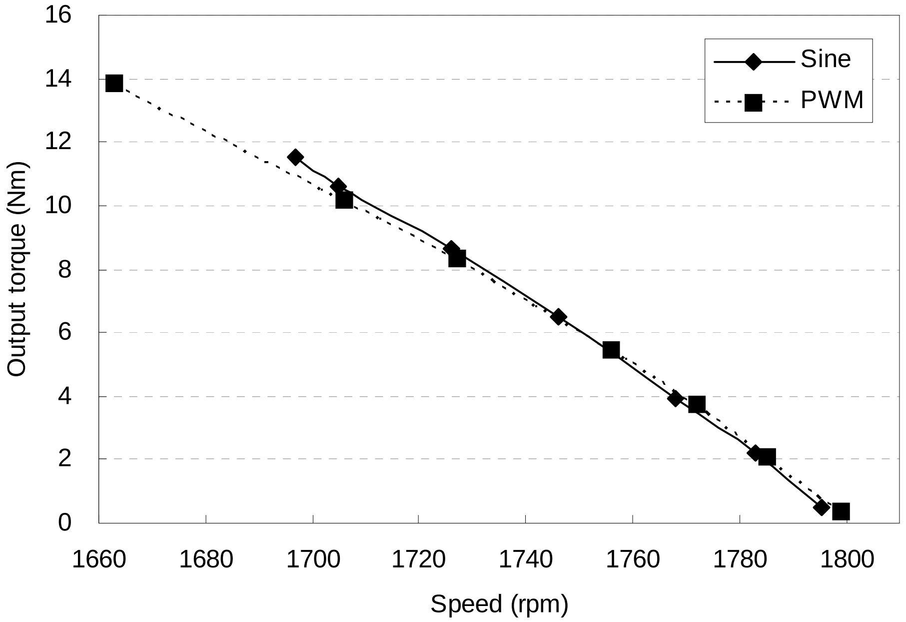

Figure 4-5 Measured torque-speed curves of an induction motor

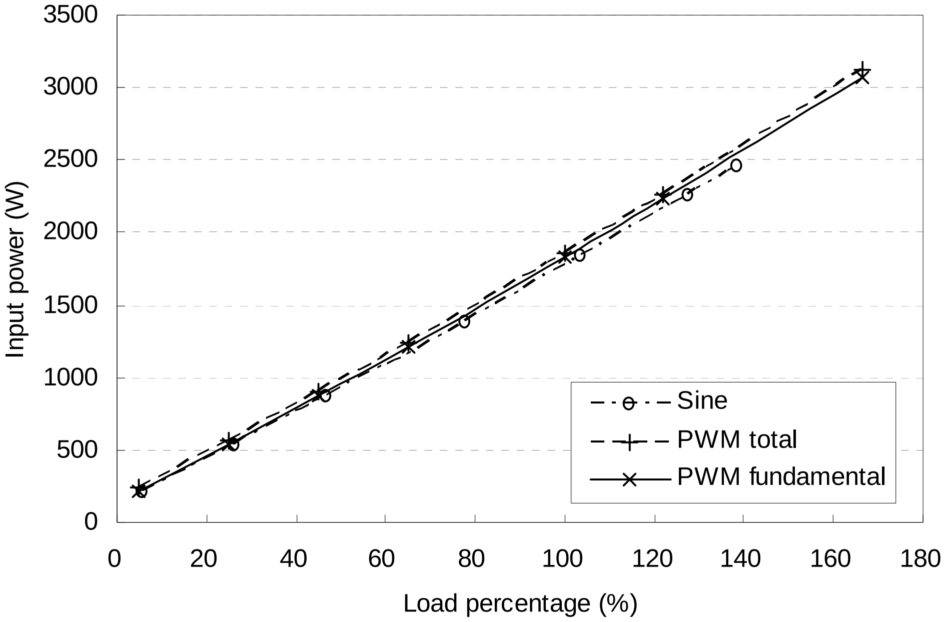

Figure 4-6 Measured input power to an induction motor

4.3 Finite element simulation

4.3.1 Simulation settings and parameters

As for the cases with measured results, time-stepped 5-slice finite element simulations are carried out for the load and no-load operations under sinusoidal and PWM supply conditions. Accurate prediction of stray loss is essential to loss evaluation under PWM supply condition. For this reason the interbar circuit model is incorporated in the finite element simulation to accurately predict the cage losses at slot harmonic frequencies. The finite element mesh in Figure 3-3 is used again for these simulations. The parameters in Table 4-4 are provided for prediction of machine losses.

The simulation algorithm deals with the time step setting in different manner for the cases of sinusoidal and PWM excitation. In the case of sinusoidal supply, 400 time steps per cycle are used, and each step has equal length. The number of time steps and hence the computational burden required for a simulation with PWM supply may be significantly increased as the PWM frequency can be as high as hundreds of times the frequency of sinusoidal supply. A standard 3-phase inverter has 6 switching instances per PWM cycle, and the intervals between adjacent switching instances are variable, resulting in variable time steps in the simulations. For an inverter with PWM frequency of 5kHz and reference signal frequency of 60Hz, there are 500 variable time steps per cycle of reference signal. The simulation algorithm searches for the switching instances by comparing the modulation waveform with the triangular switching waveform every 0.1μs, and sets up a new time step whenever the inverter switching state is found changed. The supply voltage is assumed to be an ideal PWM waveform, i.e. dead-time, rise-time and device voltage drop are all neglected and the input voltages to the machine are assumed to be constant within each time step. As a large number of simulations are required for different load and supply combinations and some of them involve long slip cycles under low load, parallel NR-DD technique is implemented to efficiently solve the system equation.

Table 4-4
Material parameters of an induction motor

Core length	0.113m	Bar-iron contact resistance	$5.0\times10^{-6}\Omega$m
Lamination thickness	0.5mm	Lamination mass density	7850kg/m^3
Lamination conductivity	5.556×10^{6} S/m	α	2.43
k_h	0.0199	k_e	9.98×10^{-5}
Stator resistance at 20.2˚C	0.806Ω	Rotor cage conductivity at 25.0˚C	2.91×10^{7}S/m
Temperature coefficient of stator resistance	3.9×10^{-3}/˚C	Temperature coefficient of rotor cage	3.9×10^{-3}/˚C

4.3.2 Simulation results

As will be discussed later, accurate stray loss prediction under no-load conditions is difficult. Load predictions are discussed first, followed by the no-load cases.

A. Load simulations

In accordance with the load test, the PWM conditions are simulated with an amplitude modulation index of 1.0. Due to the assumption of an ideal PWM waveform, the DC link voltage used for the simulations is lower than the actual value used in the test. These load simulations simulate a full slip cycle for the load conditions with slip above 0.0155. The lower load cases have rotor fundamental time period in excess of 100 times the supply fundamental time period, those simulations are therefore impractical and aborted.

Results of sinusoidal and PWM simulations of actual load conditions are presented in Table 4-5. At first glance, there is excellent agreement between the simulation and test measurements. There are some small discrepancies; the predicted line currents are approximately 1% - 5% smaller than the measurements; but the results are encouraging. One comment regarding the quality of the results should be reserved for the choice of temperature used in the simulations. Measured stator temperature under rated conditions was known at the time of the simulations and is used. However, the rotor temperature is unknown under the rated conditions and assumed to be approximately 30˚C above the stator, increasing slightly with the load. The same stator temperature is used for all sinusoidal simulations. In the PWM case, it is assumed that the rotor is hotter than in the sinusoidal case. This assumption is based in part on that the PWM excitation produces more rotor iron loss than the sinusoidal excitation.

The simulated torque-speed curve is plotted in Figure 4-7 according to the results in Table 4-5. The test and predicted efficiencies are plotted in Figure 4-8 for the sinusoidal supply case and Figure 4-9 for the PWM case. The simulated torque-speed curve displays the same tendency of gradient with the measured torque-speed curve in Figure 4-5. The result showing a difference in the torque-speed curves under sinusoidal and PWM supply indicates that a higher slip is required for a given output power and this phenomenon becomes more remarkable as the load increases. The higher slip suggests that additional input power at fundamental frequency will be required for a motor with PWM supply. It is well known that additional harmonic stray loss is produced as a PWM excitation replaces a sinusoidal excitation, however the measured and simulated results of higher slip requirement indicate that the majority of the total additional loss comes from the fundamental input power rather than the harmonic input

Table 4-5
Load simulation results of an induction motor

Sinusoidal supply

Load percentage (%)	46.9	77.7	103.5	127.6	138.3
Line-line voltage (V)	208.9	208.7	208.6	208.5	208.5
Line current (A)	4.33	5.36	6.43	7.51	7.96
Input power (W)	901.29	1411.6	1867.0	2293.6	2464.3
Output torque (Nm)	3.92	6.47	8.67	10.68	11.46
Speed (rpm)	1768	1746	1726	1705	1697
Rotor temperature (˚C)	100	104	104	110	110
Stator temperature (˚C)	70	70	70	70	70
Output power (W)	726.5	1183.1	1567.6	1906.4	2036.1
Efficiency (%)	80.6	83.8	83.96	83.12	82.63
Stator iron loss (W)	40.70	40.38	40.84	41.83	42.33
Rotor iron loss (W)	27.86	28.76	29.66	29.55	30.58
Total iron loss (W)	68.56	69.13	70.50	71.38	72.91
Stator Joule loss (W)	51.59	78.97	114.09	156.37	175.76
Cage loss (W)	25.11	51.19	86.00	130.91	151.09
Friction and windage loss (W)	29.58	29.21	28.88	28.53	28.39

PWM supply

Load percentage (%)	45.0	65.2	100.2	122.1	166.6
Line-line voltage (fundamental, V)	210.0	208.8	207.7	207.1	206.5
Line current (RMS, A)	4.32	4.91	6.30	7.27	9.49
Input power (total, W)	927.4	1251.2	1858.4	2247.1	3066.4
Output torque (Nm)	3.80	5.45	8.41	10.23	13.918
Speed (rpm)	1772	1756	1727	1706	1663
Rotor temperature (˚C)	112	122	122	130	130
Stator temperature (˚C)	69	72	72	77	77
Output power (W)	705.7	1001.9	1521.1	1827.6	2421.6
Efficiency (%)	76.10	80.08	81.85	81.33	78.97
Stator iron loss (W)	60.92	59.47	59.74	60.06	62.00
Rotor iron loss (W)	53.24	50.99	49.33	48.70	46.19
Total iron loss (W)	114.16	110.46	109.07	108.76	108.19
Stator Joule loss (W)	51.52	67.27	111.06	151.05	259.19
Cage loss (W)	27.35	43.19	89.33	132.06	250.54
Friction and windage loss (W)	28.63	28.37	27.91	27.57	26.87

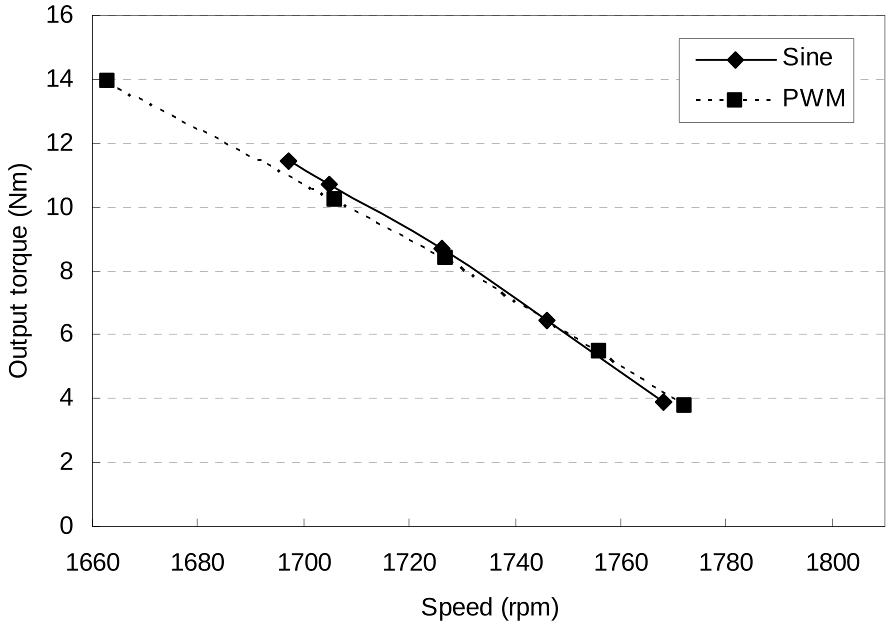

Figure 4-7 Simulated torque-speed curves of an induction motor

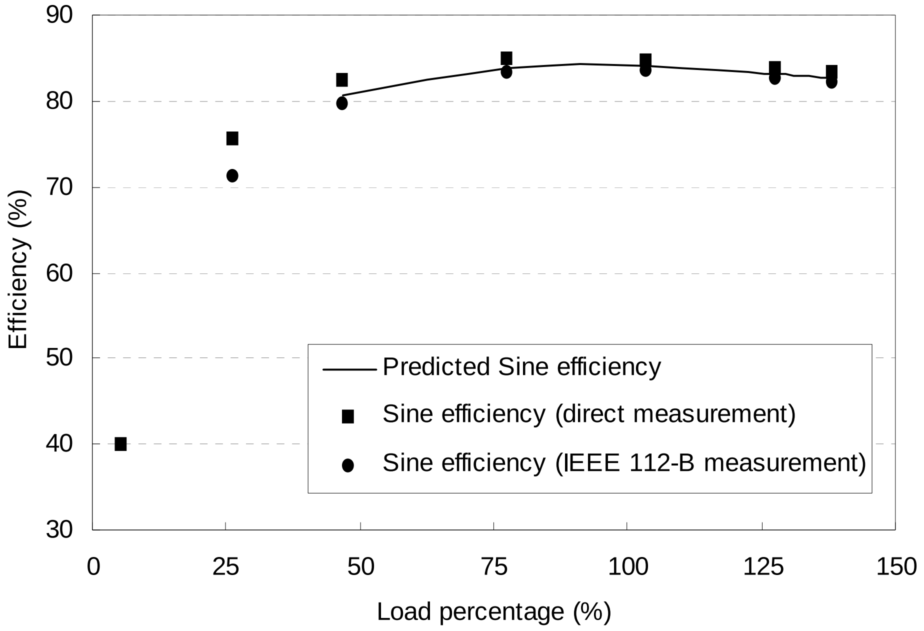

Figure 4-8 Comparison of predicted Sine efficiency with test

power that is consumed in a motor as harmonic stray loss. This conclusion is verified by the measured input power curves in Figure 4-6, where the curve of PWM fundamental input power is closer to the curve of total PWM input power than to the curve of sinusoidal input power, indicating an additional harmonic

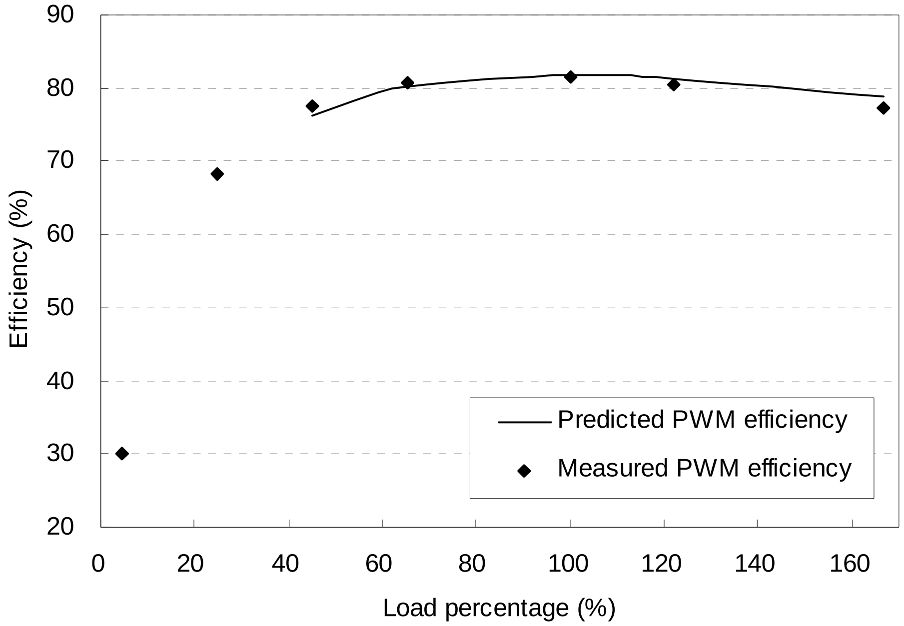

Figure 4-9 Comparison of predicted PWM efficiency with test

stray loss less than the additional fundamental loss. The cause of the additional fundamental frequency power losses may be due to higher rotor temperatures (due to the time harmonic losses introduced by the PWM supply and the consequent increase of the rotor resistance). In this case the slip required for a given torque will be higher. Alternatively, the torque at a given slip may be reduced due to increased saturation resulting in a lower available air-gap MMF.

B. No-load simulations

The accurate numerical prediction of no-load stray losses is difficult for a number of reasons. Typically, the time required for the simulation transient to pass and for steady state to be reached is significant as there is little damping in an unloaded motor system. In addition, the true no-load condition may result in a slip speed of as little as 1rpm, giving a slip cycle time period 1800 times the fundamental supply period. A number of attempts to overcome these difficulties are made in the work in this section, including simulation at synchronous speed which is a state close to no-load conditions.

The results of no-load simulation under sinusoidal and PWM supply conditions are presented in Table 4-6. Loss calculation at synchronous speed neglects the rotor hysteresis loss term (2-4) as the rotor laminations only traverse minor loops at synchronous speed. The predicted rotational losses at synchronous speed are plotted in Figure 4-10. It can be seen that the sinusoidal predictions match the test measurements well, but that the PWM predictions are excessive. Considering the sinusoidal simulations for a moment, the results match closely

Table 4-6
Simulation results of an induction motor at no load

Sinusoidal supply

Line-line voltage (V)	Stator Joule loss (W)	Rotational loss (W)	Friction and windage loss (W)	Iron loss (W)	Cage loss (W)
52.29	1.42	33.60	30.10	3.50	0.000
69.52	2.48	36.22	30.10	6.12	0.001
86.82	3.86	39.67	30.10	9.56	0.003
104.22	5.58	44.14	30.10	14.01	0.02
121.40	7.71	49.96	30.10	19.72	0.14
138.80	10.44	57.33	30.10	26.61	0.62
156.06	13.86	66.17	30.10	34.16	1.91
173.45	18.12	77.50	30.10	43.06	4.34
199.34	26.34	99.90	30.10	59.65	10.15
208.13	30.42	108.96	30.10	66.31	12.56
216.78	34.09	118.72	30.10	73.30	15.32
225.43	40.00	128.70	30.10	80.57	18.03

PWM supply, constant V_{dc} and variable m_a

Fundamental line-line voltage (V)	Stator Joule loss (W)	Rotational loss (W)	Friction and windage loss (W)	Iron loss (W)	Cage loss (W)
39.95	0.87	66.56	33.33	33.23	0.000
49.55	1.32	74.00	33.33	40.66	0.001
59.64	1.91	82.00	33.33	48.67	0.002
79.76	3.38	97.18	33.33	63.85	0.003
99.97	5.31	120.51	33.33	87.15	0.02
120.30	7.85	141.11	33.33	107.62	0.16
140.72	11.23	150.36	33.33	116.18	0.85
159.21	15.22	154.06	33.33	118.17	2.56
179.11	20.54	158.66	33.33	119.46	5.87
189.53	23.84	162.82	33.33	121.23	8.25
201.34	28.24	168.88	33.33	124.07	11.48
210.47	32.24	173.35	33.33	126.07	13.95

Table 4-6 (continued)

PWM supply, variable V_{dc} and constant m_a

Fundamental line-line voltage (V)	Stator Joule loss (W)	Rotational loss (W)	Friction and windage loss (W)	Iron loss (W)	Cage loss (W)
40.57	0.88	33.62	29.07	4.55	0.000
49.89	1.32	35.87	29.07	6.80	0.000
60.37	1.91	38.97	29.07	9.90	0.001
70.51	2.60	42.58	29.07	13.51	0.001
90.01	4.22	51.78	29.07	22.71	0.004
110.04	6.37	55.73	29.07	26.61	0.05
131.24	9.37	83.25	29.07	53.82	0.36
161.53	15.46	109.76	29.07	78.05	2.65
181.04	20.77	130.71	29.07	95.64	6.00
199.93	27.31	154.53	29.07	114.72	10.74
209.90	30.98	168.29	29.07	125.02	14.20

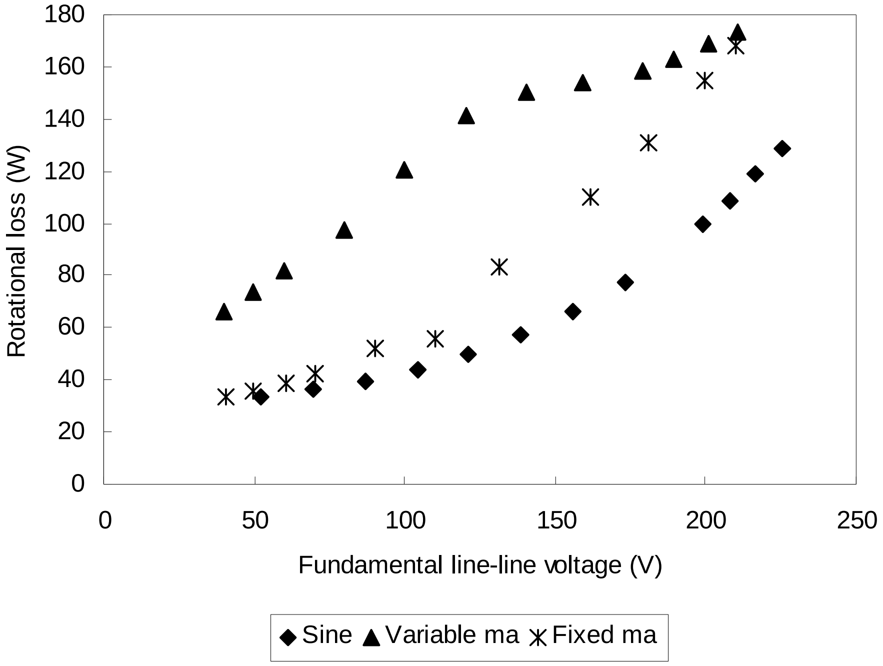

Figure 4-10 Predicted rotational loss of an induction motor at no load

with test (including the test value for friction and windage) and could be used to calculate the traditional iron loss parameter for the equivalent circuit model. Traditionally, it is assumed that the cage loss under synchronous conditions is zero, especially in the case where the rotor is skewed. The losses remaining after friction and windage and stator Joule loss are subtracted from the input power and assigned to be core losses in compliance with IEEE Standard 112. However, even though the machine is skewed, the interbar effect will result in some currents flowing at slot harmonic frequencies and hence stray cage loss. In the case shown, the stray cage loss component is predicted to be almost 20% of the iron loss component.

Turning to the discrepancy in predicted loss under PWM conditions, it is the author’s opinion that the discrepancy is due mainly to the discrete calculation of the rotor eddy-current losses. Most of the laminations in the unloaded motor are operating in the unsaturated region of the *B*-*H* curve, with the effect that small field intensity changes cause relatively large flux density changes (when compared to the effect when saturated). It is observed that the predicted losses under PWM conditions are heavily dependent on the error tolerance used in the numerical simulations. This is likely due to a combination of the rapid change in magnetic field at PWM frequencies and the requirement for discrete time differentiation of flux density in order to predict the losses. Under a PWM excitation certain variable time steps used to model narrow input voltage pulses can be several orders of magnitude smaller than the fixed time steps used to model sinusoidal supply. Thus the sudden change of the PWM voltage excitation may cause the numerical errors of flux density to be exaggerated when the flux density derivative is used in (2-3) and (2-6) for evaluation of eddy-current loss and excess loss. Consequently, the direct numerical calculation of the flux density derivative will cause the predicted eddy-current and excess losses to be excessive.

4.3.3 Improved rotor iron loss evaluation under low slip and PWM supply conditions

As mentioned in Section 4.3.2 B, there are two reasons for the difficulty in accurately predicting iron loss in a PWM-fed induction motor at a low slip (or no load):

1. The true no-load conditions result in a rotor fundamental frequency less than 0.1Hz, the simulation for such a long period of PWM-fed induction machine operation produces impractical computational burden;
2. The discrete-time calculation of no-load rotor iron loss under PWM supply conditions is sensitive to the accuracy of flux density prediction, even small noises in numerical simulation may cause eddy-current losses to be overpredicted.

Although the simulation at synchronous speed plus a time-domain iron loss calculation is expected to give a result close to the true value of rotor iron loss at no-load, in practice this approach still cannot overcome the simulation accuracy interference in eddy-current loss evaluation. In addition, the synchronous model fails to calculate rotor hysteresis loss because the fundamental frequency on the rotor at synchronous speed is zero that forces the hysteresis loss calculation using (2-4) to be invalid.

An alternative approach to give fast and accurate rotor iron loss evaluation for PWM-fed unloaded induction machines is under investigation. This approach identifies the significant flux density harmonics and calculates eddy-current losses in the frequency domain by summing the contributions of the individual harmonics. This new approach is implemented in three stages.

The first stage is to carry out a time-stepped finite element simulation under the true no-load conditions, i.e. at a very low slip. After a certain number of supply cycles to end the simulation transients, only one supply period of magnetic potential data is required to be recorded, rather than a full slip period of data.

The second stage is to identify the major rotor flux harmonics and exclude the minor harmonics due to the insufficient accuracy of flux density derivative calculation. As known from the basic magnetic circuit relation in an induction machine, the flux density seen by the rotor in the stator reference frame is a function of MMF and permeance harmonics. The frequencies of those harmonics are determined by the electrical frequency of stator current (ω_e), the number of stator slots (N_{st}) and the number of pole pairs (p). Converted to the rotor reference frame, the rotor flux density harmonics can be written as a function in terms of ω_e,

N_{st}, p, the slip (s) and the angle referred to the rotor (θ_r). The approach of direct numerical derivative and integral needs a full slip period of flux density data for rotor eddy-current loss calculation. That approach actually discards the information about spatial distribution of flux that may be obtained through application of engineering knowledge. Rather than considering an element in isolation, one should recognize that it is one of many elements sampling a spatially distributed field. Using this additional information, the magnitude and phase of the individual rotor flux density harmonics may be identified with considerably less computational expense and with a faster response to the machine designer. As the analytical form of the major rotor flux density harmonics is known, one can make use of the additional information by applying linear least squares regression to the one supply period of flux density data collected in the first stage, from a series of spatially distributed elements of similar shape.

The third stage is to find the magnitude of major rotor flux density harmonics according to the results of linear regression, and substitute the harmonic magnitude into the frequency-domain form of (2-3) and (2-6) for a prediction of rotor eddy-current loss with improved accuracy.

Using this approach to simulate PWM operation at rated voltage with a slip speed of 1rpm, the predicted rotor loss is 36.7W, compared to 60.1W predicted by discrete calculation of the rate of change of flux density. Comparing the predicted rotational loss at rated voltage in Table 4-6 with the measured result in Table 4-2, one may find that the reduction by 23.4W is a significant improvement for the no-load loss prediction under PWM supply conditions. This new approach is a topic of ongoing research. This section outlines the application of this new approach to rotor iron loss prediction, and interested readers may refer to [79] for details. Improvements to this method and application of similar approaches to the calculation of stator iron loss are under investigation.

4.4 Summary

This section investigates the relative performance of an induction machine under both sinusoidal and PWM conditions. Combining FEA analysis with test data, some insights into causes of stray losses under PWM supply conditions are presented. It is interesting to note that both the tests and simulations indicate that the majority of additional losses under PWM conditions are actually fundamental frequency losses. As an induction machine becomes more saturated with the increasing load, the additional stray losses due to PWM switching become less significant than in the case of the machine with a lower saturation level. These results of stray loss investigation indicate that improvements to rotor thermal design may be more important to efficiency than PWM switching patterns.

No-load tests and simulations are carried out in an attempt to investigate the relation of stray losses and PWM switching scheme. The sensitivity of numerical predictions of losses under no-load conditions is highlighted, together with the computational difficulty of simulating a machine at very low slip. A possible solution is briefly discussed, forming the start point to further study specifically on no-load or low-load conditions.

Chapter 5 Synchronous Machine Analysis

This chapter generalizes the multislice interbar model to simulate synchronous machines with skewed stator slots. The interbar circuit model is extended in this chapter to model the rotor amortisseur cage. Simulations with a range of interbar contact resistance values are carried out for a synchronous generator to investigate their role in slot harmonics and stray loss in amortisseur cage.

5.1 Synchronous machine modeling

5.1.1 Field winding modeling

The time-stepped finite element modeling of synchronous machines is implemented analogous with the modeling of cage induction machines. A structure special to synchronous machines is the field windings on the rotor. From the modeling perspective, field windings can be treated as stranded conductors similar to the stator windings. The only difference is that the field windings carry a DC current which can be assumed constant in the field excitation equation, and an additional circuit equation is not necessary to model the electric circuit of field windings. The contribution of field current to rotor field is denoted by the following equation in the form similar to (3-4),

$$\nu_0 \frac{\partial^2 \mathbf{A}_{\mathrm{sl}i}}{\partial x^2} + \nu_0 \frac{\partial^2 \mathbf{A}_{\mathrm{sl}i}}{\partial y^2} = -\frac{\gamma N_{\mathrm{f}} I_{\mathrm{f}}}{\Delta_{\mathrm{f}}} \tag{5-1}$$

In (5-1), I_{f} is constant field current, N_{f} is number of turns of field winding, and Δ_{f} is coil side area of field winding. It should be noted that the physical field current contains ripples originating from the field supply (external or internal) and the induced EMF. However these ripples hardly affect the machine performances, and therefore the field supply is modeled as a constant current source, rather than a voltage source which accounts for the ripple effects but brings more modeling complexity by introducing an additional circuit equation.

5.1.2 Generalization of multislice interbar model

In a synchronous machine, the amortisseur is a structure analogous to the induction cage in an induction machine. The skew in a synchronous machine usually occurs at the stator slots in contrast to an induction machine where the skew is applied to the rotor bars. However the skew of stator or rotor relative to the other has a same effect on machine performances, no matter which one is physically skewed from the machine axis. Therefore the multislice interbar technique, which was originally developed for modeling skewed rotor bars in induction machines, can be generalized to model synchronous machines with skewed stator slots.

As mentioned in Section 2.2.1, there is a group of amortisseur bars embedded in the rotor, across each pole pitch, and each bar group may or may not be connected to the groups at the adjacent poles through conductive bridges. Figure 5-1 shows the interbar circuit model for a synchronous machine. The main difference from the interbar circuit models for a synchronous machine and an induction machine is that the former introduces two special parameters, i.e. pole-pole iron resistance (R_{p2p}) and pole-pole end-ring impedance (Z_{p2p}), which connect the adjacent bars belonging to different bar groups. These parameters usually have values different from R_{i} and Z_{end} and dependent on the saliency and pole pitch of

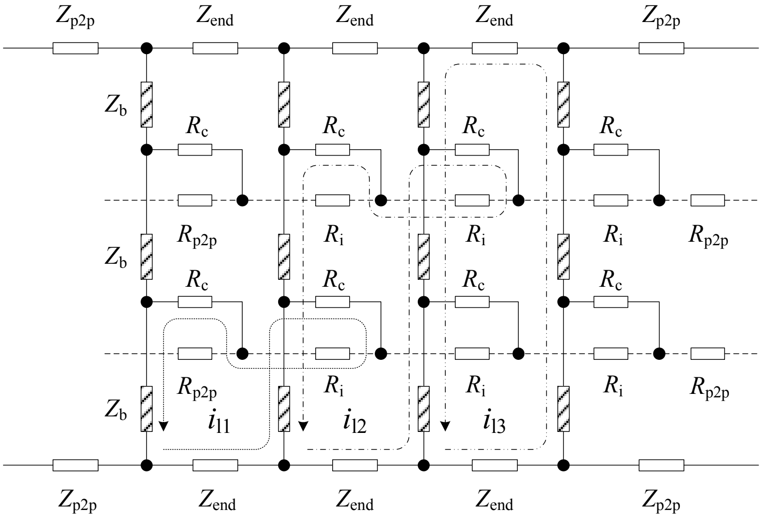

Figure 5-1 Interbar circuit model for a synchronous machine (3-slice example)

the machine. Z_{p2p} is infinity for the special case of nonconnected amortisseurs, where the bar groups are insulated from one another. The circuit equations of amortisseur are in the form similar to the rotor circuit equation of an induction machine, i.e. (3-7) and (3-8). For amortisseur modeling, the matrices $\mathbf{R}_{\mathrm{r}}$ and $\mathbf{L}_{\mathrm{r}}$ in (3-8) are related to not only the values of R_{c}, R_{i} and Z_{end}, which have been used in induction machine models, but also the values of pole-pole parameters, i.e. R_{p2p} and Z_{p2p}.

Applying the modifications introduced in Section 5.1.1 and Section 5.1.2 to the multislice interbar model, one can obtain the synchronous machine system equations that are comprised of (3-2) to (3-8) and (5-1). Provided that the rotor position is known, one may simulate a synchronous motor by simultaneously solving the above equations, or simulate a synchronous generator by simultaneously solving the above equations and a load circuit equation that is coupled with the stator circuit equation (3-6). The procedure to solve the global equation for a synchronous machine is the same as the procedure to solve the induction machine equations. Galerkin method is applied to obtain the finite element form of field equations, and then the time-discretized form of the global equation is derived by C-N method. Considering that the global equation for a synchronous machine still shows no direct coupling between the fields on individual slices, the parallel NR-DD technique can be implemented again for an efficient solution.

5.1.3 Ventilation duct modeling

The core of a large AC machine is usually divided axially into packets of laminations by radial ventilation ducts as shown in Figure 5-2. These ducts allow cooling air to flow radially into the machine, removing heat from the core and windings. The presence of ventilation ducts causes flux fringing from the side of individual ducts and decrease in the average flux density at the air gap under each duct opening. The flux fringing produces axial variation in the air-gap flux density, the influence of ventilation ducts on magnetic circuit and flux density distribution is thereby unable to be modeled by the conventional 2-D FEM.

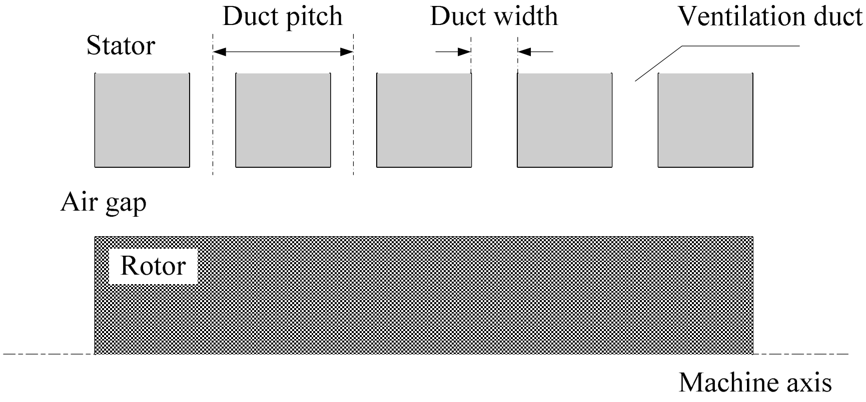

Figure 5-2 Ventilation ducts

In the traditional analytical method for machine magnetic circuit modeling, the presence of ventilation ducts is taken into consideration in a similar way to the winding slots, where the flux fringing also occurs. The fringing of air-gap flux density due to slot openings leads to increase in the average air-gap reluctance, which can be expressed as a decrease in effective area or as an increase in effective air-gap length. Carter shows that the decrease in effective area can be obtained by reducing the slot pitch ε to the effective slot pitch ε' as follows [80]:

$$\varepsilon' = \varepsilon - bw \tag{5-2}$$

where w is slot opening, and b is a factor expressed as

$$b = \frac{2}{\pi}\left\{\tan^{-1}\left(\frac{w}{2g}\right) - \frac{g}{w}\ln\left[1+\left(\frac{w}{2g}\right)^2\right]\right\} \tag{5-3}$$

In (5-3) g is minimum length of air gap. With this transformation the calculation of air-gap flux density is performed as if the flux crossed the uniform air gap over this effective slot pitch. An alternative to reducing the slot pitch is increasing the air-gap length. Carter converted the decrease in width dimension as shown in (5-2) to an equivalent increase in the length dimension on the basis of constant reluctance.

$$\frac{g}{\varepsilon'} = \frac{g'}{\varepsilon} \tag{5-4}$$

According to (5-4) the familiar Carter’s coefficient is written as

$$K_{\mathrm{C}}=\frac{g'}{g}=\frac{\varepsilon}{\varepsilon'}=\frac{\varepsilon}{\varepsilon-bw} \tag{5-5}$$

and it is used to find the effective air-gap length g'.

$$g'=K_{\mathrm{C}}g \tag{5-6}$$

Cochran shows that, similarly to winding slots, the presence of ventilation ducts also can be taken into consideration by using a factor to reduce duct pitch (the width of one stack of laminations plus one vent, as shown in Figure 5-2) or increase air-gap length [81]. If there are N_{d} ducts, each of width w_{d}, the duct pitch is

$$\varepsilon_{\mathrm{d}}=\frac{L+w_{\mathrm{d}}}{N_{\mathrm{d}}+1} \tag{5-7}$$

where L is the overall length of the core, including the ducts. In accordance with (5-5), Cochran multiplies the air-gap length by the following factor to obtain the effective air-gap length:

$$K_{\mathrm{d}}=\frac{\varepsilon_{\mathrm{d}}}{\varepsilon_{\mathrm{d}}-b_{\mathrm{d}}w_{\mathrm{d}}} \tag{5-8}$$

where b_{d} is calculated using (5-3) with w replaced by w_{d}. A number of publications propose the effective reduction in axial core length as an alternative approach to take into consideration the ventilation ducts [82] - [84]. Using a similar procedure embodied in (5-4), Williamson and Flack transform the effective increase in air-gap length to an effective reduction in core length [82]. This effective core length, L', is given by

$$L'=\frac{L}{K_{\mathrm{d}}}=L\left(1-\frac{N_{\mathrm{d}}+1}{L+w_{\mathrm{d}}}b_{\mathrm{d}}w_{\mathrm{d}}\right) \tag{5-9}$$

Liwschitz-Garik and Whipple give (5-9) with an approximate expression for b_{d} [83]. With the assumption $N_{\mathrm{d}} >>1$, $L>>w_{\mathrm{d}}$, Say gives an equivalent expression for L' as follows [84]:

$$L'=L-N_{\mathrm{d}}b_{\mathrm{d}}w_{\mathrm{d}} \tag{5-10}$$

With the traditional analytical approach to model magnetic fields in AC machines, Carter's coefficients as (5-5) and (5-8) are usually determined and applied successively for the stator slots, the rotor slots and the radial ventilation ducts, to create the effective air gap or core length. The presence of slots causes radial and tangential variations of the flux density that are automatically modeled with the 2-D FEM. The axially spaced radial ducts cause axial variation of the flux density that are beyond the plane used with the traditional 2-D FEM. Fortunately, modified 2-D FEA can be carried out by simply replacing the physical core length in the system equation with the effective core length calculated as (5-9) or (5-10). This transformation does not incur any change to the 2-D finite element mesh.

It should be noted that the above approach is equally valid for both stator and rotor ducts. Large synchronous machines usually have ventilation ducts in the stator core only, while rotor ducts for synchronous machines are less common. In this case, K_{d} is computed by substituting only the stator duct parameters into (5-8), and the effective core length is then computed as (5-9). When both stator and rotor have ventilation ducts, as is the case of a large induction machine, K_{ds} and K_{dr} must be computed respectively for stator and rotor by substituting the stator and rotor duct parameters into (5-8). Then the two Carter's coefficients are applied successively as shown in (5-11) to compute the effective core length.

$$L' = \frac{L}{K_{\mathrm{ds}} K_{\mathrm{dr}}} \tag{5-11}$$

5.2 Outline of simulation and experiment conditions

The amortisseur cage in a synchronous machine carries induced harmonic currents at slot frequencies that respond to the periodic variations in reluctance and air-gap flux density caused by stator slotting. It can be extrapolated that variation in the bar-iron contact resistance due to the uncertainty in manufacturing process has evident influence on magnitude of the rotor harmonic currents, and hence on stray losses in amortisseur cage. As these harmonic currents act on the machine magnetic field, variation in certain output harmonics, e.g. the open-circuit voltage harmonics, may be observed as a reflection of interbar resistance variation. The simulations and experiments in this section aim to investigate the reaction of these slot harmonics and the resulting cage stray loss to the interbar resistance variation.

The synchronous machine investigated in this chapter is a 3-phase, Y-connected, large salient-pole synchronous generator provided by GE Canada. All the experiment results regarding this machine are also provided by GE Canada. The machine nameplate data are presented in Table 5-1. This machine has a skew of one slot pitch, and the rotor is equipped with a connected amortisseur. The basic structure parameters are omitted here for the purpose of confidentiality.

Table 5-1
Synchronous machine nameplate data

Rated VA	14.089MVA
Rated voltage	13.8kV
Frequency	60Hz

Simulations are carried out using a 4-slice finite element model with the generalized interbar circuit and the effective core length. According to the rotational symmetry the machine structure displays, a finite element mesh is created for the sector of one pole as shown in Figure 5-3. The mesh consists of 3646 nodes and 6788 first-order triangular elements, not including the dynamic air-gap elements. Following the test procedures in IEEE Standard 115, simulations are carried out under open-circuit and short-circuit conditions, respectively. Prior to a synchronous machine simulation, a magnetostatic FEA with the field current as the input is usually necessary in order to find the initial nodal magnetic potentials. The time-stepped simulation with rotor motion is subsequently initialized by substituting these initial values of nodal potential for $\mathbf{A}_{\mathrm{N}}^{t}$ in the global equation at the first time step. These initialization procedures are not required for induction machine simulations. One may simply assume zero initial conditions because the rotor cage can automatically dampen out the transients caused by initial sudden change in excitation. In addition, soft start conditions may be adopted to gradually increase the excitation during the initial stage of simulation, for the cases of long transients. In a synchronous machine

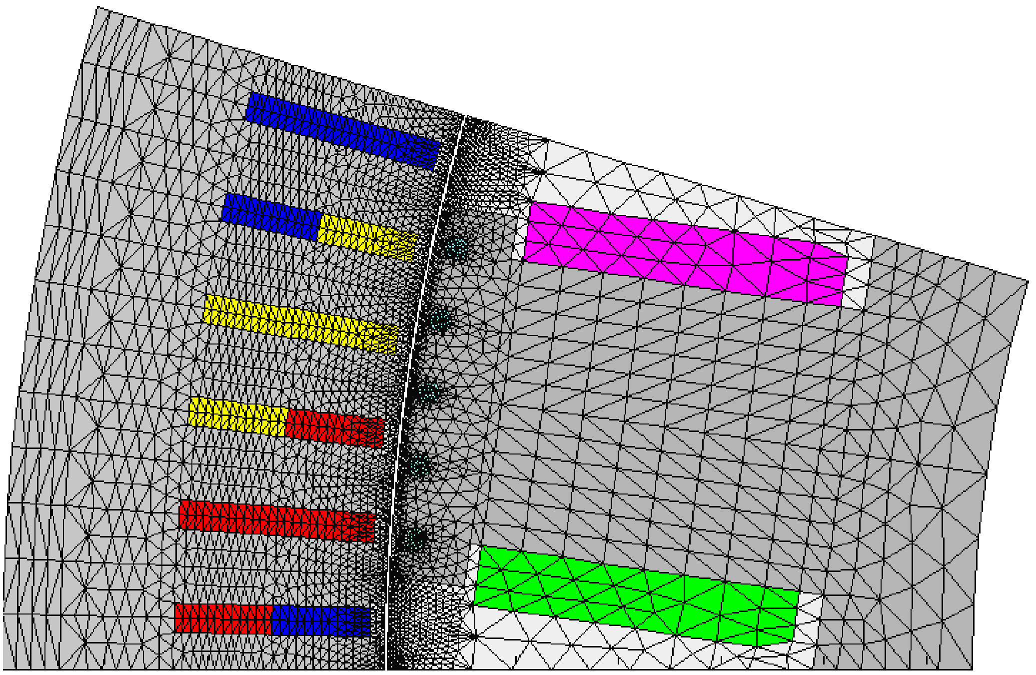

Figure 5-3 Finite element mesh of a synchronous machine

under steady-state operation, the amortisseur cage is unable to function as the squirrel-cage damper in an induction machine. Due to the lack of damping, synchronous machine simulations without initial magnetostatic solution may produce oscillations or intractably long transients.

5.3 Open-circuit simulations and experiments

The synchronous generator model developed in Section 5.1 is generally available to simulations under various load conditions. Simulations for the special case of open-circuit operation can be carried out by setting the stator resistance R_s to a very large value and setting the terminal voltage $\mathbf{V}_s$ to zero in the stator circuit equation (3-6). With these small modifications, (3-6) describes the case that an EMF induced by the rotor field is applied to a closed stator circuit with very large impedance, which limits the stator current $\mathbf{I}_s$ to nearly zero. From the perspective of the machine magnetic field, the state of generator with this stator circuit is effectively equivalent to an open-circuit operation.

5.3.1 Electromotive force calculation

The main goal of this section is to extract the slot harmonic components of the open-circuit voltage (EMF) and investigate their relation to the rotor interbar resistances. The induced EMF can be calculated using the nodal magnetic potentials obtained from the solution of the system equation. Figure 5-4 shows a stator coil comprised of two effective coil sides (a and b) exposed to the 2-D magnetic field in a machine. L is the effective length of the coil, i.e. the core length. $\mathbf{A}_\mathrm{a}$ and $\mathbf{A}_\mathrm{b}$ are the magnetic potentials at the coil sides a and b, respectively.

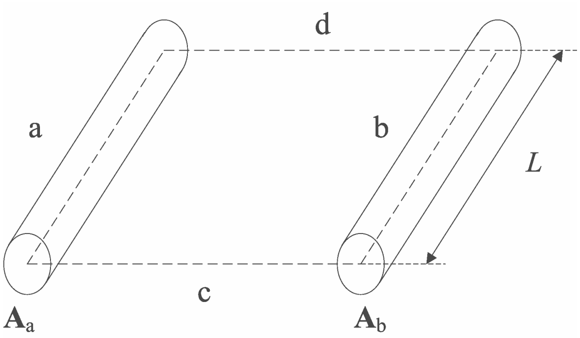

Figure 5-4 Calculation of the flux through a coil

The magnetic flux through this coil is given by

$$\phi = \oint_{\mathrm{acbd}} \mathbf{A}\mathrm{d}l = \mathbf{A}_\mathrm{a} l - \mathbf{A}_\mathrm{b} l \tag{5-12}$$

For stator windings comprised of coils of N_t turns, the magnetic potentials used for flux linkage calculation must be the average over the area of coil side. This average magnetic potential is expressed by

$$\overline{\mathbf{A}}_\mathrm{cs} = \frac{1}{\Delta_\mathrm{cs}} \sum_i \frac{\Delta_{\mathrm{e}i}}{3} \sum_{j=1}^{3} \mathbf{A}_{\mathrm{e}i\,\mathrm{n}j} \tag{5-13}$$

where $\mathbf{A}_{\mathrm{e}i\,\mathrm{n}j}$ is the magnetic potential at the jth node of the ith element in a coil side, and $\Delta_{\mathrm{e}i}$ is the area of this element. In an N_sl-slice model, if a phase winding consists of N_cs coil sides that form N_c parallel circuits, the total flux linkage of one phase is given by

$$\psi = \frac{N_\mathrm{t} L_\mathrm{sl}}{N_\mathrm{c}} \sum_{m=1}^{N_\mathrm{sl}} \sum_{k=1}^{N_\mathrm{cs}} \gamma_k \overline{\mathbf{A}}_{km} \tag{5-14}$$

where $\overline{\mathbf{A}}_{km}$ is the average magnetic potential at the *k*th coil side in the *m*th slice, and γ_k is ±1 depending on the direction of this coil side. The time-stepped phase EMF can be derived as follows:

$$E_{\mathrm{p}}^{t+\Delta t} = -\frac{\psi^{t+\Delta t} - \psi^{t}}{\Delta t} = -\frac{N_{\mathrm{t}} L_{\mathrm{sl}}}{N_{\mathrm{c}} \Delta t} \sum_{m=1}^{N_{\mathrm{sl}}} \sum_{k=1}^{N_{\mathrm{cs}}} \gamma_k \left(\overline{\mathbf{A}}_{km}^{t+\Delta t} - \overline{\mathbf{A}}_{km}^{t} \right) \tag{5-15}$$

5.3.2 Simulation and experiment results

The harmonic components of measured and simulated open-circuit line-line voltage are obtained from fast Fourier Transform (FFT) and presented in Table 5-2. These results are normalized to per unit values with the measured fundamental voltage as the baseline value. The simulation results obtained from the proposed multislice interbar model are given at a wide range of possible interbar resistances, from $1\times10^{-5}\Omega$m to $1\times10^{-1}\Omega$m. To illustrate the advantage of proposed model in predicting slot harmonics, the additional results obtained from a 2-D finite element model modified by skew factor are also given in Table 5-2, as an object of comparison. The first step of this approach is to calculate the open-circuit voltage with the conventional single-slice finite element model, as is used in most commercial 2-D FEA packages. The stator slots are assumed unskewed in the first step of calculations. The second step is to account for the effect of skewed slots on open-circuit voltage by correcting each of their harmonics obtained through FFT, with an analytical factor. This factor, known as the "skew factor", is reproduced in numerous textbooks, such as [81]. Skew factor has been commonly used in analytical models of skewed AC machines to correct the air-gap flux density calculated with the assumption of unskewed slots or bars. This factor is expressed by

$$K_{\mathrm{s}} = \frac{\sin\left(\frac{n\beta}{2}\right)}{\frac{n\beta}{2}} \tag{5-16}$$

where β is the skew angle in radian, as shown in Figure 2-4, and n is the harmonic order.

Table 5-2
Normalized open-circuit line-line voltage harmonics of a synchronous machine

Harmonic order	Measured RMS	Simulated RMS modified by skew factor	Simulated RMS with multislice interbar model at different interbar resistances								
			1×10^{-5} Ωm	4×10^{-5} Ωm	1×10^{-4} Ωm	4×10^{-4} Ωm	1×10^{-3} Ωm	4×10^{-3} Ωm	1×10^{-2} Ωm	4×10^{-2} Ωm	1×10^{-1} Ωm
1	1.000	1.003	1.017	1.017	1.017	1.017	1.017	1.017	1.017	1.017	1.017
3	8.20×10^{-5}	1.07×10^{-3}	1.56×10^{-5}	1.58×10^{-5}	1.59×10^{-5}	1.60×10^{-5}	1.63×10^{-5}	1.67×10^{-5}	1.68×10^{-5}	1.69×10^{-5}	1.69×10^{-5}
5	3.97×10^{-3}	3.91×10^{-3}	4.11×10^{-3}	4.11×10^{-3}	4.11×10^{-3}	4.12×10^{-3}	4.13×10^{-3}	4.14×10^{-3}	4.14×10^{-3}	4.14×10^{-3}	4.14×10^{-3}
7	2.56×10^{-3}	3.58×10^{-3}	3.36×10^{-3}	3.36×10^{-3}	3.37×10^{-3}	3.37×10^{-3}	3.37×10^{-3}	3.39×10^{-3}	3.40×10^{-3}	3.40×10^{-3}	3.40×10^{-3}
11	2.06×10^{-3}	6.15×10^{-3}	2.30×10^{-3}	2.30×10^{-3}	2.30×10^{-3}	2.30×10^{-3}	2.25×10^{-3}	1.76×10^{-3}	1.20×10^{-3}	7.74×10^{-4}	6.91×10^{-4}
13	5.54×10^{-3}	9.86×10^{-3}	5.46×10^{-3}	5.46×10^{-3}	5.46×10^{-3}	5.52×10^{-3}	5.64×10^{-3}	5.34×10^{-3}	5.02×10^{-3}	4.90×10^{-3}	4.88×10^{-3}
17	3.21×10^{-4}	1.60×10^{-4}	7.50×10^{-4}	7.51×10^{-4}	7.51×10^{-4}	7.36×10^{-4}	6.73×10^{-4}	5.67×10^{-4}	5.39×10^{-4}	5.26×10^{-4}	5.24×10^{-4}
19	1.79×10^{-4}	7.57×10^{-5}	1.85×10^{-4}	1.85×10^{-4}	1.85×10^{-4}	1.82×10^{-4}	1.73×10^{-4}	1.57×10^{-4}	1.50×10^{-4}	1.46×10^{-4}	1.45×10^{-4}
23	6.83×10^{-4}	3.20×10^{-4}	1.18×10^{-3}	1.18×10^{-3}	1.18×10^{-3}	1.08×10^{-3}	7.29×10^{-4}	4.12×10^{-4}	3.99×10^{-4}	4.64×10^{-4}	5.03×10^{-4}
25	3.96×10^{-4}	2.20×10^{-4}	9.28×10^{-4}	9.28×10^{-4}	9.28×10^{-4}	9.53×10^{-4}	1.04×10^{-3}	1.52×10^{-3}	1.97×10^{-3}	2.27×10^{-3}	2.31×10^{-3}

The 12 slots over a pair of poles in this machine give rise to the periodic variation of reluctance, which results in the harmonic components of induced amortisseur bar currents at the frequencies of multiples of the 12th harmonic. These harmonic bar currents produce forward and backward rotor fields which rotate at the speeds of $(12k \pm 1)n_s$ (n_s is synchronous speed and $k = 1, 2, 3, \ldots\ldots$) relative to the stator. These rotor fields superimpose the 11th, 13th, 23rd, 25th, etc. harmonics on the induced open-circuit voltage.

Table 5-2 shows the selected significant harmonics of the measured and simulated open-circuit voltages up to the 25th harmonic. The above analysis suggests that the main origin of the 11th, 13th, 23rd and 25th harmonics is the modulation effect of stator slots. The other harmonic components in Table 5-2 come into being as a result of the saturation in the iron core or the design of certain constructions such as the distribution of stator windings and the shape of pole face. The results given by the multislice interbar model indicate that the variation of interbar resistance clearly influences the magnitude of slot harmonics in open-circuit voltage. On the other hand, the magnitude of other harmonics due to the reasons other than slots does not change significantly with the interbar resistance variation. For example, the phase belt voltage harmonics, such as the 5th and 7th harmonics, remain constant at the wide range of interbar resistances. The slot harmonics in open-circuit voltage are most sensitive to the variation in interbar resistance at the order of magnitude of 10^{-4} Ωm to 10^{-3}Ωm. On the contrary, the variations of interbar resistance have only minor effect on the slot harmonics of open-circuit voltage if the amortisseur bars are insulated very well, e.g. the bar-iron contact resistance is in a range greater than 1×10^{-2}Ωm, or they are poorly insulated, e.g. the bar-iron contact resistance becomes smaller than 1×10^{-4}Ωm that is comparable to the bar resistance. In the simulation results at a variety of interbar resistances, the case of 1×10^{-3}Ωm shows the best agreement with the measured results at the slot harmonic frequencies. This implies that the average interbar resistance in this machine is approximately at the order of magnitude of 10^{-3}Ωm. Figure 5-5 shows a certain instantaneous open-circuit flux distribution under the interbar resistance of 1×10^{-3} Ωm. The differences in stator tooth fluxes can clearly be seen.

As a compromise that accounts for the skewed slots, the skew factor approach is computationally cheaper but less complete than the multislice interbar modeling technique. To compare the simulation accuracy, the harmonics predicted by the skew factor approach are presented in Figure 5-6 together with the measured result and the simulation result at the interbar resistance of 1×10^{-3}Ωm. It is evident

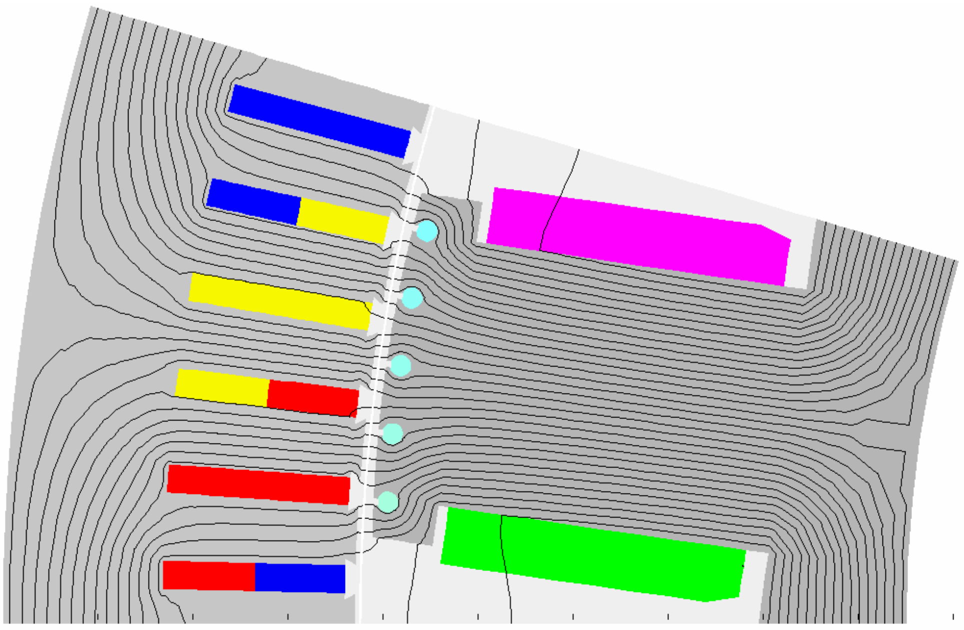

(a) Slice 1

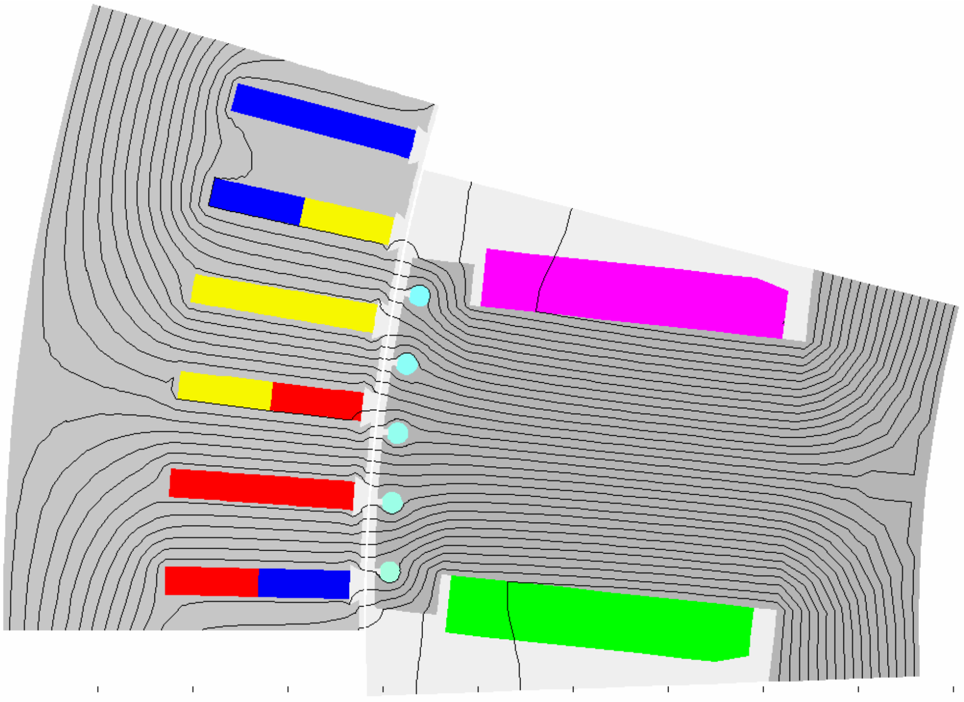

(b) Slice 4

Figure 5-5 Fluxes in an open-circuit synchronous machine

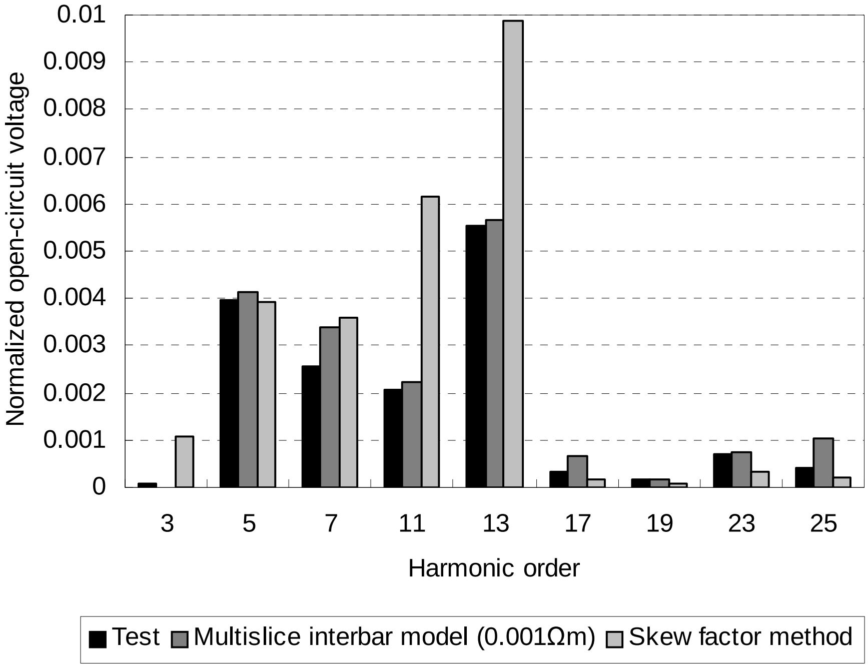

Figure 5-6 Comparison of measured and simulated open-circuit voltages

that, at the slot harmonic frequencies, the results given by the proposed model fundamentally match the measured results better than the results given by the skew factor approach. It should be underlined that the accuracy of harmonic prediction tends to be difficult as the harmonic order increases. As one may notice in Figure 5-6, there is a relatively large error in the predicted 25th harmonic given by the proposed model. The reason for this error is that the cubic spline interpolation of *B-H* curve used in the numerical simulations may not give sufficiently accurate prediction of the small variation in flux density. The investigation on a cage induction motor in [85] indicates that much of the slot harmonic flux closes on itself in a layer close to the rotor surface. It is considered reasonable that the similar phenomenon occurs on the stator inner surface in a synchronous machine that is excited by the rotor field windings. Only a small amount of harmonic flux at the high slot frequencies penetrates into the stator core, embraces an entire slot through the relatively low reluctance path provided by the teeth, and hence induces the slot harmonic EMF in stator windings. The *B-H* curve may not be measured and interpolated with sufficient data points to allow accurate prediction of such a small variation in flux density.

The amortisseur bar currents consist of slot harmonics only. Figure 5-7 shows the magnitude of the simulated 12th and 24th current harmonics (720Hz and 1440Hz) flowing in the individual slices of a certain amortisseur bar. The figure displays noticeable bar current variation along the axial direction, indicating the transverse currents of significant magnitude flowing into the rotor core. It can be found that the axial variation in bar current is more prominent when the order of magnitude of interbar resistance is $10^{-4}\Omega$m to $10^{-3}\Omega$m. This fact shows an agreement with the sensitivity of slot harmonics in open-circuit voltage to the interbar resistance. The currents in the individual bar segments tend to be uniform as the interbar resistance increases, implying the decreased transverse currents in the cases of better insulation.

5.4 Short-circuit simulations and experiments

5.4.1 Simulation settings

This section aims to use simulation technique to investigate the composition of stray-load loss as is defined and measured under short-circuit operation, in compliance with IEEE Standard 115. The components of stray-load loss include stator iron loss, rotor iron loss and amortisseur cage loss. The simulation of short-circuit operation can be achieved with $\mathbf{V}_s$ in (3-6) set to zero. The simulated range of interbar resistances is $1\times10^{-5}\Omega$m to $1\times10^{-1}\Omega$m, identical to that in the open-circuit simulations.

The stray-load loss under short-circuit operation is evaluated by measurements and simulations. The stator and rotor lamination parameters that are used for calculation of iron losses are presented in Table 5-3. The approach to evaluate stator iron loss for synchronous machines is identical to that for induction machines, i.e. calculating the eddy-current loss, hysteresis loss and excess loss as (2-3), (2-4) and (2-6), respectively. The rotor iron loss evaluation for synchronous machines usually excludes the hysteresis loss component for the similar reason mentioned in Section 4.3.2 B. In that section, the rotor hysteresis loss are not considered when calculating the rotor iron loss in an induction motor at synchronous speed, because the hysteresis loss produced by minor hysteresis

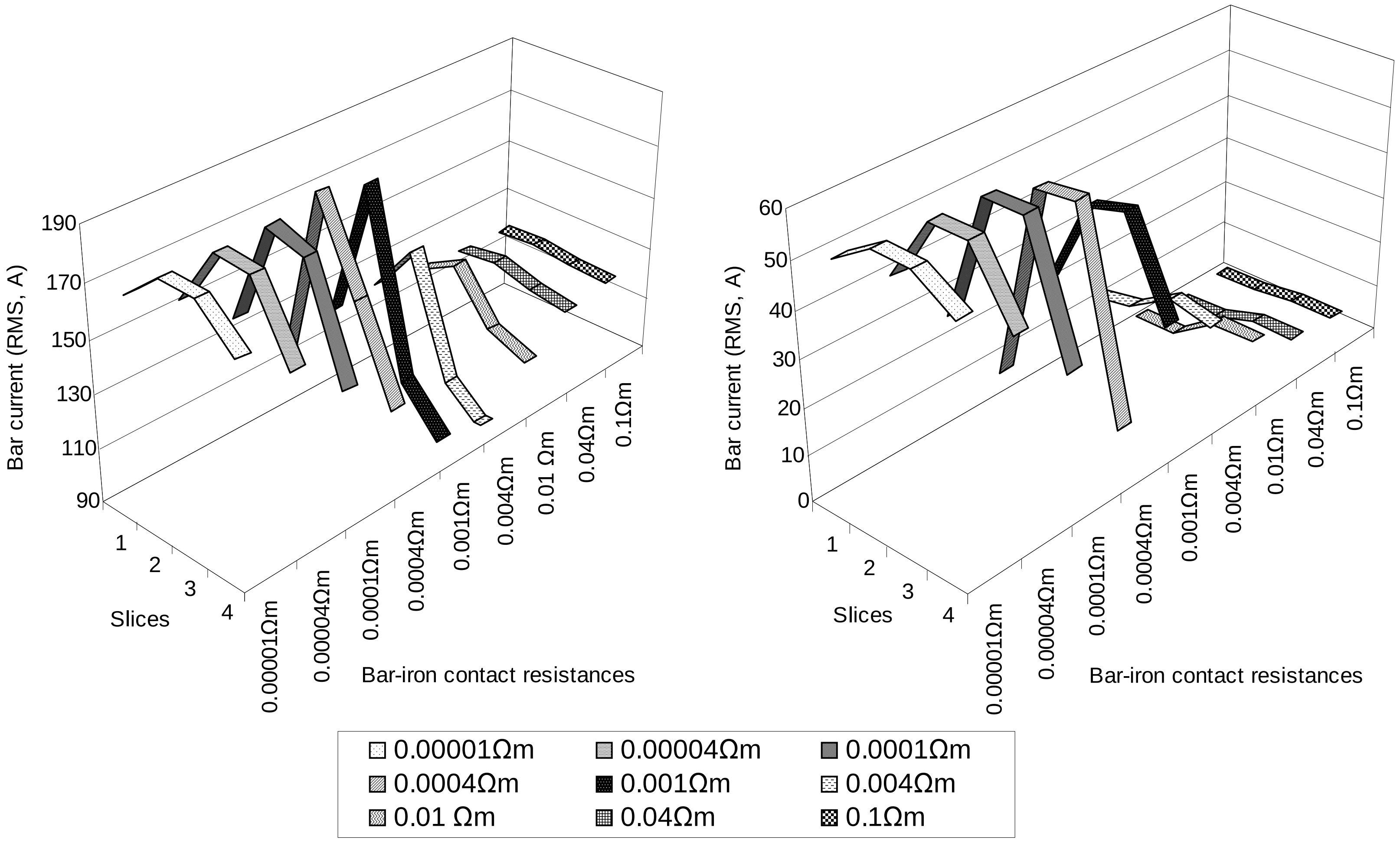

(a) Bar current harmonic at 720Hz

(b) Bar current harmonic at 1440Hz

Figure 5-7 Amortisseur bar current in an open-circuit synchronous machine

Table 5-3
Lamination parameters of a synchronous machine

Stator lamination thickness	0.483mm
Stator lamination conductivity	1.923×10^{6}S/m
Rotor lamination thickness	1.880mm
Rotor lamination conductivity	6.864×10^{6}S/m
Mass density of laminations	7650kg/m^{3}
α	1.828
k_{h}	0.0195
k_{e}	2.12×10^{-5}

loops is usually assumed negligible. The rotor field in a synchronous machine is fundamentally constant with the similar minor hysteresis loops, which are caused by stator slot openings and stator current harmonics as in an induction machine. Thus the evaluation of rotor iron loss in a synchronous machine also neglects the component of hysteresis loss. However, the rotor flux density fluctuations still produce eddy-current loss and excess loss, and these losses are taken into account as rotor iron loss components.

5.4.2 Simulation and experiment results

The short-circuit measurement and simulation results are given in Table 5-4. The results are normalized to per unit values with the measured stray-load loss and short-circuit current as the baseline values. A breakdown of the simulated stray-load losses at different interbar resistances is presented in Table 5-4. The simulation results indicate that a significant proportion of the stray-load loss comes for the harmonic Joule loss in amortisseur cage. The ratio of this cage stray loss to the total stray-load loss may change significantly with the variation in interbar resistance. For instance, the simulation results in Table 5-4 show that this ratio is as low as 8.86% at the interbar resistance of $1.0\times10^{-5}\,\Omega$m, reaches the peak as high as 29.35% at the interbar resistance of $1.0\times10^{-3}\Omega$m, and decreases to 20.91% at the interbar resistance of $1.0\times10^{-1}\Omega$m. Due to the variation in cage

Table 5-4
Normalized short-circuit operation results of a synchronous machine
Measured results

Total stray-load loss	1.0000
Short-circuit current	1.0000

Simulated results

Simulated performances	Interbar resistances (Ωm)								
	1×10^{-5}	4×10^{-5}	1×10^{-4}	4×10^{-4}	1×10^{-3}	4×10^{-3}	1×10^{-2}	4×10^{-2}	1×10^{-1}
Short-circuit current	0.9688	0.9688	0.9688	0.9690	0.9690	0.9688	0.9688	0.9688	0.9688
Total stray-load loss	0.7638	0.7925	0.8309	0.9354	0.9875	0.9510	0.9089	0.8766	0.8693
Stator iron loss	0.1856	0.1877	0.1876	0.1876	0.1875	0.1872	0.1871	0.1870	0.1870
Total rotor loss	0.5782	0.6048	0.6433	0.7478	0.8000	0.7638	0.7219	0.6896	0.6823
Rotor iron loss	0.5105	0.5124	0.5112	0.5106	0.5101	0.5054	0.5016	0.5006	0.5005
Cage stray loss	0.0677	0.0924	0.1321	0.2372	0.2899	0.2584	0.2203	0.1890	0.1818
Ratio of cage loss to total loss (%)	8.86	11.66	15.90	25.36	29.35	27.18	24.23	21.56	20.91

stray loss component, the total stray-load loss also displays an evident dependence on the interbar resistance. The total stray-load loss and the cage stray loss component both reach their peaks when the interbar resistance is approximately at the order of magnitude of 10^{-3}Ωm. These losses are lower when the interbar resistance is as low as comparable to the bar resistance or sufficiently high as the case of perfect bar-bar insulation. The simulated stray-load loss at the interbar resistance of $1.0\times10^{-3}\Omega\text{m}$ matches the measured result. Figure 5-8 shows a

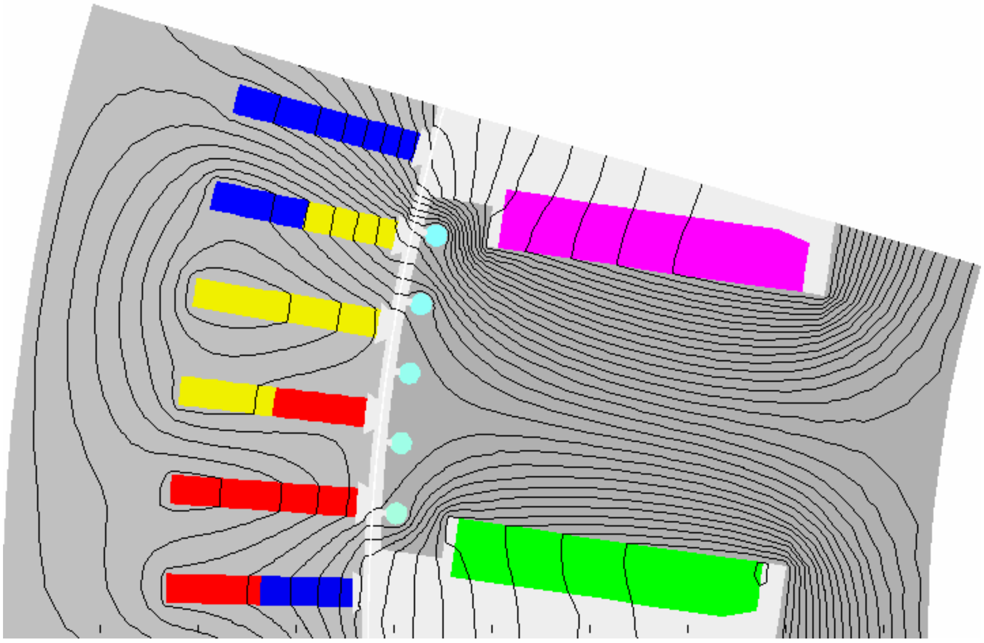

(a) Slice 1

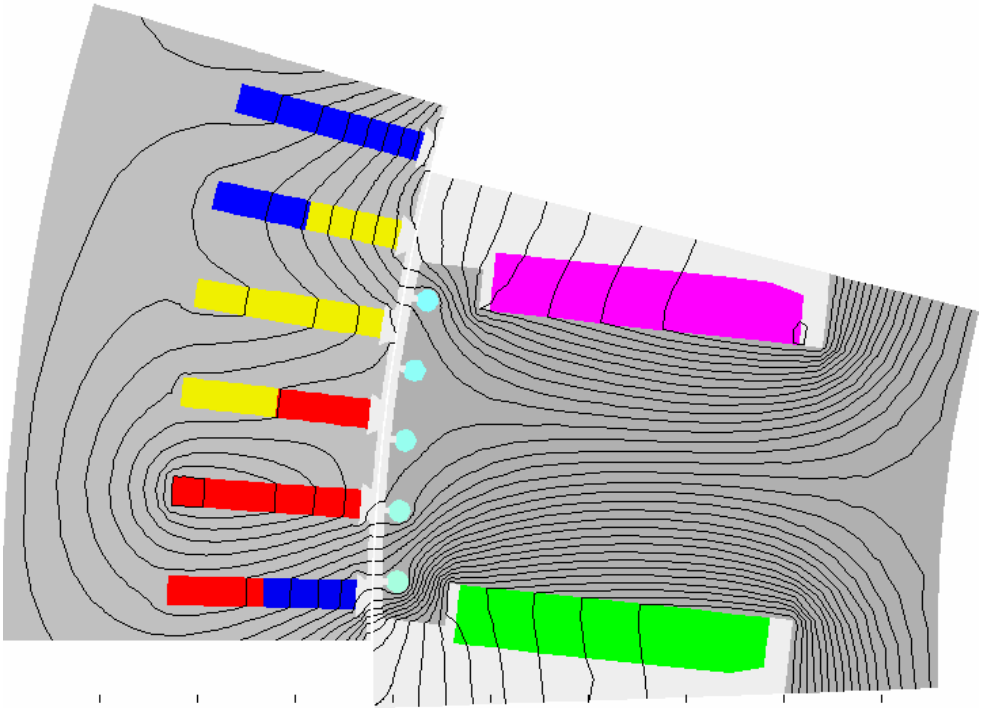

(b) Slice 4

Figure 5-8 Fluxes in a short-circuit synchronous machine snapshot of flux distribution in the synchronous machine under this interbar resistance condition. The flux density distribution on the pole face of a short-circuit synchronous machine is evidently less even than that in an open-circuit synchronous machine due to the armature reaction.

5.5 Discussion on rotor iron loss evaluation for synchronous machines

The iron sheets from which the rotor core of this machine is manufactured are as thick as 1.88mm, significantly thicker than the typical laminations. Trial simulations indicate that an accurate prediction of the eddy-current loss in this rotor core is technically difficult in some cases. The eddy-current loss formulation as (2-3) is based on an assumption of uniform distribution of the magnetic field across the lamination thickness. However, this assumption is valid only if the iron sheets are sufficiently thin. Skin effect should be taken into account for iron sheets whose thickness is comparable with the skin depth. The alternating component of magnetic field may concentrate on the surface of the thick sheets and increase the effective flux density. Skin depth is a measure of the distance over which the harmonic flux density falls to 1/*e* of its original value. For a harmonic flux density at the radian frequency of ω, the skin depth is denoted by

$$\delta = \sqrt{\frac{2}{\mu_{\mathrm{m}} \sigma_{\mathrm{m}} \omega}} \qquad (5\text{-}17)$$

where μ_{m} is average permeability in the iron. (5-17) suggests that the skin depth depends on the local saturation in laminations. A lamination region exposed to saturated field possesses a lower permeability and hence a larger skin depth with respect to each flux density harmonic. On the other hand, an unsaturated iron region displays a smaller skin depth due to the higher permeability. For this reason, a general expression of eddy-current loss that accounts for the local saturation level and skin depth, is required in order to improve the accuracy of eddy-current loss prediction for thick laminations.

Dreyfus developed an analytical approach that multiplies the conventional frequency-domain expression of eddy-current loss by a factor to predict the eddy-current loss under skin depth condition [86]. If skin depth is not considered, the lamination eddy-current loss density (in W/m^3) corresponding to the harmonic flux density at the radian frequency of ω is given as follows:

$$P_{\mathrm{e}}\left(\omega\right)=\frac{\sigma_{\mathrm{m}}d^{2}\omega^{2}}{24}\hat{B}_{\omega}^{2} \tag{5-18}$$

where $\hat{B}_{\omega}$ is magnitude of flux density at the radian frequency of ω. The factor that is used by Dreyfus to modify (5-18) is given by

$$K_{\mathrm{sk}}=\frac{3}{\xi}\cdot\frac{\sinh\xi-\sin\xi}{\cosh\xi-\cos\xi} \tag{5-19}$$

where

$$\xi=\frac{d}{\delta} \tag{5-20}$$

Thus an alternative expression of lamination eddy-current loss density that takes into account the skin depth is given as follows:

$$P_{\mathrm{e\,sk}}\left(\omega\right)=K_{\mathrm{sk}}P_{\mathrm{e}}\left(\omega\right)=\frac{\sigma_{\mathrm{m}}d^{2}\omega^{2}(\sinh\xi-\sin\xi)}{8\xi\left(\cosh\xi-\cos\xi\right)}\hat{B}_{\omega}^{2} \tag{5-21}$$

To predict the total eddy-current loss in thick laminations, the calculation shown in (5-21) must be implemented for individual lamination elements at individual harmonic frequencies, with $\hat{B}_{\omega}$ provided by FFT of the finite element solution.

Although (5-21) provides an improved approach to calculate eddy-current losses in thick laminations, this approach still may not guarantee the calculation accuracy for some local regions with low flux density. The practical magnetizing curve of the iron core displays a relatively high reluctivity in the segment of “reversible growth” subject to a low external field, as shown in Figure 5-9. This reluctivity decreases in the transition to the region of “irreversible growth”, i.e. producing a negative gradient of reluctivity. The negative gradient may result in negative diagonal entries of the matrix $\mathbf{G}_k$ in (3-19), and harm the convergence of numerical simulations. For this reason, in the practical simulations, the “reversible growth” segment of the magnetizing curve is replaced with an approximate linear representation that has an equal slope with the segment of “irreversible growth”. With this approximate representation, the permeability of elements with very low

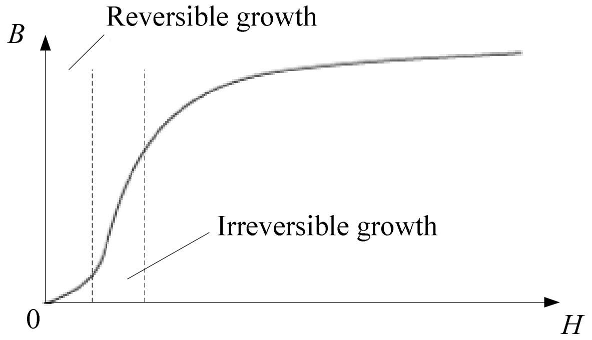

Figure 5-9 Magnetizing curve of iron core

flux density is overpredicted, and hence errors may be created when calculating skin depth and eddy-current loss density of these elements as (5-17) and (5-21). The simulation error of the total eddy-current loss in thick laminations may be considerable if there are a large number of such regions with low flux density.

Evaluation of rotor iron loss in synchronous machines is a topic for future investigation. The above discussion is motivated by the special case of thick laminations in this rotor iron core. Some general factors (e.g., minor hysteresis loops) also may be worthy of investigation for more credible evaluation of rotor iron losses in synchronous machines. It is encouraging that an insight into the factors affecting rotor stray losses in synchronous machines is obtained from the loss breakdown shown in Table 5-4, though the simulation results of rotor iron losses might be questionable quantitively. The simulations reveal clearly the tendency of cage stray loss and total rotor stray loss under different interbar resistances.

5.6 Summary

This chapter develops a 2-D multislice finite element model for a large salient-pole synchronous machine with skewed stator slots. Simulations and experiments are carried out to investigate the harmonics and the resulting stray losses in this machine. The magnitude of harmonics due to stator slot openings is found subject to the value of rotor interbar resistance. The simulation results indicate that a number of performances such as open-circuit voltage, amortisseur bar currents and stray-load loss, are significantly influenced by the variation in interbar resistance. The data and curves obtained from the simulations will be beneficial to an improvement of rotor interbar insulation for the purpose of mitigation of slot harmonics and stray losses in synchronous machines.

It is noted that accurate calculation of rotor iron loss in this synchronous machine is a challenging issue worthy of special attention. A modified equation that accounts for the skin depth of the thick rotor laminations in this machine is required in order to improve the calculation accuracy of the eddy-current loss in the rotor core. It is also acknowledged that other unknown factors affecting the calculation of rotor iron loss in regular synchronous machines (with typical lamination thickness) may be existent and worthy of future investigation.

Chapter 6 Permanent Magnet Synchronous Machine Analysis

6.1 Introduction

In the previous three chapters, multislice 2-D finite element models with interbar circuit have been established for skewed induction machines and synchronous machines. The harmonic stray losses in AC machines are investigated using these models, under a variety of PWM supply and rotor interbar insulation conditions. The shape and dimension of stator and rotor slots also play an important role in the formation of harmonic stray loss. An appropriate design of slot geometry helps reduce the stray loss caused by slot harmonics.

This chapter attempts to optimize the shape of slots in a PMSM in order to minimize the machine loss. This PMSM is utilized to accelerate or decelerate the rotating mass in a flywheel energy storage system. A power electronic converter controls the power flow during the process of energizing (the PMSM is motoring) and deenergizing (the PMSM is generating) the flywheel. The energy loss occurring in the mechanical-electrical energy conversion is one of the primary concerns regarding a flywheel system. Even though PMSMs are typically considered to be high efficiency machines, particular attention should be made to losses in a machine designed for use with a flywheel. Total loss should be as low as possible in order to maximize round-trip energy efficiency. The rotor of the system is typically evacuated, eliminating conductive and convective heat transfer from the rotor. Due to the difficulty in removing the heat from the rotor, high frequency eddy current losses in the magnets should be minimized to protect the magnets from performance degradation or permanent malfunction. Adjustment of the slot shape is an economic approach to reduce the total loss, and particularly the magnet stray loss in a PMSM.

The slot shape optimization in this chapter involves two techniques that are integrated into one computer program: the optimum seeking algorithm based on

ES is implemented as the outer loop to repeatedly adjust the slot design; time-stepped finite element simulations are carried out as a nested loop in the body of optimization loop to calculate the losses for the individual designs.

6.2 Permanent magnet synchronous machine modeling

This section aims to develop a time-stepped finite element model for PMSMs which is used to provide the information of flux density distribution for loss calculation. The machine investigated in this chapter has fractional-slot windings in unskewed slots, and there is no amortisseur assembled with the rotor. As the time-stepped finite element models for the common structures or regions in all types of AC machines, such as core laminations, stator windings and air gap region, have been established in Chapter 3, this section focuses on modeling of permanent magnets, the parts particular to a PMSM, and calculation of magnet stray loss caused by eddy currents.

A permanent magnet is a type of hard magnetic material that is characterized by a wide hysteresis loop. The magnets commonly used in permanent magnet machines usually exhibit a linear normal magnetization characteristic in the second quadrant, as shown in Figure 6-1. The slope of the straight line shown in Figure 6-1, i.e. the permeability of a permanent magnet is only slightly greater than that of free space. A permanent magnet machine must be designed to operate in the second quadrant of the magnet’s hysteresis loop so that the magnet will not be demagnetized when exposed to an external repellent field. The magnets in

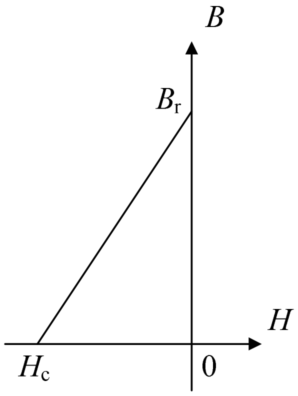

Figure 6-1 Linear magnetization characteristic of a permanent magnet

many permanent magnet machines are segmented in order to reduce the magnet eddy-current loss. The main goal of this chapter is to investigate the effect of slot shape on the total machine loss and the magnet stray loss. The adoption of solid pieces or thin sheets of magnet in a simulation model does not affect the assessment of various slot shape designs and the final selection from them. Therefore, for modeling convenience, it is assumed that the machine is equipped with solid magnets, and a single-slice finite element model can be applied considering the unskewed structures. The single-slice field equation for a solid permanent magnet is given by

$$\nabla \times (\nu \nabla \times \mathbf{A}) = \mathbf{J}_{\mathrm{e}} + \mathbf{J}_{\mathrm{pm}} \tag{6-1}$$

where $\mathbf{J}_{\mathrm{e}}$ is the eddy current density in the magnet, and $\mathbf{J}_{\mathrm{pm}}$ is the term of equivalent current density representing contribution of the magnet. $\mathbf{J}_{\mathrm{e}}$ and $\mathbf{J}_{\mathrm{pm}}$ are given as follows:

$$\mathbf{J}_{\mathrm{e}} = -\sigma_{\mathrm{pm}} \frac{\partial \mathbf{A}}{\partial t} \tag{6-2}$$

$$\mathbf{J}_{\mathrm{pm}} = \nabla \times \left(\nu_{\mathrm{pm}} \mathbf{B}_{\mathrm{r}}\right) = \nu_{\mathrm{pm}} \left(\frac{\partial B_{\mathrm{r}y}}{\partial x} - \frac{\partial B_{\mathrm{r}x}}{\partial y} \right) \tag{6-3}$$

σ_{pm}, ν_{pm} and $\mathbf{B}_{\mathrm{r}}$ are respectively the conductivity, reluctivity and residual flux density vector of the magnet, and $B_{\mathrm{r}x}$ and $B_{\mathrm{r}y}$ are respectively the x- and y-component of $\mathbf{B}_{\mathrm{r}}$. Substituting (6-2) and (6-3) into (6-1) and writing left-hand side of the equation as derivatives, one obtains

$$\nu_{\mathrm{pm}} \frac{\partial^2 \mathbf{A}}{\partial x^2} + \nu_{\mathrm{pm}} \frac{\partial^2 \mathbf{A}}{\partial y^2} = \sigma_{\mathrm{pm}} \frac{\partial \mathbf{A}}{\partial t} + \nu_{\mathrm{pm}} \left(\frac{\partial B_{\mathrm{r}x}}{\partial y} - \frac{\partial B_{\mathrm{r}y}}{\partial x} \right) \tag{6-4}$$

Applying Galerkin method to (6-4) and the field equations of other regions, one can obtain the global finite element field equation as follows:

$$\nu_{\mathrm{e}} \mathbf{S} \mathbf{A}_{\mathrm{N}} = \frac{\gamma N_{\mathrm{t}}}{N_{\mathrm{c}} \Delta_{\mathrm{cs}}} \mathbf{Q}_{\mathrm{s}} \mathbf{I}_{\mathrm{s}} + \left[-\sigma_{\mathrm{pm}} \mathbf{T}_{\mathrm{pm}} \frac{\mathrm{d}\mathbf{A}_{\mathrm{N}}}{\mathrm{d}t} + \frac{\nu_{\mathrm{pm}}}{2} \left(B_{\mathrm{r}x} \mathbf{D} - B_{\mathrm{r}y} \mathbf{E} \right) \right] \tag{6-5}$$

The first term on the right-hand side of (6-5) is nonzero for only the nodes related to stator winding elements. The term in the square brackets is nonzero for only the nodes related magnet elements. $\mathbf{T}_{\mathrm{pm}}$, $\mathbf{D}$ and $\mathbf{E}$ are constant matrices derived by Galerkin method. As the rotor of this machine has no amortisseur, rotor circuit terms do not present in (6-5). The global equation of the permanent magnet machine is comprised of (6-5) and the stator circuit equation (3-10). These equations are discretized in time domain by C-N method and then solved by NR-DD numerical technique.

Eddy currents in permanent magnets are taken into account in the above field equation, the resulting losses can thereby be calculated using the solution of the equation. The eddy-current loss (in Watts) in a magnet is expressed by the following integral over the cross section of the magnet:

$$P_{\mathrm{pm}} = \iint \frac{L_{\mathrm{pm}}}{\sigma_{\mathrm{pm}}} J_{\mathrm{e}}^{2} \mathrm{d}S \tag{6-6}$$

L_{pm} is the axial length of the magnet. J_{e} is the *z*-component of the eddy current vector, $\mathbf{J}_{\mathrm{e}}$ ($\mathbf{J}_{\mathrm{e}}$ has only *z*-component in a 2-D model). To give a finite element solution to (6-6), J_{e} can be expressed by the nodal magnetic potentials. The eddy-current density in the *i*th element in a magnet is given by

$$J_{\mathrm{e}i}^{t+\Delta t} = -\sigma_{\mathrm{pm}} \frac{\overline{\mathbf{A}}_{\mathrm{e}i}^{t+\Delta t} - \overline{\mathbf{A}}_{\mathrm{e}i}^{t}}{\Delta t} \tag{6-7}$$

where $\overline{\mathbf{A}}_{\mathrm{e}i}$ is average of the three nodal potentials. The magnet's instantaneous eddy-current loss is expressed by finite elements as follows:

$$P_{\mathrm{pm}}^{t+\Delta t} = \frac{L_{\mathrm{pm}}}{\sigma_{\mathrm{pm}}} \sum_{i} J_{\mathrm{e}i}^{2} \Delta_{\mathrm{e}i} = \frac{L_{\mathrm{pm}} \sigma_{\mathrm{pm}}}{\Delta t^{2}} \sum_{i} \Delta_{\mathrm{e}i} \left(\overline{\mathbf{A}}_{\mathrm{e}i}^{t+\Delta t} - \overline{\mathbf{A}}_{\mathrm{e}i}^{t} \right)^{2} \tag{6-8}$$

6.3 Initial design of prototype machine

The application in flywheel system places a number of technical requirements on the PMSM and the drive system. Table 6-1 summarizes the specific characteristics of this flywheel machine system. As the flywheel may be frequently accelerated or decelerated, the PMSM is required to be operated at a wide range of high speeds, and the field weakening control is applied at these high speeds. Due to the difficulty in removing heat from the rotor, permanent magnets with high temperature tolerance are preferred in the flywheel machine. The maximum operating temperature of the chosen magnets is as high as 200˚C. In the stage of raw design, the values of flux linkage and inductance are first roughly

Table 6-1
Specification of a flywheel permanent magnet synchronous machine system

Number of poles	4
Typical operating frequency range	467Hz – 933Hz
Speed range	0rpm – 28000rpm
Typical operating speed range	14000rpm – 28000rpm
Machine average efficiency over the typical speed range	>98% at rated power
System average efficiency including inverter loss	>95%
Total harmonic distortion (THD) of line-line back EMF	<1.32%
Nominal DC link voltage	600V
DC link voltage range	500V – 700V
Nominal maximum continuous power	70kW
30-second overload power rating	120kW

calculated by an analytical lumped-parameter prediction and then verified by static FEA. Once all the parameters regarding dimensions, materials, electric and magnetic circuits, etc are determined in the raw design, the machine performances under different load conditions are simulated using the time-stepped finite element model developed in the previous section and a commercial 2-D FEA package, respectively. In both simulations, it is assumed that the magnets operate at constant temperature of 120˚C with the desired linear magnetization performance. Although the magnet temperature in the real machine system may deviate from the assumed value, the assumption of linear magnetization performance is reasonable in consideration of the strong temperature tolerance of the magnets. In both simulations the machine is assumed driven by a sinusoidal current supply. Provided that the stator currents $\mathbf{I}_s$ and the rotor position are known, one can perform the following steps to simulate a load operation of the PMSM:

1. Find all the nodal magnetic potentials by independently solving (6-5);
2. Substitute these magnetic potentials into (3-10) to calculate the terminal voltages;

3. Calculate the stator Joule loss, iron loss, magnet eddy-current loss and input power using the time-stepped data of stator current, terminal voltage and magnetic potential.
4. Apply the Maxwell stress tensor method [68] to calculate the torque, and subsequently calculate the output power and efficiency.

The above steps can give a full prediction of the load operation performances. The performances predicted by the proposed model are in good agreement with those predicted by the commercial software package. The stage of initial design ends up with minor adjustment to this design that aims to better match the simulated machine performances to the technical requirements. The initial design is mainly other authors' contribution [87]. As this part is not the emphasis of this chapter, details about the process of initial design are omitted here.

The initial design adopts a rotor with the SPM, and double-layer fractional-slot short-pitched distributed windings. The SPM design is more inclined to produce magnet stray loss than an IPM design because the SPM are right located in the air gap, where the slot harmonic flux density can easily diffuse on the surfaces of the magnets. In an IPM machine, the iron laminations that cover the magnets filter part of the slot harmonic fields and hence prevent high stray loss being produced in the magnets. For these reasons, the SPM stray loss is more susceptible to the slot shape than the IPM stray loss. The slot shape optimization for this SPM machine is expected to contribute a significant reduction in the magnet stray loss besides in the total machine loss.

Figure 6-2 shows the finite element mesh for the prototype machine's cross section. The mesh contains 3167 nodes and 5964 first-order triangular elements, not including the dynamic air-gap elements. In consideration of the circumferential periodicity of magnetic field in the fractional-slot machine, the finite element mesh is constructed for a pitch over one pair of poles. Table 6-2 shows the dimension of basic structures in the prototype machine. Table 6-3 presents the lamination parameters.

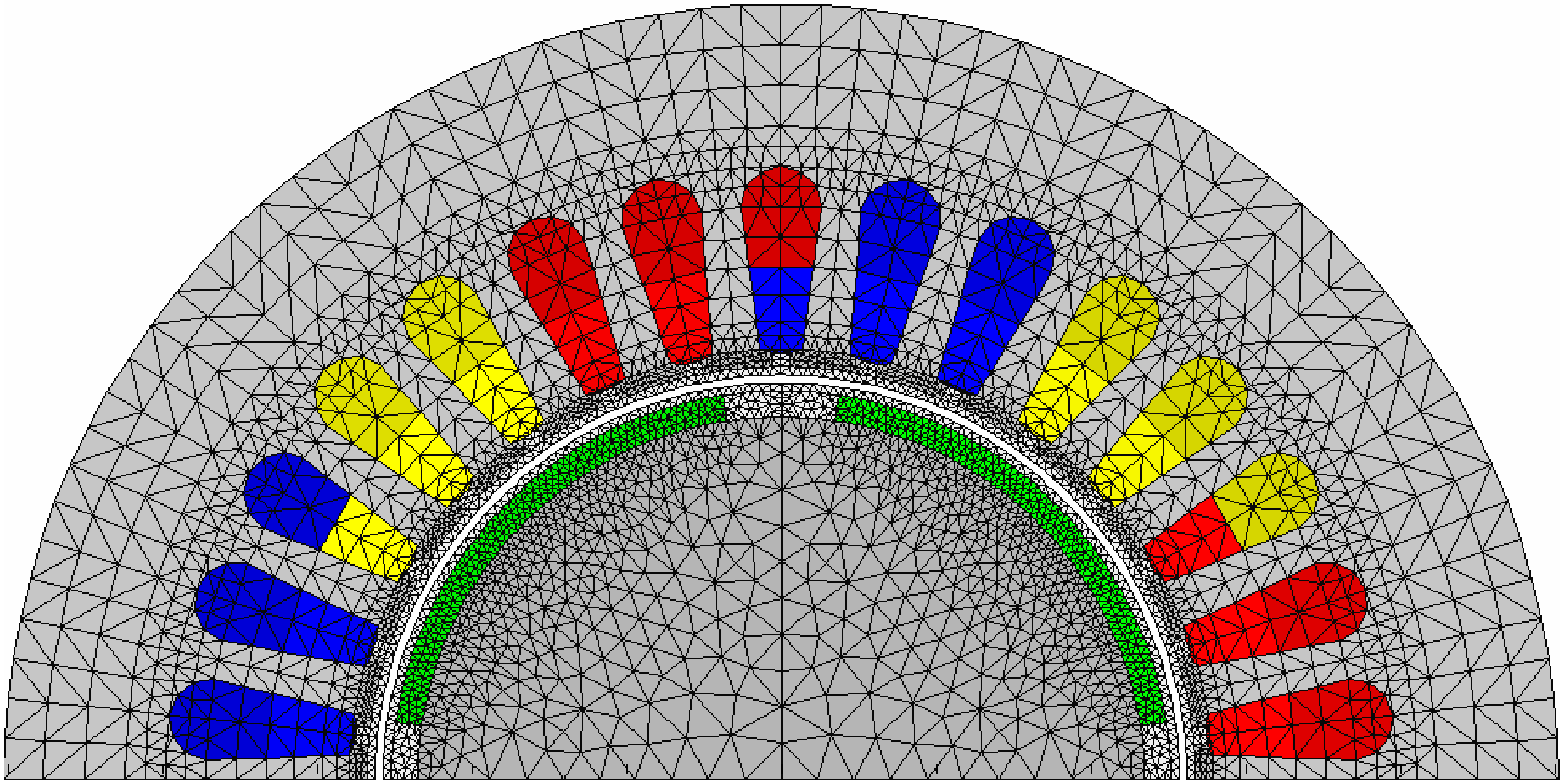

Figure 6-2 Finite element mesh for initial design of a permanent magnet synchronous machine

Table 6-2
Basic structure of the prototype permanent magnet synchronous machine

Core length	0.144m
Outer diameter of stator core	0.229m
Stator slots	2.5slots/phase/pole short pitched by 0.5slots
Rotor core diameter	0.107m
Air gap length (including magnet and overwrap)	7.5mm
Magnet arc	73˚
Magnet thickness	3.88mm

Table 6-3
Stator and rotor lamination parameters of
the prototype permanent magnet synchronous machine

Thickness	0.20mm	α	1.8559
Conductivity	1.818×10^{6}S/m	k_h	0.01743
Mass density	7650kg/m^3	k_e	1.6088×10^{-5}

6.4 Slot shape optimization

6.4.1 Slot shape variables and cost function

The finite element mesh of the stator region in Figure 6-2 is created by duplicating the mesh for half a stator slot pitch, which contains 79 nodes and 116 elements as shown in Figure 6-3 (a). To numerically describe the slot shape, a range of key points on the slot's outline are chosen and 6 decision variables are used to define the relative locations of these nodes as shown in Figure 6-3 (b). Each time when the optimization algorithm reshapes the slot, the values of these variables are changed and this brings about an adjustment of the mesh in Figure 6-3 (a). To avoid a complicated remeshing algorithm that may change the number of nodes and elements, this adjustment is achieved by recalculating the coordinates of existing nodes according to the new values of decision variables.

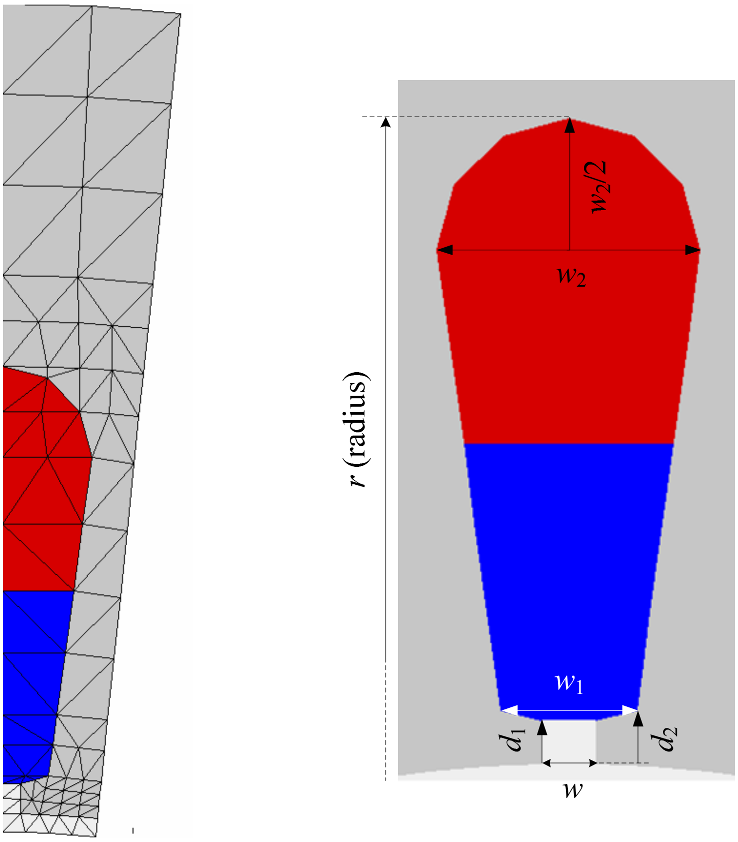

(a) Finite element mesh of half a slot pitch (b) Decision variables

Figure 6-3 Stator slot shape

In order to ensure a reasonable design and a feasible mesh for the slot geometry and, some constraints as shown in Table 6-4 are placed on the individual decision variables, and the combination of these variables is required to satisfy some inequalities. In Table 6-4 the upper for the radius r is chosen to reserve sufficient area of the back iron region; a lower limit for the slot opening w is chosen to allow the enameled wires to pass in the process of assembling stator

Table 6-4
Variable constraints

	w (mm)	d_1 (mm)	d_2 (mm)	w_1 (mm)	w_2 (mm)	r (mm)	A_{st} (mm^2)	L_d, L_q (mH)	Ψ_{pm} (Wb)
Lower limit	1.90	0.30	1.00	2.00	4.00	70.00	206.4	0.275	0.085
Upper limit	4.00	3.00	5.00	8.00	20.00	105.00	--	0.418	0.108

windings. The inequality constraints chosen for the decision variable combination include

$$w_1 \geq w + 1 \text{ (mm)} \tag{6-9}$$

$$d_2 \geq d_1 + 0.4 \text{ (mm)} \tag{6-10}$$

The ES optimizations in this chapter force a decision variable to be the maximum (or minimum) if it violates the corresponding constraint, e.g. $w = 1.9$ if w is found less than 1.9; $w_1 = w + 1$ if w_1 is found less than $w + 1$.

Additional constraints are placed on some dependent variables that are derived as functions (explicit or implicit) of the decision variables. Such variables concerned in this optimization task include A_{st} (slot area), L_d, L_q and Ψ_{pm} (permanent magnet flux linkage). Corresponding to the maximum current density allowed in the slot cross sections, A_{st} must be above the lower limit to ensure sufficient currents in the slots. Constraints are placed on L_d, L_q and Ψ_{pm} to ensure that the field weakening control may be applied efficiently and the DC link voltage is sufficiently high as the machine supply. Qualitative analysis based on well-known d-q axis model of PMSM reveals that inappropriate values of L_d, L_q or Ψ_{pm} may produce unsatisfying value of efficiency or DC link voltage. The d-q axis equations for a PMSM under steady-state operation are given by

$$v_q = R_{\mathrm{s}} i_q + \omega_{\mathrm{e}} \psi_d \tag{6-11}$$

$$v_d = R_{\mathrm{s}} i_d - \omega_{\mathrm{e}} \psi_q \tag{6-12}$$

$$\psi_q = L_q i_q \tag{6-13}$$

$$\psi_d = \psi_{\mathrm{pm}} + L_d i_d \tag{6-14}$$

$$T_{\mathrm{e}} = \frac{3}{2} p \left[\psi_{\mathrm{pm}} i_q + (L_d - L_q) i_d i_q \right] \tag{6-15}$$

where v_d, i_d and Ψ_d are direct axis voltage, current and flux linkage, respectively; v_q, i_q and Ψ_q are quadrature axis voltage, current and flux linkage, respectively; T_{e} is electromagnetic torque. The electromagnetic relations shown in the above equations reveal that

1. Excessively large Ψ_{pm} or excessively small L_d causes additional $|i_d|$ for field weakening and hence decrease in efficiency under the high speed operations;
2. In the case of excessively small Ψ_{pm}, additional i_q is required to compensate for the decrease in torque due to the small Ψ_{pm}, and this also may lead to decrease in efficiency;
3. Excessively large L_q may lead to excessively large Ψ_q and hence a requirement for supply voltage over the limit of DC link voltage.

The constraints on L_d, L_q and Ψ_{pm} are determined according to the machine performances that are roughly predicted using (6-11) to (6-15) under various values of L_d, L_q and Ψ_{pm} and field weakening conditions. These constraints are presented in Table 6-4 together with the constraints for dimension variables. As this PMSM adopts a SPM design with equal L_d and L_q, the constraints on them are identical.

The slot shape optimization is mathematically equivalent to minimization of a cost function. The cost function is constructed by superimposing the penalty functions on the total machine loss:

$$C = W + P_1(A_{\mathrm{st}}) + P_2(L_d) + P_3(\psi_{\mathrm{pm}}) \tag{6-16}$$

In (6-16), W is the total machine loss (in Watts). As the flywheel PMSM would rarely operate at steady speeds, it is impractical to minimize the machine losses under a range of varying load conditions. The machine loss under 28000rpm, open-circuit operation is chosen as a representative object for slot shape optimization. The open-circuit PMSM loss is comprised of the stator and rotor iron loss and the magnet eddy-current loss. After the field distribution information is acquired by FEA, the iron losses can be calculated using the three classical equations (2-3), (2-4) and (2-6); the magnet losses can be calculated using the equation (6-8). In (6-16), the penalty functions P_1, P_2 and P_3 may add positive numbers to the cost function when the dependent variable values violate the constraints. The decision variable constraints are handled outside the cost function. The general form of penalty functions is given by

$$P(x) = \begin{cases} 0, \text{ if } x_\mathrm{l} \le x \le x_\mathrm{u} \\ K_\mathrm{u}(x - x_\mathrm{u}), \text{ if } x > x_\mathrm{u} \\ K_\mathrm{l}(x_\mathrm{l} - x), \text{ if } x < x_\mathrm{l} \end{cases} \tag{6-17}$$

where x_l, x_u are respectively the lower limit and upper limit of the variables, K_l and K_u are positive factors that give "penalty" to the candidates beyond the dependent variable limits. The values of K_l and K_u should be determined before carrying out the optimization algorithm. One may evaluate the machine performances under the variable values beyond the limits, using the *d-q* axis equations (6-11) to (6-15), and determine the values of K_l and K_u according to sensitivity of the performances to the variable values. The values of K_l and K_u used for this optimization task are presented in Table 6-5. Adding penalty values into the cost function may allow some infeasible candidates to survive during a number of optimum-seeking iterations, rather than discard all of them by following a zero tolerance rule. For the case that the optimum occurs close to or right on the boundary of the feasible range, the penalty function approach is more probable to locate the optimum than the zero tolerance approach.

Table 6-5
Penalty weights

	For A_st, per mm^2	For L_d, per mH	For Ψ_pm, per Wb
K_l	10	1000	10000
K_u	0	1000	20000

6.4.2 Evolution strategy review

In an ES algorithm a candidate solution is expressed as a vector of objective variables,

$$\boldsymbol{a} = (\boldsymbol{x}, \boldsymbol{\sigma}, \boldsymbol{\theta}) \tag{6-18}$$

$\boldsymbol{x}$ is a vector of N_dv decision variables. $\boldsymbol{\sigma}$ is a vector of N_dv step size values (i.e. standard deviations), each corresponding to a decision variable. $\boldsymbol{\theta}$ is a vector of $N_\mathrm{dv}(N_\mathrm{dv}-1)/2$ rotation angles, and $\theta_i \in [-\pi, \pi]$. $\boldsymbol{\sigma}$ and $\boldsymbol{\theta}$ are strategy parameters optimized together with the decision variables, and this gives ES a self-adaptive feature. For the sake of completeness, a typical ES algorithm is briefly introduced in this section. A typical ES algorithm performs recombination, mutation and selection in sequence within each generation. Flow chart of the ES algorithm is shown in Figure 6-4.

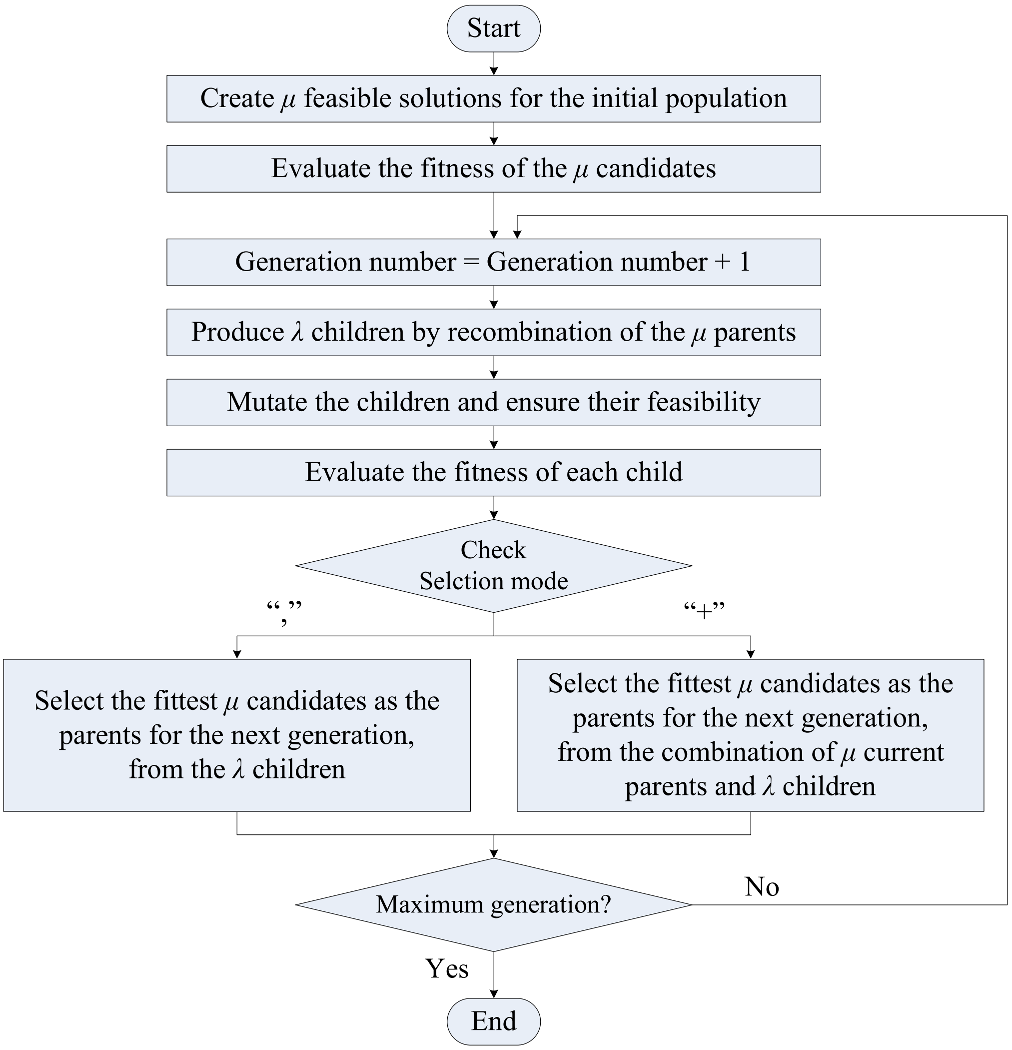

Figure 6-4 Flow chart of a typical evolution strategy

A. Selection

According to the criterion for selection, ES algorithms are classified into two categories: (μ, λ) ES and (μ+λ) ES. λ children are reproduced from μ parents by recombination and mutation within each generation of the ES algorithm. (μ, λ) ES selects the fittest μ out of the λ children to be the parents for the next generation. (μ+λ) ES differs from (μ, λ) ES in that the fittest μ to be the parents for the next generation are selected from the combination of the current μ parents and λ children. The applications of different ES algorithms to AC machine design optimization are found in a number of publications. For example, Chun, Jung and Yoon apply (1+1) ES to slot shape optimization for a permanent magnet motor to minimize the cogging torque [88]; Kim, Lee and Jung apply a modified (1+1) ES to the multiobjective optimal design of a three-phase induction motor [89]; Bochnia, Hofmann and Hupe optimize the design of an outer-rotor permanent magnet motor by (1, 5) ES [90].

B. Recombination

In the ES algorithm, the genes (i.e. components of the vector $\boldsymbol{a}$, including the decision variables and the strategy parameters) of each child are produced by recombination of the genes of two parents. The recombination operator can be sexual or panmictic, and each of them can be discrete or intermediate.

The sexual or panmictic operator is used to determine how the two parents are chosen from the μ individuals. In the sexual form, the two parents of each child are randomly chosen from the μ individuals (choosing the same individual twice for creation of one child is not suppressed though this incest recombination operator can never create anything new), and all the genes of this child are produced by these two parents. For each child produced by panmictic recombination, one parent is first chosen randomly and held fixed, then for each gene of this child the second parent is randomly chosen anew from the parent population. Thus the individual genes of a panmictic variant can be produced from different combinations of parents.

Once the two parents are determined by the sexual or panmictic operator, the discrete or intermediate operator is used to determine the manner in which the genes are inherited from the two parents. In the discrete form, it is decided randomly from which of the two corresponding parents each gene is copied to a child. In the intermediate form, each gene of a child is obtained by calculating the arithmetic mean of the corresponding genes of two parents. The various forms of recombination that create a child $\boldsymbol{a}' = (\boldsymbol{x}', \boldsymbol{\sigma}', \boldsymbol{\theta}')$ from a parent population are summarized here in order to formulate the above recombination operators. The *i*th component of the vector $\boldsymbol{a}'$ is expressed by

$$a'_i = \begin{cases} a_{\mathrm{F},\,i} & \text{no recombination} \\ a_{\mathrm{F},\,i} \text{ or } a_{\mathrm{S},\,i} & \text{sexial discrete} \\ a_{\mathrm{F},\,i} \text{ or } a_{\mathrm{S}i,\,i} & \text{panmictic discrete} \\ \dfrac{(a_{\mathrm{F},\,i} + a_{\mathrm{S},\,i})}{2} & \text{sexial intermediate} \\ \dfrac{(a_{\mathrm{F},\,i} + a_{\mathrm{S}i,\,i})}{2} & \text{panmictic intermediate} \end{cases}$$

where the subscripts F and S denote respectively the first and the second parent individual chosen randomly from the parent population, and the subscript S*i* indicates that the second parent is sampled anew for each value of *i*.

C. Mutation

The λ children produced by the above recombination operations will experience mutations prior to selection of the parents for the next generation. There are two types of mutation operators: uncorrelated and correlated. For ES with uncorrelated mutation, the vector of a candidate solution does not include the rotation angles $\boldsymbol{\theta}$, i.e.

$$\boldsymbol{a} = (\boldsymbol{x}, \boldsymbol{\sigma}) \tag{6-19}$$

The axes of the uncorrelated mutation hyper-ellipsoids (surfaces of equal probability density to place an offspring by mutation) are parallel to the coordinate axes of the search space $\boldsymbol{x}$. The uncorrelated mutation operator is expressed as follows ($i = 1, 2, \ldots, N_{\mathrm{dv}}$):

$$\sigma''_i = \sigma'_i \cdot \exp\left[\tau_1 \cdot N(0,1) + \tau_2 \cdot N_i(0,1)\right] \tag{6-20}$$

$$x''_i = x'_i + \sigma''_i \cdot N_i(0,1) \tag{6-21}$$

In (6-20) and (6-21) the superscript $'$ denotes a child's variables while the superscript $''$ denotes the variables of that child's mutant. τ_1 and τ_2 are interpreted in the sense of "learning rates" as in artificial neural networks. The values of τ_1 and τ_2 suggested by Schwefel [66] are $\tau_1 = \left(\sqrt{2N_{\mathrm{dv}}}\right)^{-1}$, $\tau_2 = \left(\sqrt{2\sqrt{N_{\mathrm{dv}}}}\right)^{-1}$. The notation $N(0, 1)$ denotes a realization of a normally distributed 1-D random variable with the expectation of zero and the standard deviation of one, and that is sampled anew for each mutant. $N_i(0, 1)$ denotes that the random variable is sampled anew for each gene of the mutant as the counter i is being updated.

In the more general case of correlated mutation, the standard deviations still mutate as (6-20) while the rotation angles and the decision variables mutate as (6-22) and (6-23), respectively ($j = 1, 2, \ldots, N_{\mathrm{dv}}(N_{\mathrm{dv}}-1)/2$).

$$\theta''_j = \theta'_j + \chi \cdot N_j(0,1) \tag{6-22}$$

$$\boldsymbol{x}'' = \boldsymbol{x}' + \boldsymbol{N}\left[\mathbf{0}, \mathbf{R}(\boldsymbol{\sigma}'', \boldsymbol{\theta}'')\right] \tag{6-23}$$

The value of χ suggested by Schwefel [66] is $\chi \approx 0.0873$. $\boldsymbol{N}\left[\mathbf{0}, \mathbf{R}(\boldsymbol{\sigma}'', \boldsymbol{\theta}'')\right]$ denotes a realization of a random vector that complies with the generalized N_{dv}-dimensional normal distribution with the expectation of $\mathbf{0}$ and the covariance matrix of $\mathbf{R}^{-1}(\boldsymbol{\sigma}'', \boldsymbol{\theta}'')$. Details about how to find a realization of that random vector are omitted here, and they can be found in a number of textbooks, e.g. [91]. The correlated mutation allows the mutation hyper-ellipsoids to have any orientation by rotating them with a rotation (covariance) matrix $\mathbf{R}^{-1}$. In this way the ES algorithm with correlated mutation can adapt itself to any advantageous direction of search, nevertheless it implies extra computational effort and memory space for the covariance matrix.

The above mutation algorithm may produce an infeasible candidate with decision variables that violate their constraints. To ensure the feasibility of a candidate, the mutation algorithm may discard such a candidate and repeat itself until a feasible candidate is found, or directly limit the candidate onto the constraint boundary.

6.4.3 Optimization by (1, 4) and (1+4) evolution strategies

Previous authors' experiences show that the ES algorithms such as (1+1) ES [88], [89] and (1, 5) ES [90] are competent enough for a variety of AC machine optimization tasks, an algorithm with large population seems unnecessary for the optimization task in this chapter that has only 6 objective variables. (1, 4) ES and (1+4) ES with uncorrelated mutation are applied respectively to the slot shape design optimization. Recombination is skipped over in these algorithms as the 4 offspring are born to only one parent. As mentioned in Section 6.4.1, for this optimization task the ES mutation deals with a candidate with any infeasible decision variable by limiting it onto the constraint boundary, rather than repeating the algorithm until a candidate with feasible decision variables is obtained. On the other hand, the dependent variable constraints are handled by adding penalty functions into the cost function as shown in (6-16). Finite element simulations are carried out for evaluation of the candidate solutions' fitness. Static FEA is first implemented to calculate L_d (or L_q) and Ψ_{pm}, and then the open-circuit performances over one cycle at the speed of 28000rpm are simulated by time-stepped FEA to calculate the iron loss and the magnet stray loss. Similarly to the iron loss evaluation for synchronous machines, for a PMSM, the stator iron loss is evaluated from the aspects of hysteresis loss, eddy-current loss and excess loss while the rotor iron loss evaluation neglects the minor hysteresis loop. In the (1, 4) ES and (1+4) ES algorithms, the fitness evaluation, mutation and mesh adjustment for the 4 offspring are independent of each other, so that these steps can be carried out in parallel on 4 processors. The finite element simulation for the unskewed PMSM investigated in this chapter utilizes a single-slice model, parallel processing is therefore not implemented on the level of machine model. Flow chart of the parallelized (1, 4) ES and (1+4) ES algorithms is shown in Figure 6-5. These ES algorithms are efficiently carried out on a quad-core computer, saving significant time in the FEA for fitness evaluation.

The loss minimization algorithms based on (1, 4) ES and (1+4) ES start with the same initial values of objective variables. The results of initial design and optimized designs given by the two algorithms are presented in Table 6-6. Due to the design with a long air gap, the magnitude of slot harmonics in the rotor core flux density is so low that it produces little harmonic stray loss in the rotor iron. In this case, stator iron loss and magnet stray loss are the main loss components that noticeably response to the adjustment of slot shape. Both the (1, 4) and (1+4) ES algorithms give the slots that are fundamentally thinner and shorter than the initial design, reducing the total loss by 12.7% and 11.8%, respectively. The data in Table 6-6 show that the ES designs produce a similar effect of loss density

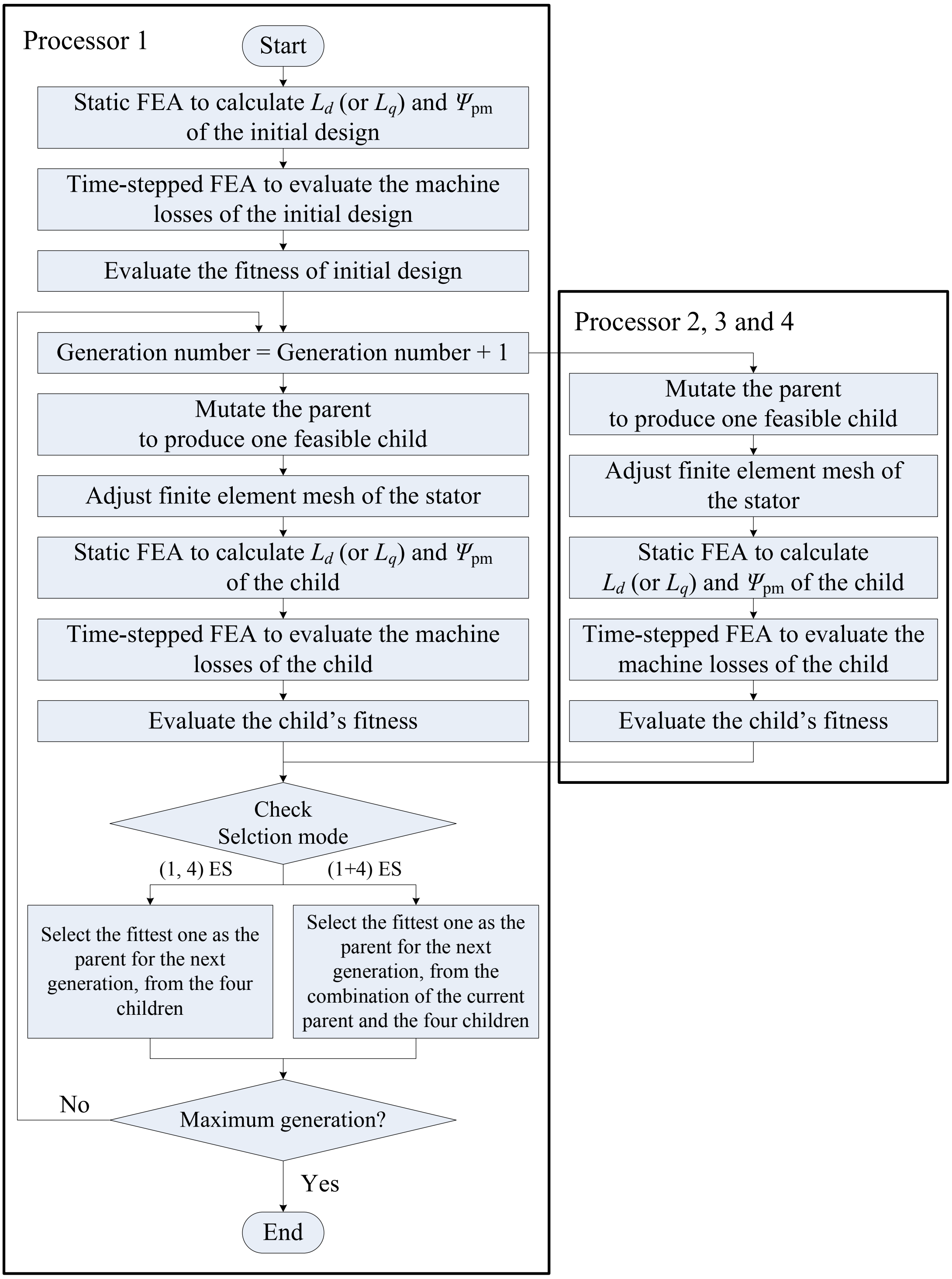

Figure 6-5 Flow chart of slot optimization by parallel (1, 4) ES and (1+4) ES

reduction in the regions of teeth and back iron. In comparison to the initial and (1+4)-ES designs, the (1, 4)-ES design creates narrower slot openings and a more

Table 6-6
Initial design and optimization results of slot shape

Shape and performance variables	Initial design	(1, 4) ES	(1+4) ES
w (mm)	2.44	1.94	2.22
d_1 (mm)	2.00	0.90	1.31
d_2 (mm)	2.49	3.97	2.47
w_1 (mm)	6.20	4.88	6.72
w_2 (mm)	12.00	11.93	10.55
r (mm)	90.58	89.89	87.41
A_{st} (mm^2)	248.05	206.40	208.10
Fill factor	0.373	0.447	0.444
L_d, L_q (mH)	0.310	0.319	0.305
Ψ_{pm} (Wb)	0.102	0.103	0.103
Cost function value	756.86	660.55	667.22
Total machine loss (W)	756.86	660.55	667.22
Total iron loss (W)	707.49	639.64	633.89
Stator iron loss (W)	707.45	639.62	633.85
Rotor iron loss (W)	0.04	0.02	0.03
Magnet stray loss (W)	49.37	20.91	33.33
Average loss density in tips (kW/m^3)	265.72	213.32	310.34
Average loss density in teeth (kW/m^3)	373.54	347.60	348.20
Average loss density in back iron (kW/m^3)	166.92	142.17	136.70

smooth tip-tooth transition by a better combination of w, d_1, d_2 and w_1 values. It can be seen that the initial slot area is relatively large with a fill factor less than 0.4 if an appropriate wire gauge such as Gauge 15 or Gauge 18 is chosen. Provided that the same wire is applied into the slots given by the (1, 4)-ES and (1+4)-ES designs, the fill factors of both designs are increased to slightly under 0.45. This still admits sufficient wires within the reduced slot area. As the results of the decrease in air-gap flux density fluctuations, this design significantly reduces the average loss density in the tip regions and the permanent magnets. The most important advantage of the (1, 4)-ES design is that the percentage of decrease in magnet stray loss (compared to the initial design) is as high as 57.6%. This design can significantly reduce the risk of degrading and demagnetizing the permanent magnet in an evacuated flywheel enclosure. Figure 6-6 shows the loss density distribution of the initial design, (1, 4)-ES design and (1+4)-ES design. Due to the concentration of high-frequency harmonic flux densities on the magnets' surface, the eddy-current loss density on the surface is obviously higher than those in the inner region.

The results in Table 6-6 indicate that the (1+4)-ES algorithm does not give the optimal design. The progress of the cost function during the ES generations is shown in Figure 6-7. In the (1+4)-ES optimization, the cost function value has been fast decreasing to a local minimum within the first 5 generations, however does not get any chance to escape from this local minimum thereafter. Conversely, the (1, 4)-ES algorithm presents a sequence of cost function values that are not monotonically decreasing (a result larger than the initial value even occurs at the 9th generation), however it eventually converges to a better design. This phenomenon can be explained by comparing the selection mode of the two algorithms. With the (1+4) ES any offspring inferior to its parent will not survive for the next generation, therefore this algorithm may escape from a local optimum only if it reproduces by chance a mutant which is out of the close neighborhood of the local optimum and superior to its parent. With the (1, 4) ES an offspring inferior to its parent still has the opportunity to survive for more than one generation, this may allow the candidate to jump out of the close neighborhood of a local optimum and eventually help the algorithm converge to the global optimum.

6.5 Summary

This chapter investigates the shape of slots as a factor affecting the loss density distribution in an AC machine. Optimization of stator slot shape is implemented for a flywheel PMSM to minimize the total machine loss. The

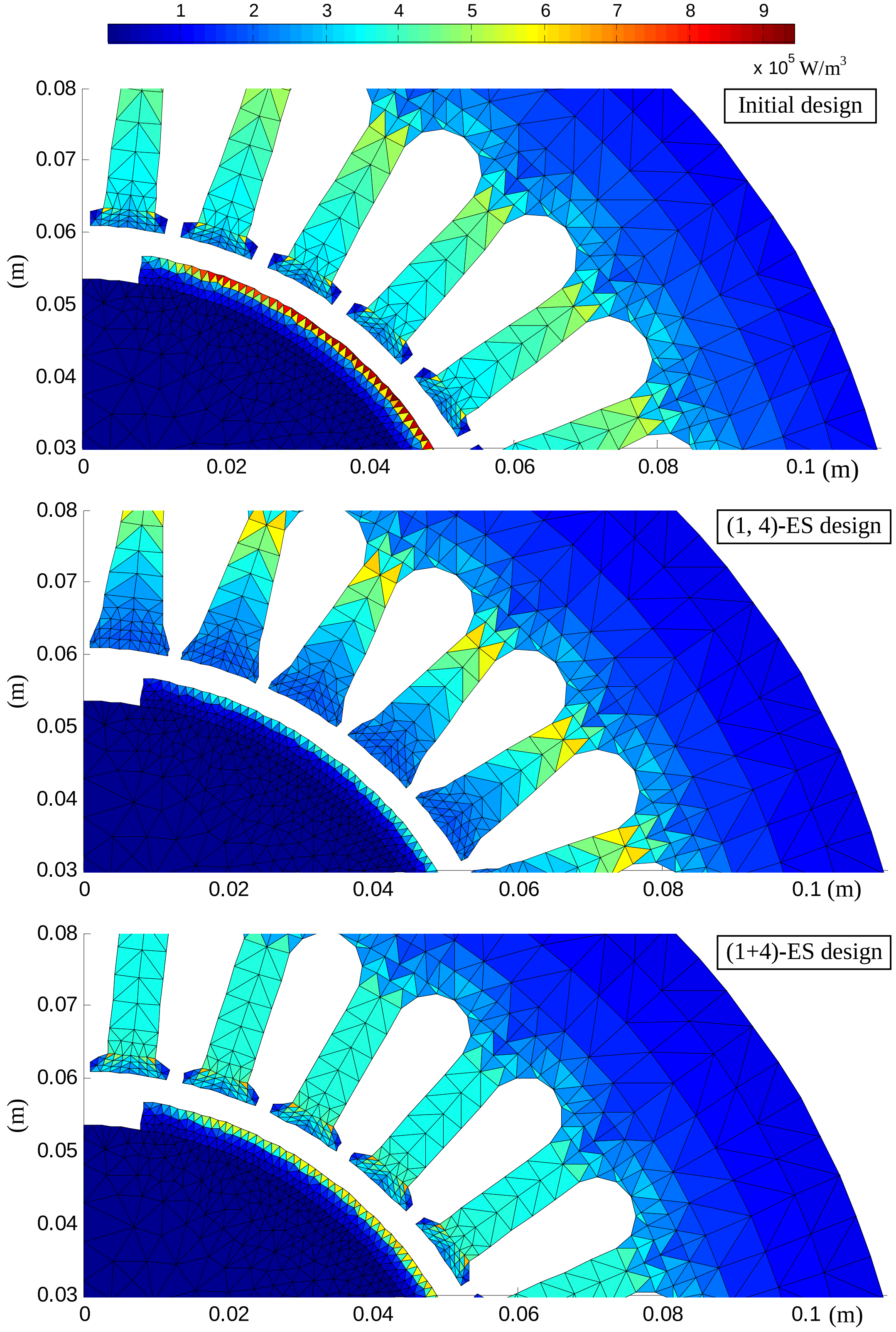

Figure 6-6 Loss density in permanent magnet synchronous machines

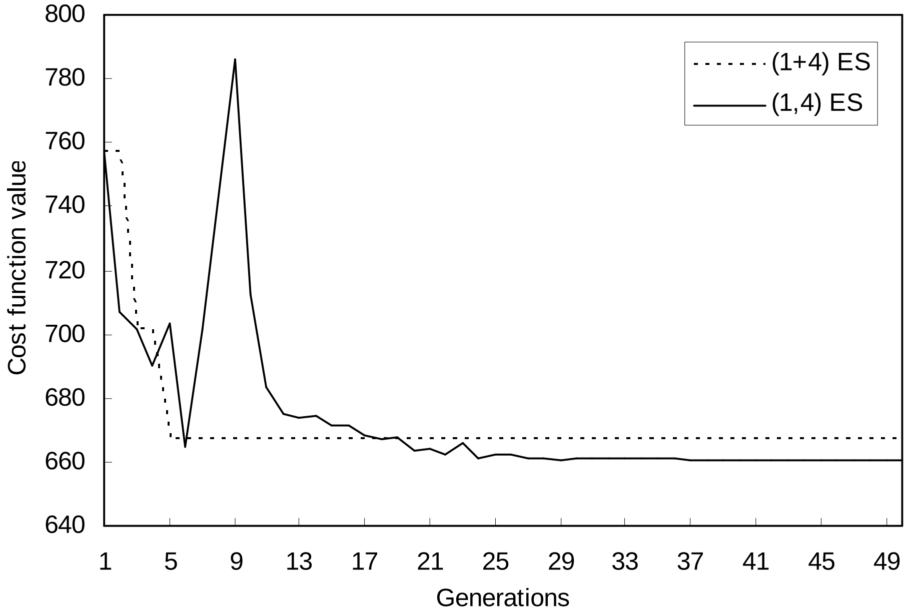

Figure 6-7 Cost function values

optimization adjusts 6 decision variables that are chosen to sketch out the slot shape. A cost function (objective function for optimization) is defined as the sum of total machine loss and penalty functions that account for the design constraints on the parameters such as slot area, *d*- and *q*- axis inductances and permanent magnet flux linkage. In the process of optimization, static 2-D FEA is carried out to calculate those constrained parameters while time-stepped 2-D FEA is carried out to evaluate the PMSM losses including the magnet stray loss that is a component very sensitive to the shape of stator slots.

Parallelized (1, 4) ES and (1+4) ES are implemented respectively as optimization algorithms for the slot shape design improvement. These parallelized algorithms are suitable to be executed on a quad-core computer, which is popular nowadays in design offices. The parallel execution can significantly save the time consumed in FEA that is used to evaluate the children's fitness. The (1, 4) ES gives an optimization result superior to that given by the (1+4) ES. The slot-tooth design given by the (1, 4) ES appears with thinner and shorter slots and smooth tip-tooth transition. This new design significantly reduces the total machine loss as well as the magnet stray loss. The decrease in the total loss can help improve the round-trip efficiency of the flywheel PMSM. On the other hand, the decrease in the magnet stray loss is significantly beneficial as it can strengthen reliability of the permanent magnets in the evacuated flywheel chamber.

Chapter 7 Conclusions and Future Work

7.1 Conclusions

Time-stepped 2-D finite element models are constructed for various AC machines in order to investigate the stray losses in these machines. Multislice technique, interbar circuit model and Carter's effective core length are incorporated with the traditional 2-D finite element model to account for the axial variations in the electromagnetic field that are caused by the presence of skewed stator or rotor, imperfect bar-bar insulation and radial ventilation ducts.

The AC machine simulations based on the multislice interbar model are very expensive computationally. In order to improve the computational efficiency of the multislice interbar model, the serial and parallel NR-DD numerical techniques are developed respectively to solve the system equation of a skewed induction motor. The motor performances at a range of interbar resistances and rotor temperatures are simulated, and the simulation results are validated by test results. For a 5-slice simulation, the serial NR-DD technique reduces the simulation time to less than 70% in comparison to the traditional NR technique while the parallel NR-DD technique further reduces the simulation time to less than 20%. The efficient simulation technique is used to investigate some aspects of stray losses in induction machine, synchronous machine and PMSM.

Simulations and tests are carried out for an induction motor under sinusoidal and SPWM supply to investigate the harmonic stray loss caused by PWM supply. As expected, the simulation and test results suggest additional losses under a PWM supply relative to the case of sinusoidal supply. Of the two components in these additional losses, the component of harmonic stray loss is less significant than the fundamental loss component. As an induction machine becomes more saturated with the increasing load, the weight of fundamental loss in this additional loss becomes even more significant than in the case of a lower saturation level. These results of stray loss investigation indicate that a thermal design improvement may be more beneficial to induction motor efficiency than an improvement of PWM switching patterns.

The investigation in this thesis reveals that the rotor interbar leakage current is an important source of harmonic stray loss in AC machines. Simulations and tests are carried out on a large synchronous generator to study the impact of interbar resistance on the harmonic fields and harmonic stray losses in this generator. The simulation results indicate that the slot harmonics and the resulting stray losses in the amortisseur cage are susceptible to the variation in interbar resistance. Within a certain range of interbar resistance, the cage stray loss may account for a significant proportion of the total rotor loss. The data and curves obtained from the simulations can better inform the rotor manufacturing improvement that aims to mitigate the harmonic stray loss in amortisseur by appropriate interbar insulation.

The slot shape is investigated in this thesis as another factor affecting the total loss and the slot harmonic stray loss in AC machines. ES is applied as a formal optimization algorithm to the improvement of slot shape design in order to minimize the total loss in a flywheel PMSM. The magnet stray loss that is caused by the slot harmonics is taken into account in the task of loss minimization. The parallelized (1, 4) ES gives a design of slot shape that reduces the total machine loss by 12.7% and the magnet stray loss by 57.6%. An attractive advantage of this design is the significant reduction in magnet stray loss that conduces to a safe range of operating temperature for the permanent magnets.

7.2 Recommendations for future work

There are some areas worthy of further investigation as research topics subsequent to the results presented in this thesis. Recommendations for the future work focus on the improvement of modeling techniques for AC machines.

This thesis assumes that iron laminations possess a monotonic magnetization characteristic, the effect of minor hysteresis loops in the *B-H* curve are not taken into consideration. The losses caused by minor hysteresis loops, though usually assumed very small, should be taken into account when making a detailed comparison of the harmonic stray losses under different PWM switching patterns. An improvement of the minor hysteresis loop modeling may help to distinguish the harmonic stray losses under various PWM schemes such as SPWM, space vector PWM (SVPWM), discontinuous PWM (DPWM), etc, and under the different combinations of amplitude modulation index and DC link voltage.

The modeling improvement for thick iron laminations is another recommendation for the further work. “Thick” means that the sheet’s thickness along the machine axis is comparable to or greater than the skin depth. In this case, the flux density and the eddy current density both decay from the surface to the center of a conductor sheet, rather than uniformly distributed as assumed in this thesis. The skin depth turns smaller as the saturation level of a machine field turns lower. As a function of saturation level, skin effect should be included in a machine loss evaluation model for those iron laminations that are “thicker” relative to the skin depth.

The AC machine model in this thesis requires the rotor temperature as an input to the simulation system. A thermal equation coupled to the AC machine simulation system is recommended to correct the parameter of rotor resistance and improve the accuracy of rotor loss prediction.

Bibliography

[1] R. Hanitsch, “Energy efficient electric motors”, *Proceedings of RIO 02 – World Climate & Energy Event*, January 6-11 2002, pp. 45 - 50

[2] A.A. Jimoh, R.D. Findlay and M. Poloujadoff, “Stray losses in induction machines: Part I, Definition, origin and measurement”, *IEEE Transactions on Power Apparatus and Systems*, vol. PAS-104, no.6, June 1985, pp. 1500-1505

[3] H.C. Karmaker, “Stray losses in large synchronous machines”, *IEEE Transactions on Energy Conversion*, vol. 7, no. 1, March 1992, pp. 148-153

[4] IEEE standard test procedure for polyphase induction motors and generators, IEEE Standard 112-2004, November 2004

[5] IEEE guide: Test procedures for synchronous machines, IEEE Standard 115-1995, December 1995

[6] Rotating electrical machines - Part 2-1: Standard methods for determining losses and efficiency from tests (excluding machines for traction vehicles), IEC 60034-2-1, September 2007

[7] S. Williamson and A.C. Smith, “Influence of interbar currents on the harmonic losses and skew in cage induction machines”, *International Conference on Power Electronic, Machines and Drives*, June 4-7 2002, Conference Publication no.487, pp. 369-374

[8] B. J. Chalmers and A. C. Williamson, “Stray losses in squirrel-cage induction motors,” *IEE Proceedings*, vol. 110, no. 10, 1963, pp. 1773–1778

[9] E. Levi, *Polyphase motors*: *a direct approach to their design*, John Wiley & Sons, New York, 1984

[10] C.N. Glew, “Stray load losses in induction motors: a challenge to academia”, *Power Engineering Journal*, vol. 12, no. 1, February 1998, pp. 27-32

[11] H. Auinger, “Determination and designation of the efficiency of electrical machines”, *Power Engineering Journal*, vol. 13, no. 1, February 1999, pp. 15-23

[12] W. Cao, K. J. Bradley and J. Allen, “Evaluation of additional loss in induction motors consequent upon repair and rewinding”, *IEE Proceedings Electric Power Applications*, vol. 153, no. 1, January 2006, pp. 1-6

[13] H.A. Toliyat and G.B. Kliman, *Handbook of electric motors*, CRC Press, 2004

[14] B. Brunelli, D. Casadei, U. Reggiani and G. Serra, “Transient and steady-state behaviour of solid rotor induction machines”, *IEEE Transactions on Magnetics*, vol. 19, no. 6, November 1983, pp. 2650-2654

[15] E.G. Strangas and K.R. Theis, “Shaded pole motor design and evaluation using coupled field and circuit equations”, *IEEE Transactions on Magnetics*, vol. 21, no. 5, September 1985, pp. 1880-1882

[16] T.W. Preston, A.B.J. Reece and P.S. Sangha, “Induction motor analysis by time-stepping techniques”, *IEEE Transactions on Magnetics*, vol. 24, no. 1, January 1988, pp. 471-474

[17] A. Arkkio, “Finite element analysis of cage induction motors fed by static frequency converters”, *IEEE Transactions on Magnetics*, vol. 26, no. 2, March 1990, pp. 551-554

[18] P. Zhou, M.A. Rahman and M.A. Jabbar, “Field circuit analysis of permanent magnet synchronous motors”, *IEEE Transactions on Magnetics*, vol. 30, no. 4, July 1994, pp. 1350-1359

[19] S. Williamson and A.F. Volschenk, “Time-stepping finite element analysis for a synchronous generator feeding a rectifier load”, *IEE Proceedings Electric Power Applications*, vol. 142, no. 1, January 1995, pp. 50-56

[20] R. Carlson, N. Sadowski, S.R. Arruda, C.A. Da Silva and L. Von Dokonal, “Single-phase line-started permanent magnet motor analysis using finite element method”, *Industry Applications Society Annual Meeting*, October 2-6 1994, Conference Record of the 1994 IEEE, vol.1, pp. 227-233

[21] S.L. Ho and H.L. Li, “Dynamic modeling of permanent magnet synchronous machines using direct-coupled time stepping finite element method”, *IEEE International Electric Machines and Drives Conference, IEMDC’99*, May 9-12 1999, pp. 113-115

[22] S. Williamson, L.H. Lim and A.C. Smith, “Transient analysis of cage-induction motors using finite-elements”, *IEEE Transactions on Magnetics*, vol. 26, no. 2, March 1990, pp. 941-944

[23] A. Arkkio, “Analysis of induction motors based on the numerical solution of the magnetic field and circuit equations”, *Acta Polytechnica Scandinavica, Electrical Engineering Series No. 59*, December 1987

[24] C.I. McClay and G.T. van der Toorn, “A comparison of time-stepped finite-element techniques for the calculation of losses in cage induction motors”, *9th International Conference on Electrical Machines and Drives*, September 1-3 1999, Conference Publication No. 468, pp. 35-39

[25] A.M. Knight and J.C. Salmon, “A comparison between finite element techniques when modelling single phase line-start permanent magnet motors”, *9th International Conference on Electrical Machines and Drives*, September 1-3 1999, Conference Publication No. 468, pp. 351-355

[26] S. Williamson, T.J. Flack and A.F. Volschenk, “Representation of skew in time-stepped two-dimensional finite element models of electrical machines”, *IEEE Transactions on Industry Applications*, vol. 31, no. 5, September-October 1995, pp. 1009-1015

[27] A. Tenhunen and A Arkkio, “Modelling of induction machines with skewed rotor slots”, *IEE Proceedings Electric Power Applications*, vol. 148, no. 1, January 2001, pp. 45-50

[28] S.L. Ho, W.N. Fu and H.C. Wong, “Estimation of stray losses of skewed rotor induction motors using coupled 2-D and 3-D time stepping finite element methods”, *IEEE Transactions on Magnetics*, vol. 34, no. 5, Part 1, September 1998, pp. 3102-3105

[29] K. Yamazaki and Y. Watanabe, “Interbar current analysis of induction motors using 3-D finite-element method considering lamination of rotor core”, *IEEE Transactions on Magnetics*, vol. 42, no. 4, April 2006, pp. 1287-1290

[30] S.L. Ho, H.L. Li and W.N. Fu, “Inclusion of interbar currents in a network-field coupled time-stepping finite-element model of skewed-rotor induction motors”, *IEEE Transactions on Magnetics*, vol. 35, no. 5, September 1999, pp. 4218-4225

[31] R. Carlson, C.A. da Silva, N. Sadowski, Y. Lefevre and M. Lajoie-Mazenc, “Analysis of the effect of inter-bar currents on the performance of polyphase cage-induction motors”, *IEEE Transactions on Industry Applications*, vol. 39, no. 6, November-December 2003, pp. 1674-1680

[32] L. Serrano-Iribarnegaray and J. Martinez-Roman, “Critical review of the analytical approaches accounting for interbar currents and experimental study of ageing in two-speed asynchronous motors for elevator drives”, *IEE Proceedings Electric Power Applications*, vol. 152, no. 1, January 2005, pp. 72-80

[33] S. Williamson and C.Y. Poh, “Inter-bar currents in cage induction motors”, *IEE Proceedings Electric Power Applications*, vol. 152, no.5, September 9 2005, pp. 1106-1112

[34] D.G. Dorrell, P.J. Holik, P. Lombard, H.-J. Thougaard and F. Jensen, “A multisliced finite-element model for induction machines incorporating interbar current”, *IEEE Transactions on Industry Applications*, vol. 45, no. 1, January-February 2009, pp. 131-141

[35] S. Williamson, C.Y. Poh and A.C.S. Smith, “Estimation of the inter-bar resistance of a cast cage rotor”, *IEEE Transactions on Industry Applications*, vol. 40, no. 2, March-April 2004, pp. 558-564

[36] D. Gersh, A.C. Smith and A. Samuelson, “Measurement of inter-bar resistance in cage motors”, *8th International Conference on Electrical Machines and Drives*, September 1-3 1997, Conference Publication No. 444 , pp. 253-257

[37] D.G. Dorrell, P.J. Holik and C.B. Rasmussen, “Analysis and effects of inter-bar current and skew on a long skewed-rotor induction motor for pump applications”, *IEEE Transactions on Magnetics*, vol. 43, no. 6, June 2007, pp. 2534-2536

[38] S. Williamson and C.Y. Poh, “The effect of interbar currents in a permanent split capacitor motor”, *IEEE Transactions on Industry Applications*, vol. 42, no. 2, March-April 2006, pp. 423-428

[39] J. Lobry, J. Trecat, and C. Broche, “The transmission line modeling (TLM) method as a new iterative technique in nonlinear 2-D magnetostatics”, *IEEE Transactions on Magnetics*, vol. 32, no. 2, March 1996, pp. 559-566

[40] O. Deblecker, J. Lobry and C. Broche, “Use of transmission-line modeling method in FEM for solution of nonlinear eddy-current problems”, *IEE Proceedings Science, Measurement and Technology*, vol. 145, no. 1, January 1998, pp. 31-38

[41] A.M. Knight, “Efficient parallel solution of time-stepped multislice eddy-current induction motor models”, *IEEE Transactions on Magnetics*, vol. 40, no. 2, March 2004, pp. 1282-1285

[42] V.C. Silva, G. Meunier and A. Foggia, “A 3D finite-element computation of eddy currents and losses in the stator end laminations of large synchronous machines”, *IEEE Transactions on Magnetics*, vol. 32, no. 3, Part 1, May 1996, pp. 1569-1572

[43] L.R. Dupre, J.J. Gyselinck and J.A. Melkebeek, “Complementary finite element methods in 2D magnetics taking into account a vector Preisach model”, *IEEE Transactions on Magnetics*, vol. 34, no. 5, Part 1, September 1998, pp. 3048-3051

[44] L.-L. Rouve, F. Ossart, T. Waeckerle and A. Kedous-Lebouc, “Magnetic flux and losses computation in electrical laminations”, *IEEE Transactions on Magnetics*, vol. 32, no. 5, Part 1, September 1996, pp. 4219-4221

[45] L.R. Dupre, R. Van Keer and J.A.A. Melkebeek, “An iron loss model for electrical machines using the Preisach theory”, *IEEE Transactions on Magnetics*, vol. 33, no. 5, Part 2, September 1997, pp. 4158-4160

[46] J.J.C. Gyselinck, L.R.L. Dupre, L. Vandevelde and J.A.A. Melkebeek, “Calculation of no-load induction motor core losses using the rate-dependent Preisach model”, *IEEE Transactions on Magnetics*, vol. 34, no. 6, November 1998, pp. 3876-3881

[47] J. Saitz, “Computation of core loss in an induction motor using the vector Preisach hysteresis model incorporated in finite element analysis”, *IEEE Transactions on Magnetics*, vol. 36, no. 4, Part 1, July 2000, pp. 769-773

[48] J.H. Lee, “Design solutions to minimize iron core loss in synchronous reluctance motor using Preisach model and FEM”, *IEEE Transactions on Magnetics*, vol. 38, no. 5, Part 1, September 2002, pp. 3276-3278

[49] A. Mansouri, H. Trabelsi and M.H. Gmiden, “Calculation of magnetic fields and iron losses in a SMPM by using vector Preisach model and transient finite element analysis”, *5th International Multi-Conference on System, Signals and Devices, IEEE SSD 2008*, July 20-22 2008, pp. 1-7

[50] J.J.C. Gyselinck, L. Vandevelde, D. Makaveev and J.A.A. Melkebeek, “Calculation of no load losses in an induction motor using an inverse vector Preisach model and an eddy current loss model”, *IEEE Transactions on Magnetics*, vol. 36, no. 4, Part 1, July 2000, pp. 856-860

[51] K. Atallah, Z.Q. Zhu and D. Howe, “An improved method for predicting iron losses in brushless permanent magnet DC drives”, *IEEE Transactions on Magnetics*, vol. 28, no. 5, September 1992, pp. 2997-2999

[52] J.D. Lavers, P.P. Biringer and H. Hollitscher, “A simple method of estimating the minor loop hysteresis loss in thin laminations”, *IEEE Transactions on Magnetics*, vol. 14, no. 5, September 1978, pp. 386-388

[53] R. Fei, E.F. Fuchs and H. Huang, “Comparison of two optimization techniques as applied to three-phase induction motor design”, *IEEE Transaction on Energy Conversion*, vol. 4, no. 4, December 1989, pp. 651-660

[54] J.L. Besnerais, V. Lanfranchi, M. Hecquet and P. Brochet, “Multiobjective optimization of induction machines including mixed variables and noise minimization”, *IEEE Transactions on Magnetics*, vol. 44, no. 6, June 2008, pp. 1102-1105

[55] G. Cvetkovski and L. Petkovska, “Efficiency maximisation in structural design optimisation of permanent magnet synchronous motor”, *18th International Conference on Electrical Machines, ICEM 2008*, September 6-9, 2008, pp. 1-6

[56] J.L. Hippolyte, C. Espanet, D. Chamagne, C. Bloch and P. Chatonnay, “Permanent magnet motor multiobjective optimization using multiple runs of an evolutionary algorithm”, *IEEE Vehicle Power and Propulsion Conference, VPPC '08,* September 3-5, 2008, pp. 1-5

[57] C.-C. Hwang, L.-Y. Lyu, C.-T. Liu and P.-L. Li, “Optimal design of an SPM motor using genetic algorithms and Taguchi method”, *IEEE Transactions on Magnetics*, vol. 44, no. 11, November 2008, pp. 4325-4328

[58] D.-J. Sim, D.-H. Cho, J.-S. Chun, H.-K. Jung and T.-K. Chung, “Efficiency optimization of interior permanent magnet synchronous motor using genetic algorithms”, *IEEE Transactions on Magnetics*, vol. 33, no. 2, March 1997, pp. 1880-1883

[59] D.-H. Cho, H.-K. Jung and D.-J. Sim, “Multiobjective optimal design of interior permanent magnet synchronous motors considering improved core loss formula”, *IEEE Transaction on Energy Conversion*, vol. 14, no. 4, December 1999, pp. 1347-1352

[60] S. Park, H. Lee, S. Hahn and I. Park, “Stator slot shape design of induction motors for iron loss reduction,” *IEEE Transactions on Magnetics*, vol. 31, no. 3, May 1995, pp. 2004-2007

[61] S. Williamson and C.I. McClay, “Optimization of the geometry of closed rotor slots for cage induction motors”, *IEEE Transactions on Industry Applications*, vol. 32, no. 3, May-June 1996, pp. 560-568

[62] J. Nocedal and S.J. Wright, *Numerical optimization*, Springer, New York, 2006

[63] A.A. Zhigljavsky, *Theory of global random search*, Kluwer Academic, 1991

[64] S. Kirkpatrick, C.D. Gelatt and M.P. Vecchi, “Optimization by simulated annealing”, *Science*, vol. 220, no, 4598, May 13 1983

[65] A. Fraser and D. Burnell, *Computer models in genetics*, McGraw-Hill, New York, 1970

[66] H.-P. Schwefel, *Evolution and optimum seeking*, John Wiley & Sons, New York, 1995

[67] W. Annicchiarico, J. Periaux, M. Cerrolaza and G. Winter, *Evolutionary algorithms and intelligent tools in engineering optimization*, WIT Press, Billerica, Massachusetts, 2005

[68] S.J. Salon, *Finite element analysis of electrical machines*, Kluwer Academic, 1995

[69] A. Boglietti, A. Cavagnino, A.M. Knight, and Y. Zhan, "Factors affecting losses in induction motors with non-sinusoidal supply", *Industry Applications Society Annual Meeting*, September 23-27 2007, Conference record of the 2007 IEEE, pp. 1193-1199

[70] G. Bertotti, A. Boglietti, M. Chiampi, D. Chiarabaglio, F. Fiorillo and M. Lazzari, "An improved estimation of iron losses in rotating electrical machines" *IEEE Transactions on Magnetics*, vol. 27, no. 6, November 1991, pp. 5007-5009

[71] J. Sagarduy, A.J. Moses and F.J. Anayi, "Effect of AC-AC conversion topology on separation of losses in Si-Re steel", *10th Joint MMM-Intermag Conference*, January 2007, Paper DP-07

[72] T.L. Mthombeni and P. Pillay, "Lamination core losses in motors with nonsinusoidal excitation with particular reference to PWM and SRM excitation waveforms", *IEEE Transactions on Energy Conversion*, vol.20 ,no. 4, December 2005, pp. 836-843

[73] J.F. Bangura and N.A. Demerdash, "Simulation of inverter-fed induction motor drives with pulse-width modulation by a time-stepping coupled finite element-flux linkage-based state space model", *IEEE Transactions on Energy Conversion*, vol. 14, no. 3, September 1999, pp. 518-525

[74] J.-J. Lee, Y.-K. Kim, H. Nam, K.-H. Ha, J.-P. Hong and D.-H. Hwang, "Loss distribution of three-phase induction motor fed by pulsewidth-modulated inverter", *IEEE Transactions on Magnetics*, vol. 40, no. 2, March 2004, pp. 762-765

[75] A. Boglietti, P. Ferraris and M. Lazzari, "Induction motor iron losses measurement with a static converter supply using a slotless rotor test bench", *IEEE Transactions on Magnetics*, vol. 30, no. 6, November 1994, pp. 4599-4601

[76] E. Nicol Hildebrand and H. Roehrdanz, "Losses in three-phase induction machines fed by PWM converter", *IEEE Transactions on Energy Conversion*, vol. 16, no. 3, September 2001, pp. 228-233

[77] T.C. Green, C.A. Hernandez-Aramburo and A.C. Smith, "Losses in grid and inverter supplied induction machine drives", *IEE Proceedings Electric Power Applications*, vol. 150, no. 6, November 2003, pp. 712-724

[78] Z. Gmyrek, A. Boglietti and A. Cavagnino, "The new methodology of the power loss calculation under deformed flux conditions", *17th International*

Conference on Electrical Machines, ICEM 2006, September 2-5 2006, Paper PTM 2-5

[79] A.M. Knight and Y. Zhan, “Identification of flux density harmonics and resulting iron losses in induction machine with nonsinusoidal supplies”, *IEEE Transactions on Magnetics*, vol. 44, no. 6, June 2008, pp. 1562-1565

[80] F.W. Carter, “The magnetic field of the dynamo-electric machine”, *Journal of the IEE*, vol. 64, 1926, pp. 1115-1138

[81] P.L. Cochran, *Polyphase induction motors: analysis, design, and application*, Marcel Dekker, New York, 1989

[82] S. Williamson and T.J. Flack, “Effect of radial rotor ventilation ducts on cage motor equivalent circuit parameters”, *IEE Proceedings Electric Power Applications*, vol. 141, no. 3, May 1994, pp. 155-162

[83] M. Liwschitz-Garik and C.C. Whipple, *Alternating-current machines*, D. Van Nostrand, New York, 1961

[84] M.G. Say, *Alternating current machines*, Pitman, London, 1976

[85] C.I. McClay, *Efficiency improvement of cage induction motors*, Ph.D Dissertation, University of Cambridge, February 1996

[86] L. Dreyfus, “Feldverteilung und wirbelstrombildung in dynamoankern”, *Arch. für E.*, vol. 4, 1915, pp. 99

[87] Ming Jiang, J. Salmon and A.M. Knight, “Design of a permanent magnet synchronous machine for a flywheel energy storage system within a hybrid electric vehicle”, *IEEE International Electric Machines and Drives Conference, IEMDC’09*, May 3-6, 2009, pp. 1736-1742

[88] J.-S. Chun, H.-K. Jung and J.-S. Yoon, “Shape optimization of closed slot rype permanent magnet motors for cogging torque using evolution strategy”, *IEEE Transactions on Magnetics*, vol. 33, no. 2, March 1997, pp. 1912-1915

[89] M. Kim, C. Lee and H. Jung, “Multiobjective optimal design of three-phase induction motor using improved evolution strategy,” *IEEE Transactions on Magnetics*, vol. 34, no. 5, September 1998, pp. 2980-2983

[90] D. Bochnia, W. Hofmann and H. Hupe, “Design optimization of permanent magnet motors by evolution strategies and finite element analysis”, *9th International Conference on Electrical Machines and Drives*, September 1-3 1999, Conference Publication No. 468, pp. 297-301

[91] T. Bäck, *Evolutionary algorithms in theory and practice*: *evolution strategies*, *evolutionary programming*, *genetic algorithms*, Oxford University Press, New York, 1996